

POLITECNICO DI TORINO

Collegio di Ingegneria Chimica e dei Materiali

**Corso di Laurea Magistrale
in Ingegneria Chimica e dei Processi Sostenibili**

Tesi di Laurea Magistrale

Computational Fluid Dynamics analysis of a supercritical CO₂ dyeing process of textiles



Relatori

Prof. Marco Vanni
Prof.ssa Ada Ferri
Prof. Antonio Buffo
Prof. Vincent Nierstrasz

Candidata

Ludovica Beatrice Chiango

Marzo 2021

Abstract

The present work deals with the CFD modelling of an industrial dyeing process assisted by supercritical carbon dioxide. Supercritical carbon dioxide (scCO₂) is a sustainable alternative used in various processes to greatly reduce (or even eliminate) the need of conventional organic solvents. More and more frequently in modern technologies it has been made use of supercritical fluids (SCFs) and the main reason can be found in their low environmental impact. Also textile industry has been influenced by the use of supercritical fluids, being one of the largest water consumers. The wide use of scCO₂ is mainly attributed to the fact that it has all the characteristics of a good solvent: it is non-toxic, non-flammable, economical and easy to remove. In the scCO₂ dyeing process the conventional solvent (water) is replaced by scCO₂ with numerous advantages (e.g., rapid coloration, possibility of reuse of the dye and solvent, low process costs). The only fully operational scCO₂ dyeing process on an industrial scale is that one of DyeCoo, a Dutch engineering company. In the present work the scCO₂ dyeing system developed by DyeCoo has been modelled using the software Ansys Fluent. In this system textile fabrics are wrapped on a beam and placed inside the dyeing vessel, the dyestuff is placed in a separate cartilage which is connected to the beam before the introduction into the vessel for the dyeing process. Here the dyeing vessel is modelled in order to investigate the flow distribution. The attention is focused on two different types of fabrics, woven and knitted, in order to better understand their behaviour when dyed in scCO₂ medium. Since in the present work fabrics are modelled as a porous medium on ANSYS Fluent, the value of permeability is important to figure out the distribution of supercritical CO₂ inside the fabric. Indeed, a good and homogeneous distribution of the flow inside the porous medium is necessary to reach the desirable level of dyeing of the fabric itself. To obtain the value of fabric permeability, CFD simulations have been conducted.

Riassunto

Durante il presente lavoro di tesi è stata svolta un'analisi CFD di un impianto di tintura di tessuti in CO₂ supercritica (scCO₂). La fluidodinamica computazionale (CFD) è oggi largamente utilizzata in vari contesti industriali, compreso il settore tessile, in cui è utilizzata per simulare vari processi di finitura o più semplicemente flussi attorno ai tessuti. Uno dei principali fattori da considerare quando ci si riferisce all'applicazione della CFD nel settore tessile è sicuramente il fatto che alcune delle tecnologie solitamente utilizzate nei processi di finitura o nella produzione di tessuti sono state sviluppate ben prima che la CFD potesse essere utilizzata, rendendo tali simulazioni un importante strumento in grado di apportare miglioramenti a processi già esistenti. Nel presente lavoro di tesi l'attenzione è stata posta sul processo di tintura con CO₂ supercritica. Tale processo si avvale della CO₂ supercritica come fluido vettore della tintura in sostituzione dell'acqua, tradizionalmente utilizzata nell'industria tessile in questo tipo di processo, guadagnandosi il nome di "waterless dyeing". Infatti, in questi anni, i fluidi supercritici hanno trovato sempre più impiego nei processi industriali come sostituti dei solventi organici convenzionali e sono stati ampiamente studiati come "green media" nei processi chimici senza solventi. Tra questi, l'anidride carbonica supercritica è la sostanza più utilizzata siccome possiede tutte le caratteristiche di un buon solvente: è atossica, non infiammabile, economica e facile da separare; inoltre, la sua temperatura critica e pressione critica sono relativamente basse ($T_c=31.1C$, $p_c=72$ bar). Siccome l'industria tessile è una delle principali industrie consumatrici di acqua ed è anche tra le maggiori responsabili del suo inquinamento, può sicuramente ottenere diversi vantaggi dall'utilizzo dell'anidride carbonica supercritica in sostituzione dell'acqua. Con l'utilizzo di questa tecnica è inoltre possibile accorciare i tempi di tintura grazie alla bassa viscosità tipica di un gas e alle buone caratteristiche di diffusione della CO₂ supercritica. Infatti, i fluidi supercritici presentano in generale una minore viscosità ed un maggiore coefficiente di diffusione rispetto ai liquidi, favorendo così il trasporto di materia. Inoltre, l'utilizzo della scCO₂ nel processo di tintura garantisce una maggiore sostenibilità del processo stesso e una produzione pulita, poiché si andrebbero ad eliminare sia l'acqua sia i prodotti chimici tradizionalmente utilizzati durante la fase di tintura. In aggiunta, vi è la possibilità di riutilizzare il colorante in eccesso recuperandolo dalla CO₂ scaricata in uscita. Il poliestere è uno dei materiali che meglio si presta all'utilizzo di questa tecnica. Quando si fa riferimento alla tintura del poliestere assistita da CO₂ supercritica, in genere sono compresi i seguenti step: per prima cosa i coloranti dispersi sono disciolti nella CO₂ supercritica; successivamente sono trasferiti sulla fibra di poliestere causandone l'assorbimento e la diffusione al loro interno. La CO₂ supercritica riesce a rigonfiare il materiale, esercitando un'azione plasticizzante del polimero ed incrementando il processo di diffusione delle molecole di colorante all'interno delle fibre. Con lo step di depressurizzazione la CO₂ si allontana dal tessuto, che si restringe, intrappolando il colorante al suo interno. Il livello di tintura è influenzato da ciascuno dei meccanismi sopra descritti, che sono controllati dalle proprietà fisiche dei coloranti utilizzati e dai parametri del processo (come la portata di scCO₂, la temperatura, ecc..).

Attualmente l'unico processo pienamente operativo per la tintura di tessuti assistita da CO₂ supercritica è quello dell'azienda olandese DyeCoo. Il sistema sviluppato dalla DyeCoo prevede che il tessuto da tingere sia avvolto su di un tubo forato (beam) e posto nel vessel adibito al processo. Il colorante è posizionato in un contenitore separato, che viene collegato al beam nel momento del suo inserimento nel vessel. Una volta terminato il processo di tintura, la CO₂ viene condotta nel separatore, dove avviene il recupero del colorante residuo, che può essere utilizzato nei processi successivi. Non solo il colorante viene recuperato: circa

il 95% della CO_2 può essere riciclata alla fine di ogni processo con questa tecnica. Alla fine del processo si ottiene un tessuto completamente asciutto che non richiede ulteriori operazioni di asciugatura. Con tale sistema è possibile ridurre la quantità di colorante utilizzato, i consumi elettrici ed il tempo di tintura riducendo quindi i costi totali. La quantità di PET processato da ciascuna macchina della DyeCoo è circa 800 000 kg all'anno, questo garantisce un effettivo risparmio di 32 milioni di litri di acqua e 160 000 kg di sostanze chimiche, solitamente ritrovate nelle acque di scarico industriali. La DyeCoo ha inoltre instaurato collaborazioni con marchi come Nike ed Ikea. In **Figura 1** è mostrato il reattore utilizzato dalla DyeCoo nel processo di tintura con CO_2 supercritica, modellato nel presente lavoro.

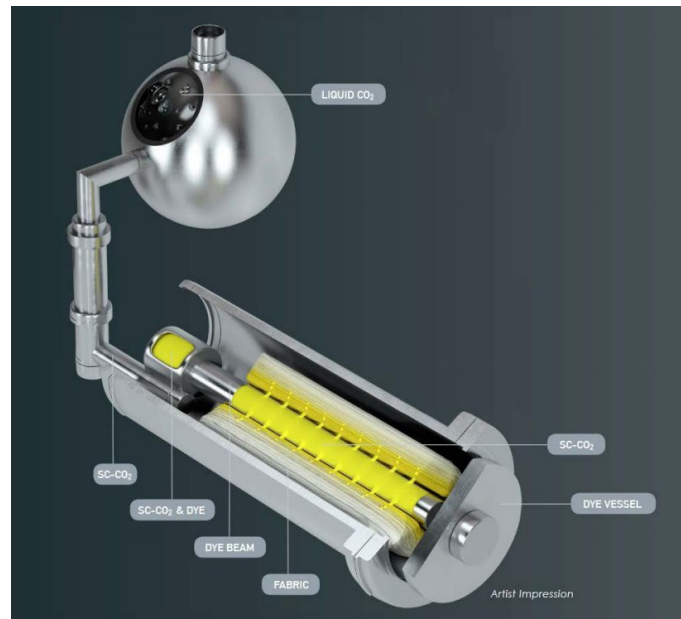


Figura 1: Reattore di tintura, DyeCoo company

Sono pochi gli studi in letteratura che indagano la modellizzazione CFD di un processo di tintura tradizionale, e ancora meno quelli riguardanti il processo di tintura assistito da anidride carbonica supercritica. Nel presente lavoro di tesi è stato modellato il reattore utilizzato dalla compagnia DyeCoo (chiamato DyeOx) con lo scopo di investigare gli aspetti fluidodinamici del processo riguardanti il flusso di scCO_2 attraverso il tessuto. In questo tipo di processo un'equa distribuzione del fluido all'interno dell'autoclave è importante al fine di ottenere una colorazione uniforme del tessuto. Infatti, è qui che la miscela di anidride carbonica supercritica e colorante permeano attraverso la massa del tessuto.

Il presente lavoro di tesi si avvale della CFD per modellare il processo di tintura utilizzato dalla DyeCoo utilizzando il software ANSYS Fluent. Lo studio è stato condotto principalmente su due scale: quella della struttura del tessuto, per determinarne la permeabilità, e quella del reattore, per studiare il campo di moto del fluido nell'impaccato. In particolare, per il primo aspetto, è stata presa in considerazione la diversa struttura dei tessuti in termini di permeabilità per capire come essa influenzi il processo e quanto influisca sulla distribuzione del flusso all'interno del tessuto. Il DyeOx è infatti utilizzato per la tintura di due tipologie di tessuto: intrecciato (woven) e lavorato a maglia (knitted). Nel presente lavoro sono stati revisionati vari test di permeabilità all'aria condotti su tessuti intrecciati e a maglia, concludendo che questi ultimi presentano un più alto valore di permeabilità all'aria. Questo è

dovuto alla particolare struttura ad anello che contraddistingue i tessuti lavorati a maglia, che comporta la presenza di un maggior numero di pori rispetto ai tessuti intrecciati dello stesso peso. Va sottolineato che la permeabilità all'aria dei tessuti è strettamente correlata al peso del tessuto stesso e alla sua struttura, influenzata da spessore e porosità. Per ottenere i valori di permeabilità di un tessuto intrecciato (woven fabric) è stata utilizzata la CFD per riprodurre le prove di permeabilità all'aria usualmente condotte sui tessuti.

La permeabilità è una proprietà specifica in un dato mezzo poroso ed in generale, per un materiale anisotropo è un tensore. Nel caso di tessuti intrecciati (woven fabrics) questo tensore diventa ortotropico e quindi vi è un sistema di coordinate principali a cui corrisponde il seguente tensore:

$$[K] = \begin{bmatrix} K_1 & 0 & 0 \\ 0 & K_2 & 0 \\ 0 & 0 & K_3 \end{bmatrix},$$

in cui K_1 e K_2 sono le permeabilità nel piano (in-plane permeability) e K_3 è la permeabilità lungo lo spessore del tessuto (through-thickness permeability). In generale questi tre valori sono diversi tra loro per un dato tessuto e quindi il flusso è sottoposto a diverse resistenze all'interno del mezzo poroso. In aggiunta, il tessuto è composto da fili, che sono a loro volta composti da fibre; di conseguenza, anche per i fili è possibile distinguere due valori di permeabilità: la permeabilità lungo le fibre (K_{\parallel}) e la permeabilità perpendicolare alle fibre (K_{\perp}). I valori della permeabilità dei tessuti sono importanti un ampio range di applicazioni che riguardano il flusso attraverso i tessuti, ed è per questo che l'interesse nel calcolare la permeabilità dei tessuti attraverso la CFD sta recentemente crescendo.

Nella prima parte del presente lavoro, sono state eseguite simulazioni del passaggio di un flusso d'aria attraverso il tessuto plain-woven al fine di calcolarne la rispettiva permeabilità nel piano e attraverso lo spessore, confrontando i dati di permeabilità all'aria di tessuti effettuati sulla base del test descritto dalla UNI EN ISO 9237:1997. La struttura del tessuto scelto (PL22/15, "plain weave with 22 ends/cm for warp yarns and 15 ends/cm for weft yarns"), di cui si conosce il valore di permeabilità all'aria da dati presenti in letteratura, è stata ricreata mediante il software TexGen. I dettagli relativi al tipo di tessuto scelto sono disponibili in **Tabella 1**.

Tabella 1: caratteristiche del tipo di tessuto scelto per le simulazioni

Sample	PL22/15
Thickness (mm)	0.4390
R (exp.) $\text{cm}^3/\text{cm}^2 \text{ s}$	239.2
fabric porosity (%)	78.45
Mass (g/m^2)	143.9

La geometria è stata in seguito importata nel software ANSYS Fluent, in cui è stato costruito un canale a sezione rettangolare di lunghezza pari a 10 mm. Il modello è stato validato riproducendo le stesse condizioni del test di permeabilità all'aria condotto su quel tipo di tessuto (test descritto dalla UNI EN ISO 9237:1997), mostrando una deviazione di circa l'8%

rispetto alla prova sperimentale, valore considerato accettabile. La geometria utilizzata per questo tipo di simulazioni è mostrata in **Figura 2**. In tale figura sono riportate anche le condizioni a contorno imposte su ANSYS Fluent. Per la mesh (rappresentata in **Figura 3**) sono stati utilizzati elementi tetraedrici sia per il canale che per il tessuto, per un totale di 591095 nodi e 2677686 elementi. Le simulazioni stazionarie sono state eseguite specificando il modello laminare per i test condotti a basse velocità, mentre il modello di turbolenza $k-\epsilon$ è stato utilizzato per velocità dell'aria in ingresso più elevate. Come metodo risolutivo sul software ANSYSYS Fluent è stato imposto il SIMPLE Pressure-Velocity Coupling e discretizzazione spaziale del secondo ordine. I fili componenti il tessuto sono stati trattati come mezzo poroso, in cui è stata specificata la permeabilità, calcolata mediante formule riportate in letteratura e pari a $1.35 \times 10^{-11} \text{ m}^2$. Al fine di considerare un tessuto infinitamente esteso sono state impostate condizioni di simmetria per le pareti del canale, come mostrato in **Figura 2**.

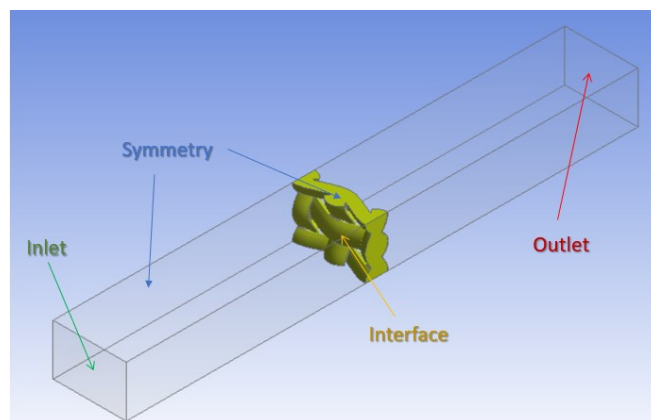


Figura 2: Dominio computazionale e condizioni a contorno, simulazioni per la permeabilità lungo lo spessore del tessuto

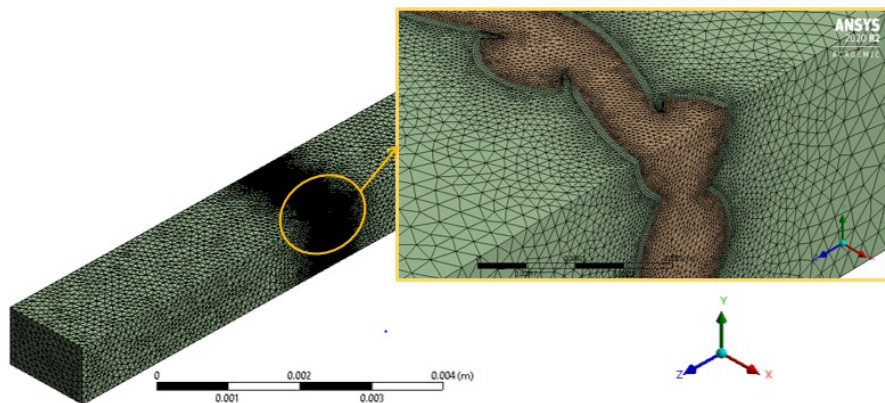


Figura 3: Dettaglio della mesh, simulazioni per la permeabilità lungo lo spessore del tessuto

Imponendo il valore della velocità dell'aria in ingresso al canale, è stato ricavato il ΔP lungo lo spessore del tessuto. Sono stati imposti bassi valori di velocità dell'aria in ingresso al canale al fine di poter ricadere nel range di validità della legge di Darcy e quindi ricavare il valore della permeabilità lungo lo spessore, K_T , per il dato tessuto attraverso la seguente formula (Darcy):

$$\Delta P = \frac{\mu L Q}{K_T A}, \quad (1)$$

in cui ΔP è la differenza di pressione lungo lo spessore (L), A è l'area attraverso la quale passa il flusso d'aria e Q è la portata di aria. In **Tabella 2** sono mostrati i risultati di tali simulazioni.

Tabella 2: Set di prove a bassa velocità, permeabilità lungo lo spessore

Inlet velocity (m/s)	ΔP (Pa)	K_T (m ²)
0.01	0.210	4.21×10^{-10}
0.05	1.08	4.15×10^{-10}
0.025	0.536	4.19×10^{-10}

Un ulteriore test è stato condotto imponendo la CO₂ come fluido alla pressione e temperatura utilizza nel processo di tintura della DyeCoo ed imponendo una bassa velocità della CO₂ in ingresso. Anche in questo caso i risultati sono coerenti con quelli prima mostrati (**Tabella 3**). Questa è stata ritenuta un'ulteriore conferma del modello.

Tabella 3: Set di prove a bassa velocità, permeabilità lungo lo spessore - scCO₂

Fluid	Inlet velocity (m/s)	ΔP (Pa)	K_T (m ²)
scCO ₂	0.0265	0.57	4.19×10^{-10}

Solo per bassi valori di velocità il flusso in un mezzo poroso è descritto da una relazione lineare tra ΔP e la velocità del flusso. Aumentando il ΔP aumenta anche il numero di Reynolds, pur rimanendo in regime laminare, in tali condizioni la relazione tra il ΔP e la velocità del flusso non è più lineare. Ciò significa che la legge di Darcy non può essere usata per un'analisi accurata del flusso e quindi bisogna considerare anche il contributo del termine inerziale. L'equazione usata per descrivere il comportamento del mezzo poroso su ANSYS Fluent in questo caso è riportata di seguito:

$$\Delta P = \frac{\mu L}{K_T} v + \frac{LC_2 \rho}{2} v^2. \quad (2)$$

Di conseguenza è stato condotto un secondo set di simulazioni al fine di poter ottenere il valore di C_2 per il tessuto in esame dall'Equazione (2). In **Tabella 4** sono mostrati i risultati di questo ultimo set di simulazioni, in cui C_2 è stato ricavato sostituendo nell'Equazione (2) il ΔP calcolato, la portata di fluido passante attraverso il tessuto e il valore medio di K_T ricavato dal primo set di simulazioni. In tal modo è stata ottenuta l'equazione della curva che mette in relazione ΔP e velocità per il tessuto in esame: $\Delta P = 35.19v^2 + 21.51v$.

Tabella 4: Set di prove a velocità più elevata, permeabilità lungo lo spessore

Inlet velocity (m/s)	ΔP (Pa)	K_T (m ²)	C_{2T} (1/m)
1	5.90×10^1	4.18×10^{-10}	1.22×10^5
2	1.84×10^2	4.18×10^{-10}	1.15×10^5
3	3.59×10^2	4.18×10^{-10}	1.07×10^5

I risultati di queste simulazioni sono riassunti in **Tabella 5**.

Tabella 5: Risultati delle simulazioni, permeabilità lungo lo spessore

K_T (m ²)	4.18×10^{-10}
$1/K_T$ (1/m ²)	2.39×10^9
C_2 (1/m)	1.15×10^5

Lo stesso metodo è stato utilizzato per ricavare la permeabilità del tessuto nel piano. La geometria utilizzata per queste simulazioni è mostrata in **Figura 4**; è stato utilizzato lo stesso approccio descritto precedentemente con la sola eccezione che il tessuto è stato inclinato di 45° all'interno del canale. In tal modo è stato possibile ricavare il contributo della permeabilità nel piano, conoscendo il valore della componente della permeabilità lungo lo spessore. La mesh è stata generata imponendo le stesse dimensioni e caratteristiche della mesh precedentemente descritta per le simulazioni della permeabilità lungo lo spessore, per un totale di 670118 nodi and 3044646 elementi. Anche per queste simulazioni stazionarie è stato utilizzato il modello laminare per basse velocità dell'aria in ingresso al canale ed il modello di turbolenza Realizable $k-\varepsilon$ per velocità più elevate. Sono stati utilizzati il pressure based solver, SIMPLE Pressure-Velocity Coupling e la discretizzazione spaziale del secondo ordine come metodi risolutivi. Anche in questo sistema i fili componenti il tessuto sono stati modellati come mezzo poroso, in cui è stata specificata una permeabilità pari a 1.35×10^{-11} m². Per queste simulazioni le pareti del canale non sono state più impostate come zone di simmetria ma come pareti in cui è stato specificato uno sforzo a parete nullo. Nonostante la permeabilità nel piano di un tessuto abbia due componenti diverse tra loro, qui sono state considerate per semplicità uguali e pari a K_P , ricavato dalle simulazioni tramite le seguenti relazioni:

$$\Delta P = \frac{\mu L Q}{K' A}, \quad (3)$$

$$K' = K_T + K_P. \quad (4)$$

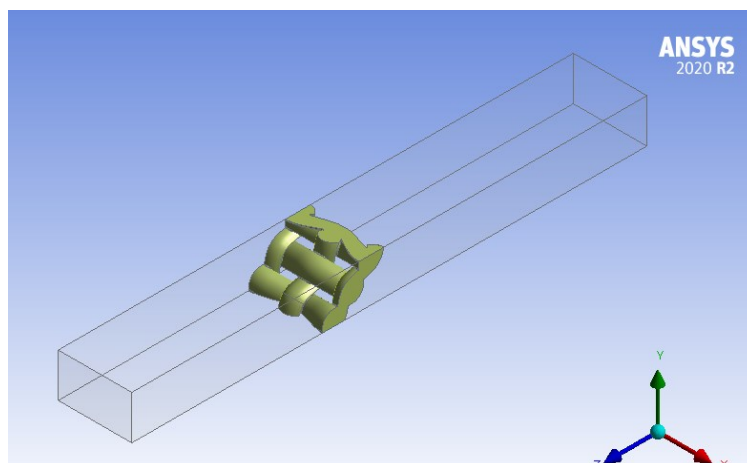


Figura 4: Dominio computazionale, simulazioni per la permeabilità nel piano

Dal primo set di simulazioni, condotte impostando basse velocità dell'aria in ingresso al canale, sono stati ricavati i valori di K_P utilizzando le equazioni (3) e (4), i risultati sono mostrati in **Tabella 6**. Il valore finale di K_P è stato ottenuto facendo una media dei risultati delle simulazioni.

Tabella 6: Set di prove a bassa velocità, permeabilità nel piano

Inlet velocity (m/s)	ΔP (Pa)	K'	K_P (m ²)
0.01	0.19	1.31×10^{-9}	8.90×10^{-10}
0.05	0.938	1.30×10^{-9}	8.77×10^{-10}
0.025	0.47	1.31×10^{-9}	8.87×10^{-10}

Anche in questo caso è stato poi impostato un secondo set di simulazioni al fine di calcolare C_2' dalla seguente relazione, utilizzando i dati ricavati dalla simulazione e il valore medio di K_P , precedentemente ricavato:

$$\Delta P = \frac{\mu L}{K'} v + \frac{LC_2' \rho}{2} v^2. \quad (5)$$

I risultati di questo secondo set sono riportati in **Tabella 7**.

Tabella 7: Set di prove a velocità più elevata, permeabilità nel piano

Inlet velocity (m/s)	ΔP (Pa)	K' (m ²)	C_2' (1/m)
1	43.601	1.3×10^{-9}	30175.876
2	137.933	1.3×10^{-9}	30425.815
3	275.561	1.3×10^{-9}	29510.213

Mentre in **Tabella 8** sono riassunti i risultati ottenuti da entrambi i set di simulazioni.

Tabella 8: risultati delle simulazioni, permeabilità nel piano

K_P (m^2)	8.85×10^{-10}
$1/K_P$ ($1/m^2$)	1.13×10^9
C_2' ($1/m$)	3.00×10^4

Nella seconda parte del lavoro di tesi è stato condotto lo studio della distribuzione della velocità all'interno del reattore DyeCoo al variare di alcuni parametri del processo. Per questo tipo di simulazioni è stata generata una geometria bidimensionale assial-simmetrica al fine di ridurre il costo computazionale. È stato quindi condotto uno studio di sensibilità al variare della geometria modellata sul software, della portata di CO_2 supercritica in ingresso al reattore e del valore di permeabilità del tessuto.

Di seguito viene riportata la geometria bidimensionale del reattore (**Figura 5**).



Figura 5: Geometria del reattore per il processo di tintura dei tessuti assistito da $scCO_2$

L'altezza radiale della bobina di tessuto è stata considerata pari a 0.2 m, valore calcolato tenendo conto delle condizioni di carico tipiche dell'autoclave. Sono state considerate due diverse geometrie: una in cui la superficie laterale del beam a contatto con il tessuto è stata considerata un'interfaccia per il sistema, e un'altra in cui si è tenuto conto della struttura perforata del tubo. Per la seconda, il beam è stato disegnato praticando dei fori di 5 mm intervallati da una distanza di 5 mm su tutta la lunghezza del tubo. In seguito, ci si riferirà al primo caso come "beam semplificato" ed al secondo come "beam perforato". I dettagli della mesh utilizzata per entrambi i casi sono mostrati in **Tabella 9** e **Tabella 10**.

Tabella 9: Mesh details, simplified beam configuration

Element size (m)	5.00×10^{-3}
Nodes	35828
Elements	34611

Tabella 10: Mesh details, perforated beam configuration

Element size (m)	5.00×10^{-3}
Nodes	70354
Elements	68150

Va aggiunto che per il caso perforato è stato eseguito un affinamento in corrispondenza dei fori del beam, impostando un numero pari a 5 divisioni per ogni foro e 5 divisioni per ogni intervallo tra i fori (ovvero le pareti per del beam perforato), come mostrato in **Figura 6**. Inoltre, in entrambi le configurazioni sono state impostati 4 layer di inflation alle pareti del vessel, beam e della bobina.

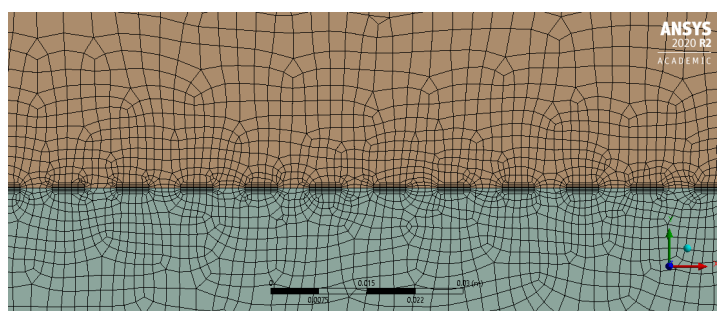


Figura 6: Dettaglio della mesh utilizzata per la configurazione con il beam perforato, interfaccia con il mezzo poroso

Le condizioni operative del Sistema sono $120\text{ }^{\circ}\text{C}$ e 250 bar . Una tipica condizione di funzionamento dell'impianto prevede una portata di CO_2 supercritica in ingresso al sistema pari a $500\text{ m}^3/\text{h}$ oppure $1000\text{ m}^3/\text{h}$. In questo lavoro di tesi si è scelto di considerare una portata di $500\text{ m}^3/\text{h}$ come caso base, successivamente è stato fatto anche un confronto considerando una portata di scCO_2 in ingresso pari a $1000\text{ m}^3/\text{h}$.

Per un primo set di simulazione la bobina è stata modellata come mezzo poroso in cui è stata specificata una resistenza viscosa ($1/K$) pari a $6.086 \times 10^{+10}\text{ 1/m}^2$ e una resistenza inerziale pari a zero, sulla base di simili esempi in letteratura.

Come condizioni a contorno sono state impostate la portata di scCO_2 in ingresso al sistema e la pressione di uscita, pari alla pressione di esercizio. Le pareti del vessel sono state impostate come "stationary walls" a cui è stata imposta la condizione di no slip e una temperatura fissa di 393.15 K .

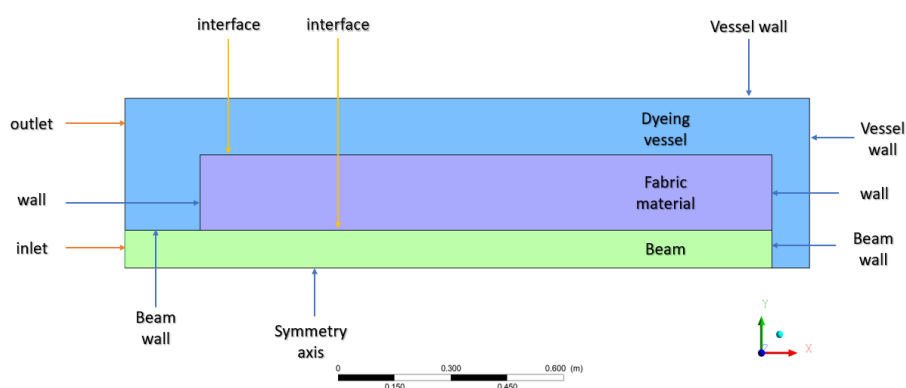


Figura 7: Dominio computazionale e condizioni a contorno, reattore di tintura

Per queste simulazioni, condotte in regime stazionario, è stato scelto il Realizable $k-\varepsilon$ model come modello di turbolenza sulla base di studi condotti in letteratura riguardo la modellazione di fluidi supercritici. È stato impostato il density-based solver in ANSYS Fluent per risolvere le equazioni di governo del sistema, con una formulazione implicita e discretizzazione spaziale del secondo ordine. Le proprietà del fluido sono state descritte secondo il modello del National Institute of Standards and Technology (NIST), in cui è implementata l'equazione di stato per l'anidride carbonica di Span e Wagner.

Inizialmente è stato svolto lo studio di sensibilità alla mesh al fine di ottenere dei risultati indipendenti dalla griglia scelta. Per questa analisi sono stati monitorati, come parametri chiave per il sistema, il valore del ΔP a cavallo del poroso e il valore della velocità della $scCO_2$ misurata all'interno della bobina lungo la direzione assiale, tenendo fissa l'altezza radiale, come mostrato in **Figura 8**.

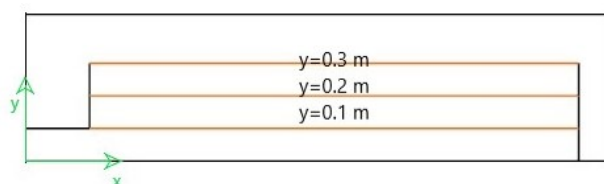


Figura 8: Rappresentazione delle varie altezze radiali a cui è stata calcolata la velocità media del fluido all'interno del mezzo poroso

Una volta individuate le mesh definitive per entrambe le configurazioni (beam perforato e beam semplificato) si è proceduto con un confronto tra le due. Confronto eseguito prendendo in esame anche la temperatura e la pressione dell'intero sistema, oltre al ΔP a cavallo del poroso e al valore della velocità della $scCO_2$ all'interno della bobina. Comparando graficamente il campo di pressione e temperatura per entrambe le simulazioni, si è concluso che sono abbastanza simili tra loro in termini di risultati ottenuti. Si è valutato inoltre il valore della velocità radiale a 1, 2 e 3 cm di distanza dalla zona di contatto tra tessuto e tubo forato, in cui la velocità è più elevata e il fluido inizia a permeare attraverso il tessuto nei vari strati avvolti l'uno sull'altro. Nella configurazione con il "beam perforato" il fluido è accelerato in corrispondenza dei fori, facendo pensare quindi ad una distribuzione non omogenea

all'interno della bobina. In realtà, focalizzandosi sul valore della velocità all'interno dei primi strati del poroso, i risultati mostrano che la velocità radiale si uniforma quasi subito all'interno del mezzo poroso, come si può vedere dalla **Figura 8**. L'andamento mostrato graficamente è confermato anche dai risultati numerici in **Tabella 11**, che riporta il valore della velocità misurata fissando la coordinata y a 0.11, 0.12 and 0.13 m (quindi nei primi 1, 2 e 3 centimetri del poroso rispettivamente) nelle due configurazioni studiate. Da qui si può osservare che già dopo i primi 2 cm il valore della velocità della scCO₂ differisce solo dell'1% tra le due configurazioni. Questo andamento si mantiene costante per tutto lo spessore della bobina.

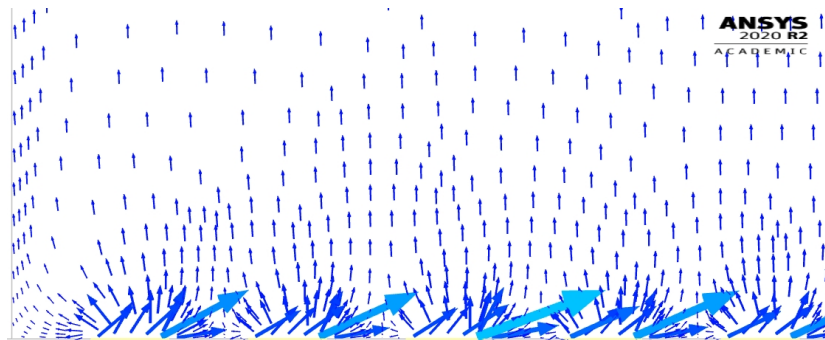


Figura 8: Vettori velocità all'interfaccia tra beam perforato e mezzo poroso

Tabella 11: Velocità media all'interno del tessuto in direzione assiale misurata ad altezza costante: discostamenti tra le due configurazioni analizzate

	Simplified	Perforated	Deviation
average velocity magnitude (m/s) at y=0.11 m	1.15×10^{-1}	1.30×10^{-1}	-13%
average velocity magnitude (m/s) at y=0.12 m	1.21×10^{-1}	1.19×10^{-1}	1%
average velocity magnitude (m/s) at y=0.13 m	1.13×10^{-1}	1.10×10^{-1}	3%

Anche il valore del ΔP è molto simile per le due configurazioni e mostra una deviazione del solo 3%. In conclusione, si è quindi pensato di procedere scegliendo la configurazione con il "beam semplificato" per le successive simulazioni in modo da ridurre il costo computazionale e la complessità del sistema, dal momento che le differenze tra i due risultati sono state considerate trascurabili.

Un'ulteriore analisi è stata condotta variando la portata di scCO₂ in ingresso al sistema, in particolare aumentandola. Le condizioni operative utilizzate per le due simulazioni a confronto sono indicate in **Tabella 12**.

Tabella 12: Condizioni operative nei Casi A e B, analisi di sensitività relativa alla portata di scCO₂ in ingresso

	Caso A	Caso B
Temperatura	120 °C	120 °C
Pressione	250 bar	250 bar
Portata	500 m ³ /h	1000 m ³ /h

Il confronto tra il Caso A e B è stato fatto in termini di temperatura, pressione e velocità radiale della scCO₂ all'interno del poroso. In particolare, il campo di temperatura risulta essere molto simile in entrambi i casi mantenendo un valor medio di 120 °C in tutto il dominio. Nel caso B si è registrato un aumento di pressione rispetto al caso A, in particolar modo lungo il tubo e all'interfaccia con il mezzo poroso; il ΔP a cavallo del poroso è quindi più alto del caso A e pari a 7.53×10^4 Pa. Il risultato più interessante è stato ottenuto dal confronto tra le velocità della scCO₂ in direzione radiale. A questo proposito sono qui riportati i grafici delle velocità radiali misurate a tre diverse altezze all'interno del poroso (**Figura 9** e **Figura 10** per i Casi A e B). Nel caso A è evidente che la velocità rimane abbastanza costante in tutta la lunghezza del tessuto, mentre nel caso B è possibile osservare come aumentando la portata la velocità della scCO₂ tende ad aumentare lungo l'asse x ad altezza radiale costante. Questa non omogenea distribuzione della velocità radiale della scCO₂ potrebbe risultare in una colorazione non uniforme del tessuto; l'andamento è costante in tutto lo spessore della bobina ed è anche coerente con i risultati riportati in letteratura, in cui si è osservato che un aumento di portata massica comporta una distribuzione della velocità altamente disomogenea.

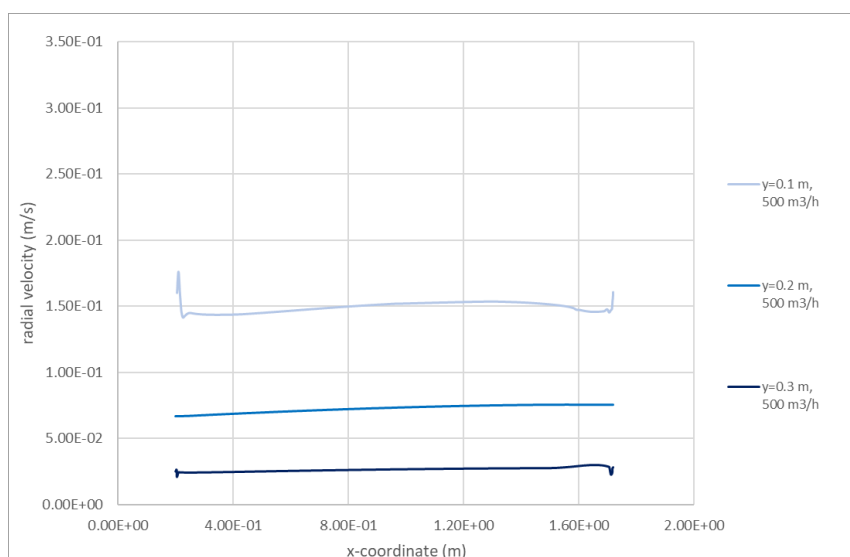


Figura 9: Velocità radiale media all'interno del tessuto in direzione assiale misurata ad altezza costante – portata in ingresso: 500 m³/h

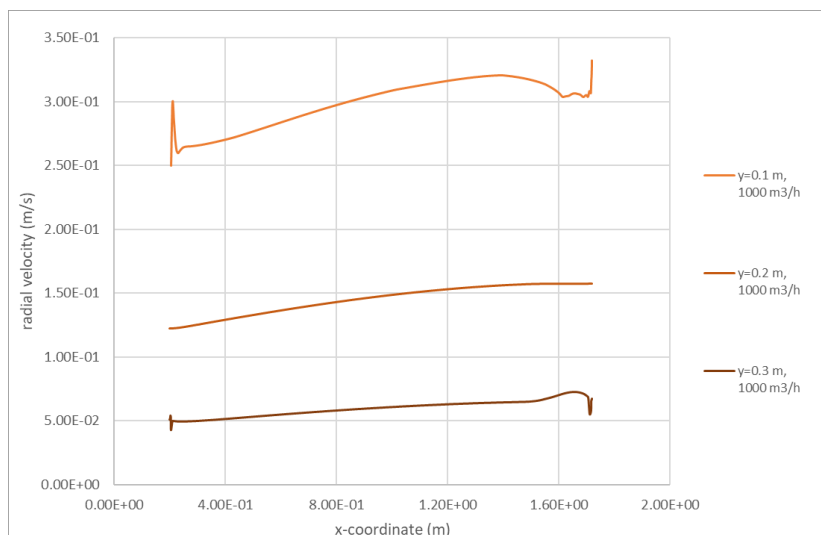


Figura 10: Velocità radiale media all'interno del tessuto in direzione assiale misurata ad altezza costante – portata in ingresso: 1000 m³/h

Per capire l'influenza della struttura del tessuto sulla distribuzione della scCO₂ all'interno del vessel ed in particolar modo all'interno del mezzo poroso, è stata eseguita un'ulteriore analisi. Nelle simulazioni fin ora presentate il tessuto è stato modellato come mezzo poroso con permeabilità isotropica pari a $1.643 \times 10^{-11} \text{ m}^2$, come specificato in letteratura e riportato in **Tabella 13**. Nelle successive simulazioni sono stati variati i parametri di permeabilità del mezzo poroso. In particolare, sono stati utilizzati i valori ricavati dall'analisi CFD di permeabilità condotta nella prima parte del lavoro per un tessuto intrecciato (plain weave 22/15).

Tabella 13: Dettagli del mezzo poroso, Caso A

Case A	
Permeabilità, $K \text{ (m}^2\text{)}$	1.643×10^{-11}
Resistenzaz viscosa, $1/K \text{ (1/m}^2\text{)}$	6.086×10^{10}
Resistenzaz inerziale, $C_2 \text{ (1/m)}$	0

Un primo test è stato impostato modellando il tessuto come mezzo poroso con permeabilità isotropa e pari al valore della permeabilità lungo lo spessore per il tessuto PL 22/15, ricavata nella prima parte del lavoro. Di seguito verrà fatto riferimento a questo caso come Caso C, le cui caratteristiche sono riportate in **Tabella 14**.

Tabella 14: Dettagli del mezzo poroso, Caso C

Case C	
Permeabilità, $K \text{ (m}^2\text{)}$	4.184×10^{-10}

Resistenzaz viscosa, $1/K$ ($1/m^2$)	2.39×10^9
Resistenzaz inerziale, C_2 ($1/m$)	0

La permeabilità impostata nel caso C è maggiore di quella del Caso A, infatti anche il campo di pressione è abbastanza diverso nei due casi: adesso non è più omogeneo all'interno del poroso ma la pressione raggiunge il valore più elevato in corrispondenza dell'ultima zona del tessuto, in cui la scCO₂ è forzata a permeare all'interno del tessuto a causa della presenza della parete finale del beam. Questo andamento si riflette anche sulla distribuzione delle velocità radiali all'interno del poroso. Infatti, dalla **Figura 11** si vede come la scCO₂ abbia un andamento completamente diverso nei casi A e C. In particolare, sembra che nel Caso C il fluido non attraversi il tessuto in maniera omogenea, penalizzando la parte iniziale e raggiungendo valori elevati solo in corrispondenza della parte finale del mezzo poroso. Questo potrebbe risultare in una distribuzione non omogenea di colorante all'interno dei vari strati del tessuto.

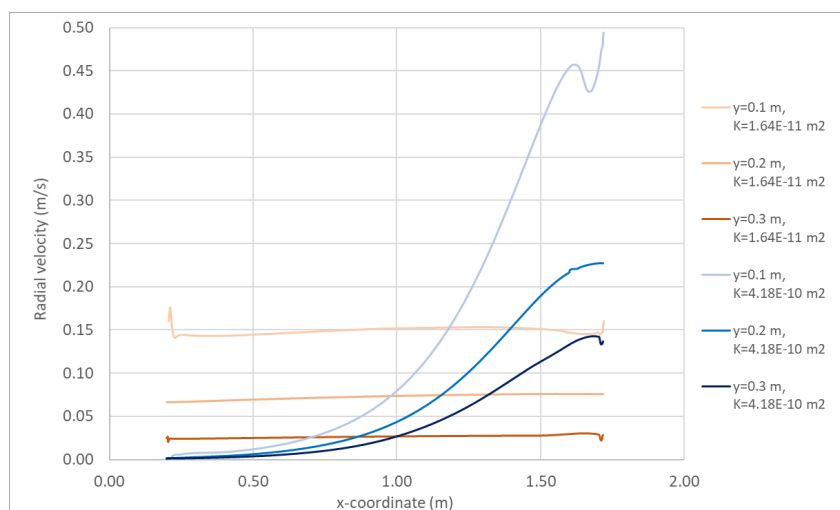


Figura 11: velocità radiale media all'interno del tessuto in direzione assiale misurata ad altezza costante – confronto tra i Casi A e C

Siccome il valore di permeabilità considerato in questo caso risulta essere più elevato del caso A, si può concludere che aumentando la permeabilità del tessuto si incorre nel rischio di ottenere velocità non omogenee all'interno della bobina di tessuto. Questo andamento è stato confermato e mostrato graficamente in **Figura 12**, in cui è riportato l'andamento della velocità radiale della scCO₂ all'interno del mezzo poroso nel primo strato del tessuto ottenuta simulando bobine con diversa permeabilità (per ipotesi isotropa). In particolare, sono riportati i risultati ottenuti da altre due simulazioni in cui è stato impostato un valore intermedio di permeabilità tra il caso A e C ($8.00 \times 10^{-11} m^2$) ed uno più basso ($8.00 \times 10^{-12} m^2$). Il trend è coerente: l'aumento della permeabilità del tessuto incide sulla distribuzione della velocità radiale della scCO₂, rendendola non omogenea all'interno del tessuto con un andamento crescente lungo l'asse x. Questo risultato è interessante in quanto permette di fare anche una prima considerazione rispetto al comportamento che possono avere i diversi tessuti impiegati in tale processo: sembrerebbe infatti che la disomogeneità nel flusso aumenti con l'aumentare

della permeabilità, ci si aspetta dunque che tessuti più permeabili, come quelli a maglia (knitted fabrics), siano maggiormente interessati da questo fenomeno.

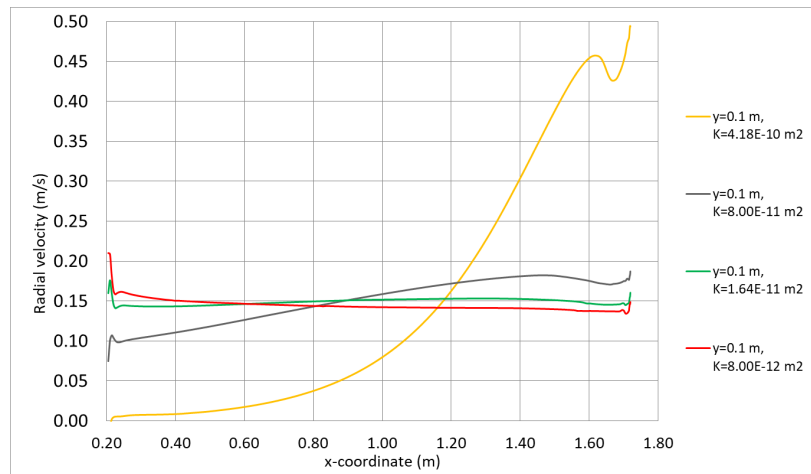


Figura 12: Velocità radiale media della scCO₂ nel primo strato di tessuto a contatto con il beam, influenza del valore di permeabilità K del tessuto.

Un altro aspetto da considerare è che i valori di permeabilità impostati nel caso C si riferiscono alla permeabilità di un solo strato di tessuto. Per questo motivo va sottolineato che la permeabilità dei tessuti è strettamente correlata agli spazi vuoti che si creano tra i vari fili che lo compongono, che rappresentano il percorso preferenziale del fluido. Una volta che il tessuto viene avvolto attorno alla trave perforata, vi sarà una sovrapposizione di diversi strati di tessuto, che andranno a modificare le vie preferenziali del fluido attraverso il mezzo poroso. Di conseguenza ci si potrebbe aspettare un valore più basso di permeabilità rispetto a quello utilizzato nel caso C, che risulta quindi non adeguato a descrivere il comportamento del sistema.

In un secondo caso, Caso D, è stata considerata sia la permeabilità (isotropica) del tessuto che la resistenza inerziale ricavata dalle simulazioni condotte nella prima parte del lavoro. I valori impostati per descrivere il mezzo poroso in ANSYS Fluent sono riportati in **Tabella 15**.

Tabella 15: Dettagli del mezzo poroso, Caso D

Caso D	
Permeabilità, K (m^2)	4.184×10^{-10}
Resistenza viscosa, $1/K_T$ ($1/m^2$) (isotropic)	2.39×10^9
Resistenza inerziale, C_2 ($1/m$) (isotropic)	1.15×10^5

I risultati ottenuti questa volta sono molto diversi dal caso C, nonostante il valore della permeabilità fosse uguale per entrambe le simulazioni. Questo dimostra che il contributo del

termine inerziale influisce molto sulla distribuzione del flusso quando si considerano elevati valori di permeabilità del mezzo poroso, che causano elevate velocità in determinate zone del mezzo poroso. Questo risultato è graficamente osservabile in **Figura 13**, dove viene fatto un confronto tra i risultati della velocità radiale della $scCO_2$ all'interfaccia con il poroso per il caso C e D. Inoltre, la pressione all'interno del poroso risulta più omogenea e di conseguenza anche la distribuzione dei vettori velocità sia in modulo che in verso lungo i vari strati del mezzo poroso.

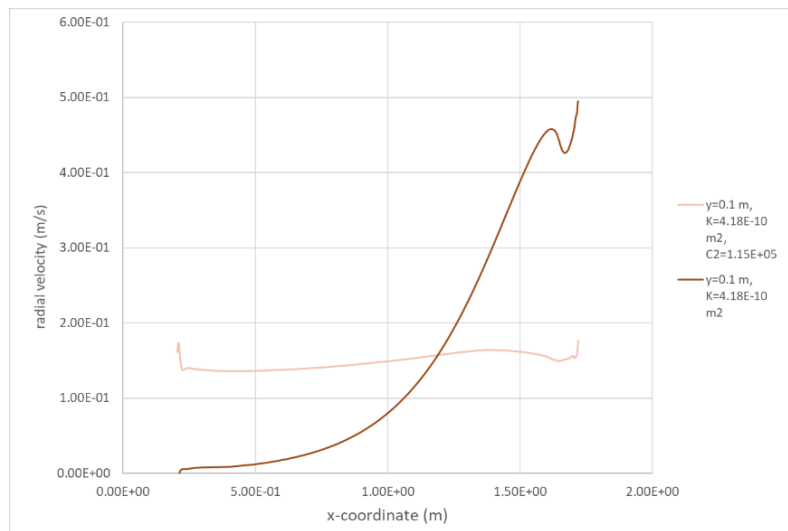


Figura 13: Average radial velocity inside the porous medium along the axial direction at the inlet of the porous medium – Cases C and D

Nell'ultima simulazione sono stati impostati in ANSYS Fluent entrambi i valori di permeabilità nel piano e lungo lo spessore (K_T , K_P) e le relative resistenze inerziali al flusso (C_2 , C_2') ricavate nella prima parte del lavoro. Si farà riferimento a questa prova come Caso E; in **Tabella 16** sono riportati i valori specificati come input del mezzo poroso nel software.

Tabella 16: Dettagli del mezzo poroso, Caso E

Caso E	
Resistenza viscosa, $1/K_T$ ($1/m^2$) (direzione radiale)	2.39×10^9
Resistenza inerziale, C_2 ($1/m$) (direzione radiale)	1.15×10^5
Resistenza viscosa, $1/K_P$ ($1/m^2$) (direzione assiale)	1.13×10^9
Resistenza inerziale, C_2' ($1/m$) (direzione assiale)	3.00×10^4

I risultati di questa simulazione sono molto simili a quelli del caso D, in cui è stata considerata una permeabilità isotropa del tessuto, pari a K_T . Questo si può giustificare con il fatto che la componente assiale di velocità risulta molto più bassa rispetto alla componente radiale, di conseguenza il valore della permeabilità specificato in direzione assiale influenza poco il comportamento fluidodinamico del sistema. Questo è un risultato comprensibile ed in linea con le previsioni, proprio per questo motivo nel caso D è stato impostato un valore di permeabilità isotropo per la bobina e pari a K_T . I due campi di pressione risultano praticamente uguali, come anche il valore del ΔP misurato a cavallo del poroso, che ha una deviazione praticamente nulla (-0.08%) rispetto al caso D ed è pari a 3.91×10^4 Pa. In **Tabella 17** sono riportati i discostamenti tra i due casi D ed E in termini di velocità radiale media ad altezza fissata all'interno del poroso.

Tabella 17: velocità media radiale: deviazioni tra il Caso D ed E

Posizione radiale (m)	Velocità radiale media (m/s)	Discostamento con il Caso D
0.1	1.48×10^{-1}	-0.89%
0.2	7.38×10^{-2}	-0.13%
0.3	3.42×10^{-2}	-0.13%

In conclusione, nel presente lavoro di tesi è stata valutata l'influenza di alcuni parametri sul processo di tintura assistito da anidride carbonica supercritica, ovvero l'influenza della struttura perforata del beam, della portata in ingresso di $scCO_2$ e della permeabilità sul campo di moto del fluido all'interno del tessuto. È stato dimostrato che la velocità della $scCO_2$ si uniforma quasi subito all'uscita dai fori del tubo forato, consentendo di poter semplificare la geometria scelta impostando l'intera superficie laterale del tubo forato come zona di interfaccia con il mezzo poroso. Inoltre, si è osservato che la velocità radiale tende ad aumentare lungo la dimensione assiale della bobina aumentando la portata di $scCO_2$ in ingresso al sistema, riflettendosi in una distribuzione non omogenea del flusso. Questo potrebbe risultare in una colorazione non uniforme del tessuto a parità di altezza all'interno della bobina. Tale comportamento è stato riscontrato in tutto lo spessore del tessuto avvolto sulla trave perforata, ma è più accentuato in corrispondenza dei primi strati. Infine, si è voluto comprendere l'influenza della struttura del tessuto sulla distribuzione della velocità della $scCO_2$ nell'autoclave, e in particolare all'interno della bobina di tessuto. Dalle ultime simulazioni, in cui si è tenuto conto della sola permeabilità del tessuto, si è concluso che alti valori di permeabilità si riflettono in una distribuzione disomogenea della $scCO_2$ nella bobina. Infatti, è stato dimostrato che aumentando la permeabilità del mezzo poroso, la velocità radiale della $scCO_2$ diventa altamente non omogenea crescendo in maniera considerevole lungo l'asse x. Tale risultato può essere importante quando si vanno a processare tessuti molto permeabili come i knitted. È comunque importante ricordare che in queste simulazioni non si è tenuto conto della resistenza inerziale al flusso. Inoltre, il valore di permeabilità considerato

si riferisce alla permeabilità di un solo strato di tessuto; quindi, un interessante miglioramento del lavoro in esame può essere quello di simulare e ricavare il dato di permeabilità assoluta di una struttura multi-layered. Un ulteriore risultato è stato ottenuto considerando non solo la permeabilità ma anche la resistenza inerziale al flusso, che entra in gioco quando le velocità del fluido sono più elevate e quindi non vi è più l'ipotesi di diretta proporzionalità tra ΔP e velocità all'interno del mezzo poroso. Questa condizione interessa la prima parte a contatto con il tubo perforato in cui la $scCO_2$ raggiunge i valori più elevati di velocità. Facendo questa considerazione si è scoperto che la distribuzione della velocità cambia sensibilmente, ottenendo velocità e pressioni molto più omogenee all'interno del tessuto. Da questa osservazione si può concludere che il coefficiente inerziale gioca un ruolo determinante all'aumentare della permeabilità quando la velocità del fluido è più elevata. Inoltre, si è visto che la fluidodinamica del sistema non varia a seconda che il mezzo poroso sia considerato anisotropo o isotropo (in cui si è specificata in ogni direzione una permeabilità del tessuto pari al valore della permeabilità trasversale). Questo è un risultato plausibile perché la componente di velocità più elevata è quella radiale, mentre la velocità assiale risulta relativamente bassa. Di conseguenza, il comportamento del mezzo poroso è regolato dalla sua permeabilità radiale, che essendo minore rispetto a quella assiale, costituisce il maggior impedimento al passaggio del fluido. Tale lavoro è stato inoltre limitato alla valutazione del flusso della $scCO_2$ non considerando la presenza del colorante. Può essere interessante inoltre modellare un sistema multifase e tempo variante, al fine di simulare la permeazione della miscela di $scCO_2$ e colorante all'interno del tessuto. O ancora, come possibile sviluppo futuro, si può provare a ricavare la permeabilità del tessuto aumentando gli strati sovrapposti al fine di capire come questa variazione di permeabilità influisce sulla distribuzione della $scCO_2$ all'interno dell'autoclave. In futuro si può pensare inoltre di riprodurre l'analisi di permeabilità CFD 3D per ricavare i dati caratteristici del tessuto knitted. In tal modo si potrebbe completare il confronto tra le due tipologie di tessuto in termini di distribuzione del flusso all'interno dell'autoclave durante il processo di tintura assistito da $scCO_2$.

Table of contents

1. Introduction.....	1
2. Computational fluid dynamics: applications and theory	3
2.1. Introduction to CFD	3
2.2. The Finite-Volume Method	5
2.3. Governing equations of fluid flow	6
2.3.1. Mass conservation	7
2.3.2. Momentum equation.....	8
2.3.3. Energy equation	9
2.3.4. Equation of state.....	9
2.4. Turbulence	11
2.5. Turbulent flow calculations	12
2.6. Reynolds Averaged Navier Stokes models.....	13
2.6.1. The $k-\varepsilon$ model.....	15
2.6.2. The $k-\omega$ model	16
3. Supercritical fluids and their applications	19
3.1. Supercritical fluids properties	19
3.2. Supercritical CO ₂	20
3.3. Applications of SCFs and their role in the textile processes	21
4. Supercritical CO ₂ dyeing.....	27
4.1. Sustainability and Textile Industries	27
4.2. Supercritical Fluid Dyeing Process	29
4.3. Literature review and commercial developments	32
4.4. CFD simulations of scCO ₂ dyeing systems	37
5. Permeability of fabrics and yarns.....	41
5.1. Fluent porous media model and required inputs.....	42
5.2. Permeability values in CFD simulations of dyeing systems.....	43
5.3. Predictive methods	44
5.3.1. Permeability of yarns.....	44
5.3.2. Permeability of fabrics	46
5.3.3. Permeability of multi-layered textile.....	48
5.4. Air permeability data.....	50

6.	Through-thickness and in-plane permeability: CFD simulations	57
6.1.	Literature review	57
6.2.	Through-thickness and in-plane permeability simulations of a plain woven fabric ..	58
6.2.1.	Through-thickness permeability simulations: setup.....	58
6.2.2.	Through-thickness permeability simulations: results.....	61
6.2.3.	In-plane permeability simulations: setup.....	66
6.2.4.	In-plane permeability simulations: results.....	68
7.	System under investigation: scCO ₂ dyeing apparatus	71
7.1.	Modelling supercritical fluid.....	71
7.2.	Geometry and mesh.....	72
7.3.	Setup of the simulations	77
7.4.	Results and discussion	78
7.4.1.	Grid independence study for the simplified beam configuration.....	78
7.4.2.	Grid independence study for the perforated beam geometry.....	80
7.4.3.	Comparison between perforated beam and the simplified configuration.....	82
7.4.4.	Flow rate sensitivity analysis	88
7.4.5.	Influence of fabric permeability.....	91
8.	Conclusions.....	101
	List of tables.....	103
	List of figure.....	105
	Bibliography.....	109
	Appendix I: Air permeability data.....	115
	Appendix II	118
	Ringraziamenti	119

1. Introduction

In this work the CFD modelling of an industrial dyeing process assisted by supercritical CO₂ is presented. Nowadays supercritical fluids (particularly supercritical carbon dioxide) are often used as an alternative to conventional organic solvents in various processes. Textile industry, being one of the main water consumers and one of the main responsible for its pollution, can obtain some advantages from the use of the supercritical carbon dioxide (scCO₂) as water substitute. These advantages include higher diffusion rates and lower mass transfer resistance, which ensure greater penetration of the dye into the textile and reduce dyeing time. Therefore, in recent decades supercritical fluids (SCFs), and in particular supercritical carbon dioxide, have acquired importance and have been widely studied as "green media" in chemical processes without solvents. Moreover, scCO₂ has all the characteristics of a good solvent: it is non-toxic, non-flammable, economical and easy to remove; in addition, its critical temperature and critical pressure are relatively low ($T_c=31.1$ °C, $p_c=72$ bar). The use of scCO₂ in the dyeing process, besides has a twofold advantage: it can be used to support both the sustainability and a clean production, avoiding the use of water and chemicals. In the scCO₂ assisted dyeing process replacing the conventional solvent (water) by scCO₂ it is possible to reuse both dye and solvent, lowering process costs. The process temperature is generally 130 °C and the pressure can reach up to 30 MPa. The only fully operational process for scCO₂-assisted dyeing on an industrial scale is the one of DyeCoo, a Dutch engineering company.

This thesis work uses computational fluid dynamics, which is widely used in textile technology, to model a textile dyeing process assisted by scCO₂ using the software ANSYS Fluent, by using the geometry and operational parameters of DyeCoo dyeing system as case study. A similar study in literature was conducted by Reji et al. [1] who analysed the flow distribution of CO₂ through a porous beam considering different process conditions. In fact, they studied the influence of the operating pressure, mass flow rate and inlet temperature. They also made a comparison between compressible and incompressible flow through the beam and the influence of the flow reversal condition. However, there are not many studies in the literature dealing with CFD analysis of beam dyeing processes, and even less are those concerning the scCO₂ dyeing of textiles. In the present work, the reactor used by the DyeCoo company was modelled. In the reactor, the fabric is wrapped on a perforated beam. Here the fluid dynamics aspects of the scCO₂ flow through the beam are investigated in order to analyse its distribution inside the fabric. In beam dyeing processes, it is important to achieve an equal distribution of the dye fluid through the porous beam, since a uniform colouration of the material is required. The particular structure of the fabric, which has to be dyed, is taken into account in order to investigate how it could influence this process in terms of distribution of the scCO₂ flux. The company recommends two types of fabrics in this process: woven and knitted. The difference between them is reflected by very different values of permeability. For this reason, fluid dynamic simulations were carried out in order to obtain the value of the permeability of a plain-woven fabric, reproducing the conditions of permeability test traditionally carried out on fabrics.

In Chapter 2 the basic concepts of Computational fluid dynamics are introduced, as well as the theory and its applications to textile technology. A particular attention is given to turbulence and the turbulence models used during this thesis work.

Chapter 3 is mainly focused on supercritical fluids (SCFs), particularly supercritical CO₂, which is used in the process. Properties and applications of SCFs in industrial processes are reviewed, with a special focus on textile processes.

Chapter 4 reports an overview of the sustainability issues in the textile industry. The description of the process with a review of literature and commercial developments is reported. Also, in this chapter the state of the art relating to the CFD studies conducted on this type of process is presented.

The concept of permeability in fabrics is introduced in Chapter 5, where the various analytical methods to calculate permeability are reviewed and some typical values of air permeability of woven and knitted fabrics are reported in order to make a comparison between them.

Chapter 6 explains the setting of the simulations that have been conducted during this thesis to obtain the absolute permeability of woven fabrics. In Chapter 7 it is described how the scCO₂ dyeing plant was modelled, along with the results obtained and the sensitivity tests.

Finally, in the last chapter, general considerations deriving from this work, future challenges and improvements are reported.

2. Computational fluid dynamics: applications and theory

Computational fluid dynamics is widely used in textile technology, especially in those processes where fabrics, yarns or fast-moving fibres are involved. CFD simulations are in fact used to simulate flows through and around textiles and also to simulate a wide range of finishing processes. Another important factor concerning the application of CFD in textile is that some of the technologies usually used in finishing processes or fabric production were developed well before CFD was developed, making CFD an important tool capable of directly improving existing processes [2].

2.1. Introduction to CFD

Computational fluid dynamics is defined as “the analysis of systems involving fluid flow, heat transfer and associated phenomena such as chemical reactions by means of computer-based simulation”. [3] At the basis of the programs that simulate fluid flows there are equations describing fluid mechanics, in particular Navier-Stokes equations, whose complexity requires the use of an iterative numerical approximation to obtain solutions. The time for calculations depends on the specific problem under examination and varies between fractions of seconds and months. Seminal contributions to CFD were given by Rodi and Spalding in 1970, who implemented several algorithms still in use today and by Baliga and Patankar, in 1980. It is only around 1980 that the first commercial CFD software became available. Moreover, the first application of CFD was in the aircraft industries, but few years later, simulations were widely used also in the automotive and the textile industries. [2]

Nowadays, CFD is useful in a wide variety of applications: aerodynamics of aircrafts and vehicles, hydrodynamics of ships, power design, turbomachinery, electrical and electronic engineering, chemical process engineering, external and internal environment of buildings, marine engineering, environmental engineering, hydrology and oceanography, meteorology and biomedical engineering. CFD is particularly attractive to industries because it is highly cost-effective with respect to physical testing. The advantages of using CFD over experiment-based approaches are several, here are reported some [3]:

- The substantial reduction of lead times and costs of new designs,
- the ability to study systems where controlled experiments are difficult or impossible to perform,
- the ability to study systems under hazardous conditions at and beyond their normal performance limits,
- practically unlimited level of detail of results.

Figure 2-1 shows a graphical comparison of costs and benefits in the development of a process done in a traditional way and with simulations. As could be seen a development driven by simulation leads to a faster achievement of the marketability and of the break-even turnover.

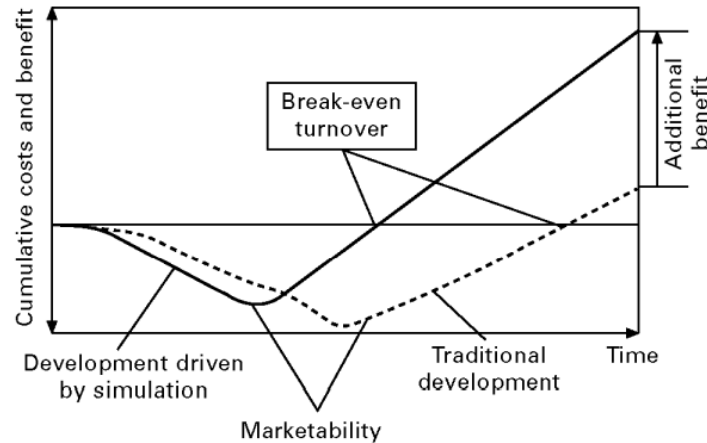


Figure 2-1: Process development by simulation compared to conventional method [2]

In textile technology it is particularly interesting to analyse both the flow and the movement of fibres and yarns inside the flow. This is why coupled simulations are widely used where fibres and yarns move through a stream alternatively. CFD is also used to simulate processes such as melt-spinning, by predicting the polymer flow in order to avoid dead zones or also to achieve the desired filament cross-sections. In melt-electrospinning, where a melted polymer is filled into a syringe and injected into an electrical field to produce fibres of a diameter below 500 nm, the contribution of CFD simulations is linked to the improvement of the distribution of the polymer on the spin pack and to a remarkable lowering of the residence time. Interesting applications of computational fluid dynamics to textile technologies are obtained in the drafting of filaments, in air-jet texturing, in staple fibre spinning and also in fabric production. Moreover, the permeability of fabrics is a subject of great interest, in particular for the outdoor clothing and composite production, where CFD calculations have led to satisfactory agreement with experimental results. These are only a few examples concerning the application of CFD to textile, since today its usage is largely diffuse and has led to a considerable number of studies. [2]

Although the ultimate goal of the simulations can be different, all CFD codes contain three main elements: a pre-processor, a solver and a post-processor. Pre-processing involves first the definition of the geometry of the region of interest (computational domain) and the grid generation. In this phase the physical and chemical phenomena that need to be modelled are also selected, and the fluid properties and boundary conditions are defined. It has to be highlighted that the solution to a flow problem is defined at each cell; in this way the accuracy of a CFD solution is related to the number of cells in the grid (in general with a higher number of cells a better solution in terms of accuracy is reached, but the cost in terms of necessary computer hardware and calculation time are higher, too). The integration of the governing equations over the control volume and the solution of the algebraic equation by an iterative method are parts of the solver, while the post-processor involves various data visualisation tools (e.g., domain geometry and grid display, vector plots, surface plots, particle tracking) [3].

2.2. The Finite-Volume Method

The finite Volume Method (FVM) is the most widely applied technique in CFD, the reason could be found in the conceptual simplicity of this method in which conservation laws in the integral form are discretized directly in the physical space [4].

In a CFD simulation the continuous problem domain is discretized using a grid and, while in the continuous domain each flow variable is defined at every point in the domain, in a discrete domain each flow variable is defined only at the grid points [5]. Usually, the polyhedral or polygons which compose the grid are referred to as “cells” and the grid points are “nodes”. In 2D it is possible also to have triangular cells, in 3D problems the cells are commonly tetrahedrals, hexahedrals or prisms [5]. In the FVM after generating a grid and associating a local finite volume (or control volume) to each mesh point, the integral form of conservation equations is applied to each control volume to get the discrete equations. The finite volume method is in fact based on cell-averaged values. [4]

The integral form of the continuity equation for steady, incompressible flow over the surface S of the control volume (where \vec{n} is the outward normal at the surface) is reported below:

$$\int_S \vec{V} \cdot \hat{n} dS = 0. \quad (2-1)$$

The physical meaning of this equation is that the net volume flow into the control volume is zero [5]. An example of a rectangular cell is reported in **Figure 2-2**:

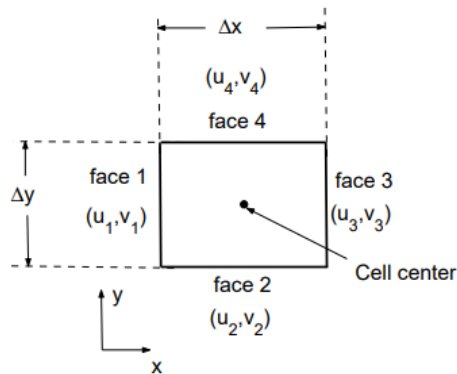


Figure 2-2: Two-dimensional rectangular cell [5]

If we express the velocity at the m -th face in this form: $\vec{V}_m = u_m \hat{i} + v_m \hat{j}$ (where $m=1,2,3,4$), the mass conservation equation (2-1) can be applied to the control volume defined by the cell, giving the following equation [5]:

$$-u_1 \Delta y - v_2 \Delta x + u_3 \Delta y + v_4 \Delta x = 0. \quad (2-2)$$

Eq. (2-2) is the discrete form of the continuity equation for the cell and ensures that the mass is conserved for the cell. Similarly, discrete equations for the conservation of momentum and energy could be obtained for the cell. The method can be easily extended to any general cell shape in 2D or 3D and any conservation equation.

Generally, the discrete equations are applied to the cells in the interior of the domain. For the cells at or near the boundary, a combination of discrete equations and boundary conditions is applied in order to obtain a system of algebraic equations with the number of equations being

equal to the number of independent discrete variables. In order to have a well-defined problem it is important to specify the proper boundary conditions. To solve the equations representing the governing laws of physics an iterative process is done. First a starting value is allocated for velocity, turbulence and pressure to each cell. This initial solution is then converted to the actual solution step-by-step in a convergence process that can be supervised by determining the residuals. Residuals express the variation from the previous iteration: the solution of the linear system has been found if that variation is small enough and so the iterative process can end. Once convergence criteria are met, the flow field will not change anymore and the simulation can be terminated. It is important to properly set the initial values, since the iterative process can be divergent if the initial solution is too far away from the actual solution [2] [4].

One of the crucial factors of the CFD simulations is the grid generation. In fact, the final solution of the simulation could be affected by the choice of the grid and for this reason it is important to perform a grid dependence study. This type of study is relevant in order to eliminate errors that could be caused by the coarseness of a grid. In this procedure a grid is refined until certain key results do not change, making the simulation grid independent [3].

In general, it is possible to distinguish between structured and unstructured grids and the choice between these two types of discretization is based on the properties of the flow solver and on the level of geometrical complexity. In fact, if easily obtained, structured grids are capable to offer the highest accuracy, while unstructured grids have higher flexibility for automatic generation of grids around complex geometries. Since the quality of the mesh could directly affect the accuracy and stability of the numerical computation, it is preferred a high quality of the grid without discontinuities, especially in those regions with high flow variation. [5] [6] [4] For a better understanding of the differences between the two types of grids, **Figure 2-3** reports a graphical representation of a volume with a structured (left) and an unstructured (right) mesh [2].

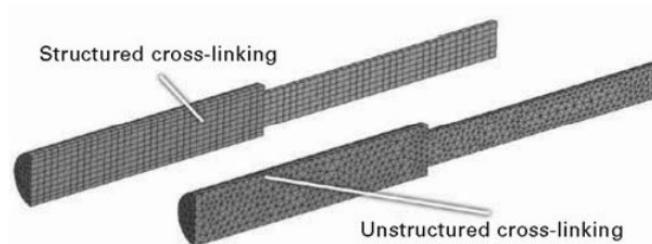


Figure 2-3: Graphical representation of the difference between structured (left) and an unstructured (right) cross-linking [2]

2.3. Governing equations of fluid flow

The mathematical statement of the conservation laws of physics is represented by the governing equations of fluid flow. Indeed, the mass of a fluid is conserved, the rate of change of momentum equals the sum of the forces on a fluid particle (Newton's second law) and, following first law of thermodynamics, the rate of change of energy is equal to the sum of the rate of heat added to and the rate of work done on a fluid particle. [3]

Since the fluid is regarded as a continuum, its behaviour is described in terms of macroscopic properties and the molecular structure of matter and molecular motions are ignored, considering only the macroscopic length scales (1 μm and larger).

For the following equations a small infinitesimal element of fluid with size δx, δy and δz is considered (**Figure 2-4**). The centre of the element is located at position (x, y, z) and the element is small enough so that the fluid properties at the faces can be expressed by a first order Taylor series expansion with respect to the property at the centre [3].

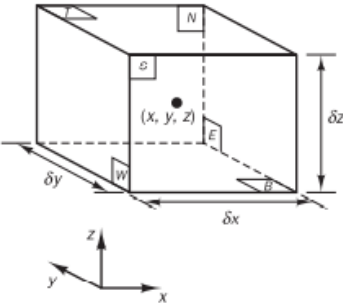


Figure 2-4: Small fluid element for the conservation equations [3]

2.3.1. Mass conservation

In the mass conservation equation in three dimensions the rate of change of mass in a fluid element must be equal to the net rate of flow of mass into the element [3]. The first term, the rate of increase of mass in the fluid element, can be written as:

$$\frac{\partial}{\partial t}(\rho \delta x \delta y \delta z) = \frac{\partial \rho}{\partial t} \delta x \delta y \delta z. \tag{2-3}$$

The mass flow rate across a face of the element is instead given by the product of density, area and the velocity component normal to the face. In particular, flows which are directed into the element produce an increase of mass in the element and for this reason get a positive sign, while flows that are leaving the element are given in a negative sign, as shown in **Figure 2-5**.

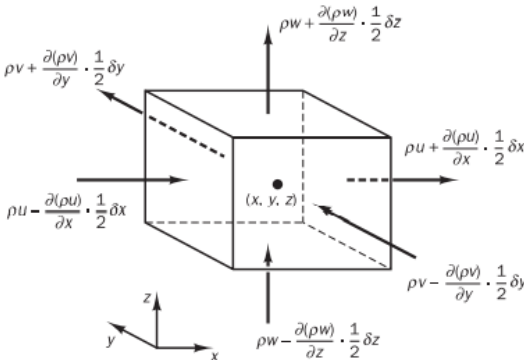


Figure 2-5: Mass flow of the fluid elements (in and out) [3]

Considering together the rate of increase of mass inside the element and the net rate of flow of mass into the element across its faces, moving all terms to the left hand side of the equation and dividing by the element volume $\delta x \delta y \delta z$, the following equation is obtained:

$$\frac{\partial \rho}{\partial t} + \frac{\partial}{\partial x_i} (\rho u_i) = 0. \quad (2-4)$$

Equation (2-4) is known as unsteady, three-dimensional mass conservation or continuity equation at a point in a compressible fluid. For an incompressible fluid, due to the fact that the density is constant, equation (2-4) becomes:

$$\frac{\partial}{\partial x_i} (u_i) = 0. \quad (2-5)$$

Equation (2-4) can be generalized for φ , the value of a property per unit mass [3].

2.3.2. Momentum equation

From Newton's second law it is known that the rate of increase of the momentum of a fluid element equals the sum of the forces on the element [3]. The first term of the equation, that is the rate of increase of x-, y- and z- momentum per unit volume of fluid particle, is given by:

$$\frac{\partial \rho u_i}{\partial t} + \frac{\partial \rho u_i u_j}{\partial x_j}. \quad (2-6)$$

In the momentum equation commonly the contribution of surface forces is separated from the contribution of body forces, which are included as a source term. A fluid element is defined in terms of pressure (p) and viscous stress components (τ). The product of stress and area is the magnitude of a force from a surface stress.

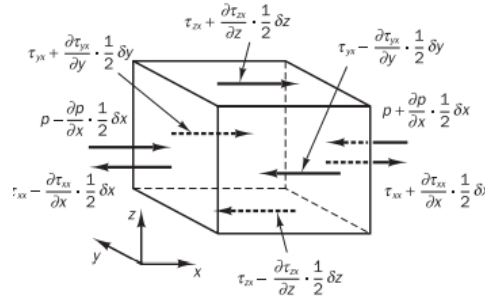


Figure 2-6: x-direction stress component [3]

Setting the rate of change of x-momentum of the fluid particle equal to the total force in the x-direction on the element, caused by surface stresses, it is possible to obtain the x-component of the momentum equation (as shown in Figure 2-6). Similarly, it is possible to obtain the y-component of the momentum equation and the z-component. Here it is reported the general form:

$$\frac{\partial \rho u_i}{\partial t} + \frac{\partial \rho u_i u_j}{\partial x_j} = -\frac{\partial p}{\partial x_i} + \frac{\partial \tau_{ij}}{\partial x_j} + S_{Mi}. \quad (2-7)$$

The source terms S_{M_x} , S_{M_y} and S_{M_z} are related to the contributions of the body forces (centrifugal force, Coriolis force, electromagnetic force). As an example, for a body force caused by gravity these terms will be: $S_{M_x} = 0$, $S_{M_y} = 0$ and $S_{M_z} = -\rho g$ [3].

2.3.3. Energy equation

From the first law of thermodynamics, the rate of change of energy of a fluid element is equal to the rate of heat added to the fluid element plus the rate of work done on the element [3].

The rate of increase of energy of a fluid particle per unit volume is given by:

$$\frac{\partial \rho E}{\partial t} + \frac{\partial \rho E u_j}{\partial x_j}, \quad (2-8)$$

where E is the sum of internal (thermal) energy i and kinetic energy.

The product of the force and velocity component in the direction of the force gives the work done on the fluid particle in the element by surface force. Thus, the total rate of work done on the fluid particle by surface stresses is obtained as:

$$-\frac{\partial \rho u_i}{\partial x_i} + \frac{\partial (u_j \tau_{ij})}{\partial x_i}. \quad (2-9)$$

The rate of heat addition to the fluid particle for heat conduction across element boundaries is given by the following term:

$$\frac{\partial}{\partial x_i} \left(k \frac{\partial T}{\partial x_i} \right). \quad (2-10)$$

Where k is the thermal conductivity.

Once defined a source term of energy S_E per unit volume per unit time, conservation of energy of the fluid particle is ensured by equating the rate of change of energy of the fluid particle (2.8) to the sum of the net rate of work done on the fluid particle (2.9), the net rate of heat added to the fluid (2.10) and the rate of increase of energy given by energy sources. In this way the obtained energy equation is [3]:

$$\frac{\partial \rho E}{\partial t} + \frac{\partial \rho E u_j}{\partial x_j}, = -\frac{\partial \rho u_i}{\partial x_i} + \frac{\partial (u_j \tau_{ij})}{\partial x_i} + \frac{\partial}{\partial x_i} \left(k \frac{\partial T}{\partial x_i} \right) + S_E \quad (2-11)$$

For practical use, equation (2.11) is usually rearranged in terms of enthalpy.

2.3.4. Equation of state

To describe the motion of a fluid in three dimensions a system of five partial differential equations (PDEs) is required. These are: mass conservation, x-, y- and z-momentum equations and energy equation; the unknown thermodynamic variables in this system of equations are: ρ (density), p (pressure), h (specific internal enthalpy) and T (temperature). The link between these four variables can be obtained through the assumption of thermodynamic equilibrium. In particular, equations of state relate state variables to the others [3].

For a perfect gas the useful equations of state are:

$$p = \rho R T \text{ and } h = C_p T. \quad (2-12)$$

For compressible fluids “the equations of state provide the link between the energy equation on the one hand and mass conservation and momentum equations on the other” [3], due to the fact that density can change with pressure and temperature in the flow field. In this work, a supercritical carbon dioxide dyeing process has been modelled using the software Ansys Fluent. In order to evaluate thermodynamic and transport properties of supercritical carbon dioxide, the NIST real gas models on Fluent has been selected. The latter uses the National Institute of Standards and Technology (NIST) model which incorporates the equation of state for carbon dioxide of Span and Wagner. This is a so-called “fundamental” equation of state that relates Helmholtz free energy with temperature and density. The argument is more deeply discussed in Chapter 7.

2.4. Turbulence

Laminar flow and turbulent flow are two different states of motion easily identified and distinguished. Laminar flow is characterized by “smoothly varying velocity fields in space and time in which individual “laminae” (sheets) move past one another without generating cross currents” [5]. This state of flow occurs at low-to-moderate values of the Reynolds number. The behaviour of turbulent flow contrasts with that of laminar flow. Turbulent flows “are characterized by large, nearly random fluctuations in velocity and pressure in both space and time” [5]. They occur at high Reynolds numbers and are characterized by the fact that the fluctuations grow until nonlinear interactions cause them to break down into finer and finer whirls that eventually are dissipated by viscosity. For this reason, turbulent flows develop a chaotic and random state of motion, where velocity and pressure change continuously with time within substantial regions of flow. [4] [3]

The Reynolds number of a flow is calculated as UL/ν where U and L are characteristic velocity and length scales of the mean flow and ν is the kinematic viscosity. This number gives a measure of the relative importance of inertia forces (which are associated with convective effects) and viscous forces. It has been observed that at values below the critical Reynolds number (Re_{crit}) the flow regime is laminar and the flow is steady if the applied boundary conditions do not change with time. Instead, a complicated series of events takes place at values of the Reynolds number above Re_{crit} . These events eventually lead to a radical change of the flow character: in fact the final state of the flow is random and chaotic. In this case even with constant imposed boundary conditions the motion becomes intrinsically unsteady. This regime, where the velocity and all other flow properties vary in a random and chaotic way, is turbulent flow.

Due to the random nature of a turbulent flow a detailed description of the motion of all the fluid particles is precluded. Instead the velocity, is decomposed into a mean value (U) with a fluctuating component $u'(t)$, hence: $u(t) = U + u'(t)$. **Figure 2-7** shows this behaviour:

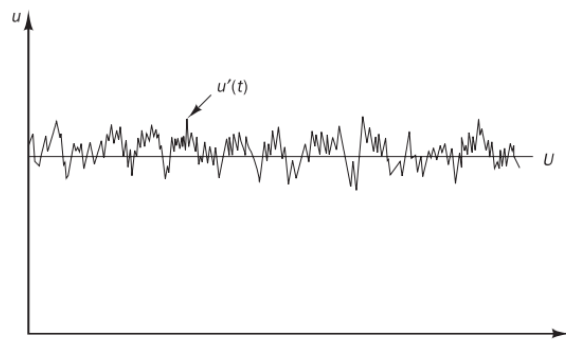


Figure 2-7: Turbulent flow: a typical point velocity measurement [3]

Hence, a turbulent flow could be characterized in terms of the mean values of flow properties and statistical properties of their fluctuation, following the Reynolds decomposition. Turbulent fluctuations always have a three-dimensional spatial character: in fact, visualisations of turbulent flows reveal rotational flow structures (turbulent eddies). For the Reynolds decomposition a flow property at this point is the sum of a steady mean component

and a time varying fluctuating component, with zero mean value. A formal definition of the time average or mean (Φ) is the following:

$$\Phi = \frac{1}{\Delta t} \int_0^{\Delta t} \varphi(t) dt, \quad (2-13)$$

Δt has to be larger than the time scale associated with the slowest variations (due to the largest eddies) of the property φ .

This definition of the mean of a flow property is adequate for steady mean flows. In time-dependent flows the mean of a property at time t is taken to be the average of the instantaneous values of the property over a large number of repeated identical experiments: the so-called ‘ensemble average’. The time average of the fluctuations φ' is, by definition, equal to zero. [3]

2.5. Turbulent flow calculations

Governing equations for turbulent flows are the same as for laminar flows. However, the solution is clearly much more complicated when dealing with turbulence. Numerical methods to capture the important effects caused by turbulence can be grouped into the following three categories: direct numerical simulations (DNS), turbulence model for Reynolds Averaged Navier Stokes (RANS) equations and large eddy simulation (LES) [3].

- DNS uses the speed of modern computers to numerically integrate the instantaneous Navier Stokes equations; these equations are solved on spatial grids sufficiently fine in such a way that they can resolve all the scales of turbulence. Also, they use sufficiently small time steps in order to resolve the period of the fastest fluctuations. In this way DNS solves all the spatial and temporal fluctuations, without the use of modelling. For this reason, DNS remains limited to very simple geometries and is extremely expensive to run, in fact it is not used for large-scale industrial problems. [3] [5]
- RANS equations aim at finding a solution for the mean flow field. The attention is focused on time averaged quantities, because they vary smoothly in space and time and for this reason are easier to solve; they require modelling to “close” the equations in order to consider the effect of turbulence on the mean fields. In fact, extra terms appear in the time-averaged flow equations for the interactions between various turbulent fluctuations. Moderate computing resources are required for reasonably accurate flow computations, but also these models may introduce significant error into the calculation. [3] [5]
- Large eddy simulation (LES) tracks the behaviour of the larger eddies. Space filtering of the unsteady Navier–Stokes equations is done prior to the computations. With this approach the smallest scales of turbulence are approximated or modelled, while large scales are solved. Non-stationarity of turbulence is conserved and the computational cost is lower than DNS. [3] [5]

Most CFD packages (including Fluent) solve the Reynolds Averaged Navier Stokes (RANS) equations.

2.6. Reynolds Averaged Navier Stokes models

The RANS method for turbulence averages all the non-stationarity, in this way the attention is therefore focused on average flow fields and the effects of turbulence on average properties. RANS equations are obtained by introducing the Reynolds decomposition in the Navier-Stokes equations for an incompressible fluid. [4] Thus, settings:

$$u_i = \bar{u}_i + u_i', \quad (2-14)$$

$$\varphi_i = \bar{\varphi}_i + \varphi_i', \quad (2-15)$$

We can obtain:

$$\frac{\partial \rho}{\partial t} + \frac{\partial}{\partial x_i} (\rho u_i) = 0, \quad (2-16)$$

$$\frac{\partial}{\partial t} (\rho u_i) + \frac{\partial}{\partial x_j} (\rho u_i u_j) = -\frac{\partial p}{\partial x_i} + \frac{\partial}{\partial x_j} \left[\mu \left(\frac{\partial (u_i)}{\partial x_j} + \frac{\partial (u_j)}{\partial x_i} - \frac{2}{3} \delta_{ij} \frac{\partial (u_l)}{\partial x_l} \right) \right] + \frac{\partial}{\partial x_j} (-\rho \overline{u_i' u_j'}) \quad (2-17)$$

In equation (2-14) \bar{u}_i and u_i' are the mean and fluctuating velocity components, while φ in equation (2-15) indicates a scalar, such as pressure, energy, or species concentration. [7]

Equations (2-16) and (2-17) are the Reynolds-averaged Navier–Stokes equations. RANS equations have the same shape as the instantaneous Navier-Stokes equations but are written for the mean flow. Moreover, the averaging process involves six additional turbulent stresses: three normal stresses and three shear stresses, here reported.

$$\tau_{xx} = -\rho \overline{u'^2}, \quad \tau_{yy} = -\rho \overline{v'^2}, \quad \tau_{zz} = -\rho \overline{w'^2}, \quad (2-18)$$

$$\tau_{xy} = \tau_{yx} = -\rho \overline{u'v'}, \quad \tau_{xz} = \tau_{zx} = -\rho \overline{u'w'}, \quad \tau_{yz} = \tau_{zy} = -\rho \overline{v'w'}, \quad (2-19)$$

These additional stresses are known as Reynold stresses ($-\rho \overline{u_i' u_j'}$). The three normal stresses (2-18) involve the variances of the x-, y- and z-velocity fluctuations. These stresses are always non-zero: because they contain squared velocity fluctuations, while shear stresses contain second moments associated with correlations between different velocity components. Also, when a transport equation for an arbitrary scalar quantity is derived, extra turbulent transport terms arise.

If the assumption of constant density is not valid, the mean density may vary and the instantaneous density always exhibits turbulent fluctuations.

For variable-density flows, Equation (2-16) and Equation (2-17) can be interpreted as Favre averaged Navier-Stokes equations with the velocities representing the density weighted or Favre-averaged values. [7] Usually, in this notation the tilde symbolize a density weighted variable, while the overbar indicates a time-averaged variable.

$$\frac{\partial \bar{\rho}}{\partial t} + \frac{\partial}{\partial x_i} (\bar{\rho} \tilde{u}_i) = 0, \quad (2-20)$$

$$\frac{\partial}{\partial t} (\bar{\rho} \tilde{u}_i) + \frac{\partial}{\partial x_j} (\bar{\rho} \tilde{u}_i \tilde{u}_j) = -\frac{\partial \bar{p}}{\partial x_i} + \frac{\partial}{\partial x_j} \left[\mu \left(\frac{\partial (\tilde{u}_i)}{\partial x_j} + \frac{\partial (\tilde{u}_j)}{\partial x_i} - \frac{2}{3} \delta_{ij} \frac{\partial (\tilde{u}_l)}{\partial x_l} \right) \right] + \frac{\partial}{\partial x_j} (-\bar{\rho} \overline{\tilde{u}_i' \tilde{u}_j'}) + S_{Mi}. \quad (2-21)$$

Turbulence closure models are necessary in order to compute turbulent flows with the RANS equations. These models must predict the Reynolds stresses and the scalar transport terms, thus closing the system of equations for the mean flow fields. In general, a turbulence model is useful when it has wide applicability, accuracy and simplicity. The most common RANS turbulence models are divided in categories based on the number of additional transport equations that need to be solved along with the RANS flow equations. The $k-\varepsilon$ and $k-\omega$ models are those used in this work and they need two additional extra transport equations (for the turbulence kinetic energy and either the turbulence dissipation rate or the specific dissipation rate). [2] [4] [5] [6]

The most used models for turbulence are the mixing length, $k-\varepsilon$ and $k-\omega$ model and are based on the assumption that an analogy exists between the action of viscous stresses and Reynolds stresses on the mean flow. If a fluid is Newtonian, the viscous stresses are proportional to the rate of deformation of the fluid elements, and for an incompressible fluid it is possible to write the following relation:

$$\tau_{ij} = \mu_{ij} = \mu \left(\frac{\partial u_i}{\partial x_j} + \frac{\partial u_j}{\partial x_i} \right). \quad (2-22)$$

Since it was found that turbulent stresses increase as the mean rate of deformation increases, Boussinesq proposed that Reynolds stresses might be proportional to mean rates of deformation, namely:

$$\tau_{ij} = -\rho \overline{u'_i u'_j} = \mu_t \left(\frac{\partial \overline{u}_i}{\partial x_j} + \frac{\partial \overline{u}_j}{\partial x_i} \right) - \frac{2}{3} \rho k \delta_{ij}. \quad (2-23)$$

In eq. (2-23) k states for the turbulent kinetic energy per unit mass and μ_t is the turbulent or eddy viscosity in Pa s; δ_{ij} is the Kronecker delta ($\delta_{ij} = 1$ if $i = j$ and $\delta_{ij} = 0$ if $i \neq j$).

The Boussinesq hypothesis has the advantage of relatively low computational cost associated with the computation of the turbulent viscosity. A disadvantage of the Boussinesq hypothesis is related to the assumption of isotropic turbulent viscosity μ_t , namely the ratio between Reynolds stress and mean rate of deformation is the same in all directions. The assumption of μ_t as an isotropic scalar quantity is not strictly true, however works well for shear flows dominated by only one of the turbulent shear stresses. It is worth to remind that this assumption leads to inaccurate predictions in many complex flows. There is also an alternative approach: solving transport equations for each of the terms in the Reynolds stress tensor. This approach requires an additional scale-determining equation and is traduced into five additional transport equations in 2D flows and seven additional transport equations in 3D. This latter method is referred as Reynolds stress model (RSM).

It is well known that RANS models are suitable for many engineering applications and typically provide a suitable level of accuracy. But, due to the fact that none of the turbulence models is universal, the first task is choosing the right turbulence model for the problem under investigation. Indeed, the choice of the turbulence model depends on the physics of the flow, the level of accuracy required, the available computational resources and the amount of time available for the simulation. Here the main characteristics of the two model which are used in the present work are reported.

2.6.1. The k - ε model

This model focuses on those mechanisms that affect the turbulent kinetic energy. The transport equations (PDEs) which are solved in the k - ε model are two: one for the turbulent kinetic energy (k) and another for the rate of dissipation of turbulent kinetic energy (ε). The description of turbulence of this model takes into account the effects of transport of turbulence properties (due to convection and diffusion) and the production/destruction of turbulence. [4] [5]

In the k - ε model the k equation is solved in the whole domain including the wall-adjacent cell (using specific boundary condition for k imposed at the wall). [6] The wall boundary conditions for the solution variables, which include mean velocity, temperature, species concentration, k , and ε , are all taken care of by wall functions [6]. These are defined as a set of semi-empirical formulas and functions which link the solution variables at the near-wall cells and the corresponding quantities on the wall. Wall functions are based on experimental observations in order to adequately describe wall behaviour.

Standard, RNG, and Realizable k - ε model have similar forms and the major differences are the method for the calculation of turbulent viscosity, turbulent Prandtl numbers governing the turbulent diffusion of k and ε and finally the term of generation and destruction in the ε equation.

The standard k - ε model was proposed by Launder and Spalding in 1974 [2] and it is popular in industrial flow and heat transfer simulations due to its robustness, economy, and reasonable accuracy for a wide range of turbulent flows. The model was derived from phenomenological considerations and is a semi-empirical model. The assumption done in the derivation of this model is that the flow is fully turbulent and that the effects of molecular viscosity can be neglected. For this reason, the standard k - ε model is valid only for intense turbulence.

Below are reported the transport equations for the turbulent kinetic energy (k) and its rate of dissipation (ε) (in Einstein notation):

$$\frac{\partial(\rho k)}{\partial t} + \frac{\partial(\rho k u_i)}{\partial x_i} = \frac{\partial}{\partial x_j} \left[\left(\mu + \frac{\mu_t}{\sigma_k} \right) \frac{\partial k}{\partial x_j} \right] + G_k + G_b - \rho \varepsilon - Y_M + S_k. \quad (2-24)$$

$$\frac{\partial(\rho \varepsilon)}{\partial t} + \frac{\partial(\rho \varepsilon u_i)}{\partial x_i} = \frac{\partial}{\partial x_j} \left[\left(\mu + \frac{\mu_t}{\sigma_\varepsilon} \right) \frac{\partial \varepsilon}{\partial x_j} \right] + C_{1\varepsilon} \frac{\varepsilon}{k} (G_k + C_{3\varepsilon} G_b) - C_{2\varepsilon} \rho \frac{\varepsilon^2}{k} + S_\varepsilon, \quad (2-25)$$

where G_k stands for the generation of turbulence kinetic energy due to the mean velocity gradient, G_b is the generation of turbulence kinetic energy caused by buoyancy, Y_M is the contribution of the fluctuating dilatation in compressible turbulence to the overall dissipation rate, $C_{1\varepsilon}$, $C_{3\varepsilon}$ and $C_{2\varepsilon}$ are constants, σ_k and σ_ε are the turbulent Prandtl numbers (respectively for k and ε), and S_k and S_ε are source terms defined by the user.

Moreover, k and ε are used to define the velocity scale ϑ and the length scale ℓ representative of the large-scale turbulence. The definitions are reported below:

$$\theta = k^{\frac{1}{2}}, \quad (2-26)$$

$$\ell = \frac{k^{\frac{3}{2}}}{\varepsilon}. \quad (2-27)$$

The eddy viscosity can be specified applying the dimensional analysis, as reported (C_μ is a dimensionless constant):

$$\mu_t = C\rho\ell v = \rho C_\mu \frac{k^2}{\varepsilon}. \quad (2-28)$$

The value of the constants that appear in the model have been determined from experiments for simple turbulent flows. It has been found that these default values work fairly well for a wide range of wall-bounded and free shear flow. The default values are:

$$C_{1\varepsilon} = 1.44, C_{2\varepsilon} = 1.92, C_\mu = 0.09, \sigma_k = 1.0 \text{ and } \sigma_\varepsilon = 1.3.$$

The RNG $k-\varepsilon$ model it is similar to the previous one, but it has some refinements:

- an additional term in the ε equation that improves the accuracy for rapidly strained flows;
- since the effect of swirl on turbulence is included, there is an enhancing accuracy for swirling flow;
- in contrast with standard $k-\varepsilon$ model, the RNG theory provides an analytical formula for the turbulent Prandtl numbers, σ_k and σ_ε ;
- the RNG theory provides also an analytically derived differential formula for effective viscosity that accounts for low-Reynolds number effects.

The RNG-based $k-\varepsilon$ turbulence model is derived from the instantaneous Navier-Stokes equations with the utilization of a mathematical technique called “renormalization group” [3] (RNG) methods.

The realizable $k-\varepsilon$ model is different from the previous two models because:

- it contains an alternative formulation for the turbulent viscosity;
- a modified transport equation for the dissipation rate from an exact equation for the transport of the mean-square vorticity fluctuation has been derived.
- This method satisfies mathematical constraints on Reynolds stresses which are consistent with the physics of turbulent flows, for this reason is called “realizable”. Recent validations show how $k-\varepsilon$ realizable model provides the best performance of all the $k-\varepsilon$ models, moreover this model was proposed to address deficiencies of traditional $k-\varepsilon$ models.

However, non-physical turbulent viscosities are produced with this model when the computational domain contains both rotating and stationary fluid zone. This represent one limitation of the realizable $k-\varepsilon$ model and is due to the fact that this model includes the effects of mean rotation in the definition of the turbulent viscosity.

2.6.2. The $k-\omega$ model

This model was proposed by Wilcox [3] and the main difference with the $k-\varepsilon$ models is that it uses the specific rate of turbulent dissipation in s^{-1} as second variable. Indeed, the $k-\varepsilon$ models use a length scale and a velocity scale in determining the eddy viscosity, but the rate of dissipation on turbulence kinetic energy ε is not the only possible length scale determining variable and for this reason other models have been postulated, such as $k-\omega$ model. [2] [4] [5] [6] [7]

Using ω the length scale become $\ell = \rho k / \omega$ and the eddy viscosity is given by the following formula:

$$\mu_t = \frac{\rho k}{\omega}. \quad (2-29)$$

A drawback of the Wilcox model is the sensitivity of the solutions to values for k and ω outside the shear layer. Transport equations for the standard k - ω model are here reported:

$$\frac{\partial}{\partial t}(\rho k) + \frac{\partial}{\partial x_i}(\rho k u_i) = \frac{\partial}{\partial x_j} \left(\Gamma_k \frac{\partial k}{\partial x_j} \right) + G_k - Y_k + S_k, \quad (2-30)$$

$$\frac{\partial}{\partial t}(\rho \omega) + \frac{\partial}{\partial x_i}(\rho \omega u_i) = \frac{\partial}{\partial x_j} \left(\Gamma_\omega \frac{\partial \omega}{\partial x_j} \right) + G_\omega - Y_\omega + S_\omega, \quad (2-31)$$

where G_k is the generation of turbulence kinetic energy due to mean velocity gradient, G_ω is the generation of ω , Γ_k , Γ_ω represent the effective diffusivity of k and ω , Y_k , Y_ω represent the dissipation of k and ω due to turbulence and S_k , S_ω are user-defined source terms.

Here are reported the model constants needed to evaluate the effective diffusivity, the generation terms and the dissipation terms:

$$\alpha_\infty^* = 1, \alpha_\infty = 0.52, \alpha_0 = 1/9, \beta_\infty^* = 0.09, \beta_i = 0.072, R_\beta = 8, R_k = 6, R_\omega = 2.95, \\ \zeta^* = 1.5, M_{t0} = 0.25, \sigma_k = 2.0, \sigma_\omega = 2.0$$

and,

$$\Gamma_k = \mu + \frac{\mu_t}{\sigma_k}, \Gamma_\omega = \mu + \frac{\mu_t}{\sigma_\omega},$$

$$\mu_t = \alpha^* \frac{\rho k}{\omega},$$

$$G_k = \mu_t S^2, G_\omega = \frac{\omega}{k} G_k.$$

In these equations, the coefficient α^* is used to damp the turbulent viscosity causing a low-Reynolds number correction and is function of α_∞^* , β_i , R_k , ρ , k , μ and ω . S is the modulus of the mean rate-of-strain tensor, defined in the same way as for the k - ε model, while α is a function of α_∞ , α^* , α_0 , R_ω , ρ , k , μ and ω . The terms ζ^* , β_i , β_∞^* and R_β are required for the calculation of Y_k and Y_ω . [7]

The Shear-Stress Transport (SST) k - ω model was developed by Menter [3]. The reason behind the development of this model was to blend the robust and accurate formulation of k - ω model in the near wall region with the freestream independence of the k - ε model in the far field. For this reason, Menter suggested a hybrid model: in the near-wall region a transformation of the k - ε model into a k - ω model could be used while in the fully turbulent region (far from the wall) a standard k - ε model is adequate. This model follows the Wilcox's original k - ω model for the Reynolds stress computation and the k -equation, but the ε -equation is transformed into an ω -equation by substituting $\varepsilon = k\omega$. An extra source term is present in the equations, i.e., the cross-diffusion term, which arises during the $\varepsilon = k\omega$ transformation of the diffusion term in the ε -equation.

Of course, the SST k - ω model has some differences with respect of k - ω standard model. The modeling constants are different and also the definition of turbulent viscosity is modified to account for the transport of the turbulent shear stress. Moreover, the SST model has a damped cross-diffusion derivative term in the ω equation and a blending function (from which are multiplied the k - ω standard model and the transformed k - ε model, both added together) which

is one in the near-wall region, to activate the standard $k-\omega$ model, and zero away from the surface, to activate the transformed $k-\varepsilon$ model.

3. Supercritical fluids and their applications

Supercritical fluids (SCFs), and in particular supercritical carbon dioxide and supercritical water, have gained importance in the past two decades for several reasons. Indeed, water and carbon dioxide, both in supercritical conditions, have been investigated extensively as green media for applications in solvent-free chemistry processes and green chemistry, but also in environmental remediation [8]. The following sections report more information on the nature of supercritical fluids, and more specifically on the properties of supercritical carbon dioxide. This chapter also contains a review of the industrial applications of SCFs and their role in the textile industry.

3.1. Supercritical fluids properties

More and more frequently in modern technologies it has been made use of supercritical fluids (SCFs). SCFs find different applications at industrial level and the main reason can be found in their low environmental impact. Processes assisted by SCFs include mass-transfer processes, phase-transition processes, reactive systems, materials-related processes, and processes related to nanostructured materials. [9] Here, their main properties and features are discussed.

When a compound is heated and/or compressed it changes its physical state. In particular, when it is heated above its critical temperature and critical pressure, the separation between liquid and gas disappears and a single phase is obtained, which is called critical phase. In that condition if the pressure is raised, the fluid can no longer be liquefied. Hence, the critical temperature of a compound is defined as the temperature above which a liquid phase cannot be formed, no matter the pressure of the system [10]. The critical pressure is defined as the vapour pressure of the compound at the critical temperature [10]. Above the critical point, a compound shows peculiar properties, some typical of a gas and others typical of a liquid. **Figure 3-1** shows a typical phase-diagram for a pure substance, where critical temperature T_c and critical pressure p_c are highlighted.

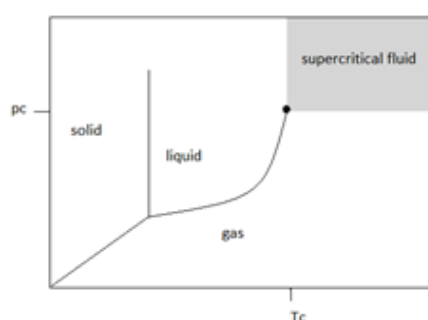


Figure 3-1: Single substance phase diagram

The most important characteristics of a supercritical fluid are the dissolving power and the high adjustability of density, simply by relatively small variations in pressure or temperature. The latter is a major difference with respect to other liquid solvents and ensure an easily tunability of the solvent strength [11].

Other important features of SCFs are the quite low viscosity and the essentially non-existent surface tension. These two characteristics, together with the high diffusivity, lead to interesting mass transport phenomena in condensed phases. Moreover, SCFs influence the properties of other components in a mixture: they are able to dissolve substantially in condensed phases and to dissolve compounds far beyond their vapour pressure. Indeed, SCFs can drastically reduce the viscosity and surface tension of condensed phases, which makes mixture containing supercritical fluid free to move in pores and tiny structures [9].

3.2. Supercritical CO₂

Between the large number of compounds that can be used as supercritical fluids in various applications and techniques, the most widely used is carbon dioxide. Its large usage in pharmaceutical, nutraceutical and food applications is mainly attributed to the observation that it presents all the characteristics for a good solvent: it is in fact non-toxic, non-flammable, inexpensive and easy to remove. Moreover, its critical temperature and pressure are relatively low and easy to reach ($T_c=31.1\text{C}$, $p_c=72\text{ bar}$). [11]

Below the phase diagram of pure carbon dioxide is reported (**Figure 3-2**).

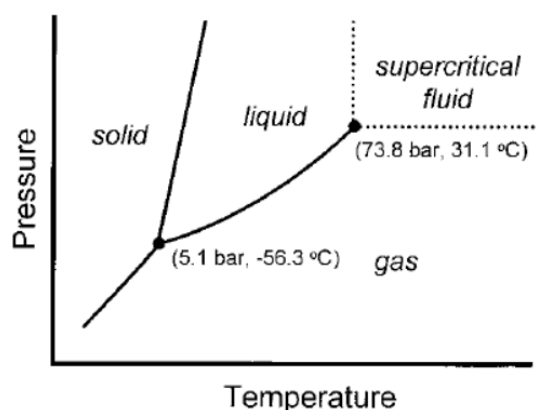


Figure 3-2: Phase diagram of pure carbon dioxide [12]

The previous reported features of carbon dioxide make it a suitable choice for the extraction of thermally labile and non-polar bioactive compounds. In fact, most non-polar molecules are in general soluble in CO₂ in contrast to polar molecules, for which it is still possible the utilization of CO₂ as solvent if an increase in solubility of polar compounds and selectivity of the process is achieved [11] [12]. This could be done by adding small quantities of other solvents in the fluid (namely, cosolvents), obtaining the following advantages: the processing times decrease, yields increase, and it is also possible to use milder processing conditions. However, this addition complicates the thermodynamics of the system and increases capital costs. [11]

Supercritical carbon dioxide (scCO₂) is a sustainable alternative to remarkably reduce, or even eliminate, the necessity of conventional organic solvents. There are numerous examples in the utilization of scCO₂ in different areas, from chemical extraction and purification, to synthetic chemical reactions and inorganic catalytic processes, also biochemical reactions involving enzymes, particle size engineering, textile finishing, and advanced material production. [13]

3.3. Applications of SCFs and their role in the textile processes

A direct effect of the authorities' awareness of the environmental consequences of the utilization of toxic organic solvents, is the research and invention of new and more environmentally safe processes [11]. In recent years, the number of the areas in which SCFs are involved has increased. The most known processes involving SCFs are supercritical fluid chromatography, enhanced oil recovery and the extraction of natural materials (e.g., decaffeination of coffee, tea or the extraction of essential oils). Enhanced oil recovery with carbon dioxide has been an effective application for 35 years. In fact, during 2008 in United States, the barrels per day of mineral oil produced with this technique have been approximately 245,000 [9]. Here some detailed examples regarding the use of SCFs in different processes are reported, from the mass transfer processes to phase-transition processes, reactive systems and material-related processes.

- **Supercritical fluid extraction (SFE)**

The SFE from solids is a process in which a supercritical gas flows through a solid substrate. In this way the product components are extracted from the solid substrate, which in most cases is a fixed bed; then the loaded solvent is fed to a precipitator or separator for recovery of the extracted components. In most cases both the extraction and precipitation are carried out in autoclaves (one or more), used as batch reactors. Simply by reducing pressure and temperature, the precipitation is achieved, and a single step process is designed. Recent commercial application of SFE are the extraction of sesame oil, the cleaning of rice (obtaining large advantages such as the removal of pesticides and heavy metal, destruction of germs and insect eggs, removal of the waxy layer and fatty acids, which are responsible for rice degradation, and ultimately the cooking time is shortened by 30%), cork treatment, scCO₂ extraction of spent rubber tires (in order to create new products from waste rubber granules). [9]

- **Supercritical fluid chromatography**

Another commonly used supercritical technology is supercritical fluid chromatography (SFC), which can be considered a variation of the typical liquid chromatographic separation where the main difference is the replacement of liquid eluent. Main features of the process: the fluid can flow concurrently or counter-currently with the feed, raw material can be added constantly or in batches, the packing can consist of an inert material or typical chromatographic packing materials. [11]

- **Supercritical particle formation, antisolvent precipitation**

Supercritical fluids are used in phase transition processes together with those substances which need to be brought into a certain size and functionality for their utilization. These processes are used for example in pharmaceutical and food applications. [9]

- **Encapsulation and Coating**

Composites belongs with this category; in fact, they are frequently produced by simultaneous precipitation of the core and coating materials. For example, a fluidized bed created with the formulation gas (CO₂) offers different options for the process and, thanks to high extent of heat and mass transfer, constant process conditions throughout the receiving vessel are ensured. Numerous process options are possible, to name a few: precipitation, encapsulation, coprecipitation at controllable conditions, and continuous removal of formulated particles. [9]

- **Supercritical drying, cleaning and degreasing**

In desorption, drying and cleaning some components are removed from solids. In particular, supercritical drying is often used for the production of aerogels from silicon, simply removing an organic substance (e.g., ethanol) with scCO₂. This process is possible thanks to the low surface tension typical of supercritical fluids. The cleaning of all kind of surfaces, even those with micrometric or nanometric structures, is also possible thanks to low surface tension of SCFs, resulting in no solvent residues on the solid materials. Today, scCO₂ cleaning represent a valid alternative to conventional industrial cleaning, giving good cleaning quality at reasonable cost. [9]

- **Impregnation with supercritical fluids**

In this supercritical fluid-based process the key properties of SCFs are their low viscosity and high diffusivity. scCO₂ viscosity is on average 30 to 100 times lower than the viscosity of a liquid, and its high diffusivity coefficient (10^{-2} to 10^{-1} m² s⁻¹) enables its small molecules to diffuse into porous and natural materials. Impregnation of materials such as wood, cork, leather, and fabric fibres, with molecules such as fungicides, polymers, and dyes, is possible with this technique [9].

- **Dyeing**

In textile-finishing industry the scCO₂ dyeing process enables the diffusion of disperse dyes in fibres. The diffusion of disperse dyes strongly depends on the type of dye, and the reason why they are not used in conventional water dyeing processes is that they require too much time for dyeing. On the contrary reactive, direct, and acid dyes, used in water dyeing, are nearly insoluble in supercritical carbon dioxide. Dyeing of polyethylene terephthalate fibres in scCO₂ has been widely discussed for its economic efficiency and practicality, while dyeing of natural fibres (such as cotton) presents already some issues. This occurs mainly because CO₂ is unable to break hydrogen bonds, preventing the diffusion of dyes into fibres such as cotton, viscose, wool and silk. Although these materials present the advantage to be dyed in scCO₂ without any pre-treatment, they require special compounds to be processed [9]. Main features and recent developments of this technique are widely discussed in the next Chapter.

- **Tanning**

Nowadays the leather production involves tanning with chromium for 90% of leather products and it requires much water. A valid alternative of this process could be represented by the utilization of compressed carbon dioxide. Studies have demonstrated how it leads to shorten tanning times, reduction of water effluents and pollution, and save also leather-finishing fats. In addition, the dyeing of leather in supercritical CO₂ is possible, which results in uniform dyeing, good dye penetration, and good dimensional stability. [9]

- **Countercurrent separation**

The separation process with SCFs is recently used in order to separate mixtures of components of low volatility. It has been developed to full commercial scale giving advantages such as moderate temperatures and absence of thermal degradation of components, however the number of applications is still low. [9]

- **Reactive systems**

In many reactions, supercritical fluids are used as a reaction medium or as a reactive component, giving new opportunities to the application of SCFs in catalysis. This is possible thanks to the ability of SCFs to dissolve catalysts in a different way with respect

to typical reaction media. Some examples of this type of applications are the hydrolytic and hydrothermal reactions and oxidative reactions in supercritical water (SCWO) for waste treatment and biomass processing. Also Friedel-Crafts alkylation, hydroformylation, and transesterification of triacylglycerides, where common reactions could be carried out in supercritical CO₂ in continuous flow systems, are performed. [9]

- **Materials-related processes: polymers, emulsions and microemulsions, colloids**

Thanks to its properties, supercritical CO₂ is able to replace organic solvents in polymer processing. Moreover, carbon dioxide can significantly increase free volume and also reduce viscosity and interfacial tension, being a suitable dilution agent for polymer melts. There are many examples of the application of CO₂ in this field, to name a few: the production of fine particles to diffusive impregnation, the continuous blending and extrusion processes, and so on. Another application is supercritical CO₂-assisted melt spinning. In fact, CO₂ can swell into the polymer matrix and extracts low-molecular-weight solvent from the polymer-rich phase. In addition, carbon dioxide can be easily removed from the polymer through evaporation obtaining a pure polymer matrix. Recently also for emulsions, microemulsions, and colloids, the utilization of CO₂ to include insoluble phases has been adopted. [9]

- **Nanostructured materials using supercritical fluids**

Although for most processes involving the preparation of nanostructured materials through SCFs there is no application at the industrial scale yet, SCFs represent a good alternative in the production of functional nanostructured films and materials for the next generation microelectronic, energy conversion, and sensing devices. For example, some reviews have shown how supercritical fluids are a promising technique in the preparation of supported metallic nanoparticles or metallic films, whose application could be found in different areas. [9]

Far from being exhaustive, this was a review of the recent processes, already at the industrial scale or at the pilot scale, which involve SCFs.

Since a very important step forward for world sustainability is the reduction of water consumption and other chemicals in textile processes, SCFs (and in particular supercritical carbon dioxide) are becoming important also for the fashion industry. ScCO₂ is mainly used for textile dyeing but it is not the only technique developed in this field: recently also pre-treatment processes such as scouring, desizing, and different finishing applications have been performed in scCO₂ showing advantages in sight of a more sustainable future. [13] [14]

A detailed description of scCO₂ dyeing process is reported in the next chapter, here some of the application of supercritical carbon dioxide in textile technology concerning pre-treatment and finishing processes are reported.

- **Uses of scCO₂ in pre-treatment applications of textiles**

A common pre-treatment involves surface modification of polyester fabrics in order to have a progression in surface hydrophilicity and wettability, moisturisation efficiency and antibacterial activities (in particular, it has been observed antibacterial activities against *S. Aureus bacteria*).

Scouring is commonly performed before dyeing or printing and the water consumption associated to this processes is really high. A successful scouring of polyester fibers using scCO₂ as medium was performed reaching +99% in oil removal efficiency. In another study, scouring and bleaching feasibility processes for flax rove in scCO₂ media were investigated. For the experiment natural flax rove, system

pressure of 28 MPa and different temperatures (70–80–10–120 °C) for 90 min were used. An eco-friendly process for desizing and scouring of raw (greige) cotton fabric was successfully designed by mixing enzymes in scCO₂ medium for the biodegradation and/or removal of various impurities from the substrate. The operating temperature was set to 50 °C and pressure at 13 MPa for 60 min, resulting in more water and energy conservations than the conventional process, a cost reductions and more environmentally friendly production for cotton fabrics. [13] [14]
In addition, a bleaching process (which is the most important pretreatment process for natural fibres) was performed on knitted cotton fabrics by scCO₂ [13] [14].

- **Uses of scCO₂ in finishing processes of textiles**

In these years, studies on finishing applications in scCO₂ media in order to modify the surface and impregnate the fibre bulk, were conducted. Researchers investigated the use of scCO₂ for impregnation and deposition of additives onto textile because of its strong permeability, which made it an ideal medium for fabric finishing. This leads to obtain textiles for water/oil repellent and antifungal and antimicrobial applications.

In addition, supercritical CO₂ has been used for the production of silver nanoparticle suspensions and might be utilized in medical applications for the coating of textiles with antifungal silver. Imparting antimicrobial functionality to substrates with scCO₂ has some advantages: low operating temperatures, non-flammable processing materials and nontoxic reactants [13] [14].

The scCO₂ could be also used in textile technology for the provision of antifungal functionality of materials, which are used in wound dressings or for medical fabrics disinfection.

Water-/oil-repellent polyester fiber fabrics were also created with the use of supercritical carbon dioxide as medium with a solution of organic fluorine. The results shows that the treated fabrics displayed a good level of water-/oil-repellent characteristics and also the mechanical property of the fabrics were improved. The addition of bioactive components during the dyeing process in supercritical carbon dioxide is used to impart antimicrobial properties to textiles [13] [14].

Another process in which the utilization of scCO₂ brings advantages is the drying of leather; in fact, scCO₂ leads to less energy consumption and higher leather quality, and generally, the products used as leather finishing agents present better solubility in scCO₂. Studies on the use of scCO₂ in silicon-based finishing on cotton fabrics, where scCO₂ is used as medium for the finishing process with modified dimethylsiloxane polymers terminated with silanol groups, were also published [13] [14].

Moreover, in order to achieve high anti-bacteria property, durable to washing, it has been successfully studied the impregnation of chitin and chitosan to polyester (PET) fabric via scCO₂. High antibacterial property of textiles, durable to washing, were reached in these studies, where chitosan–lactic acid salt was effectively applied to polyester fabric resulting in effective impregnation, with exception of chitin that could not be impregnated successfully. After 50 home washing cycles, 70% of the chitosan was still conserved on polyester fabrics, which maintained the antimicrobial properties [13] [14].

Another use of scCO₂ was proposed with electroless plating. Studies reported successfully catalysis and metallization processes via electroless plating in the scCO₂ medium, on both polyamide, as synthetic fiber, and silk, as natural fiber. This technique is useful for various industries, such as health, military, and space industry. Of course, this process has some advantages like the elimination of water

consumption, a reduction in energy consumption and finally a lack of air pollution due to the recovery of utilized carbon dioxide. On the other hand, it is worth to say that machines should be more resistant to pressure to work with scCO₂ and this leads to an high first investment cost [13] [14].

4. Supercritical CO₂ dyeing

Nowadays the research is focusing on processes that will substitute the common organic solvents in different fields, preferring more environmentally safe processes. One of the most polluting industries in the world is textile industry and the environmental problems related to it are several, including water pollution, air pollution and solid waste pollution. In the following sections the role and use of water in textile industries, the principles of the scCO₂ dyeing process and its main features, are discussed. It has also reviewed the state-of-the-art related to the scCO₂ dyeing process and its applications in the field of CFD.

4.1. Sustainability and Textile Industries

Since large amount of water is used as solvent in textile industry, it is well known that fashion industry is one of the biggest consumers of water resources in the world. To be more specific, 60 billion kilograms of fabric per year are produced using 9 trillion gallons of water [13]. This high amount of water is used in the textile industry mainly for the following chemical processes: washing, cleaning, dissolution of dyes and chemicals, scouring and bleaching.

According to the prominent nongovernmental organization Greenpeace International a considerable percentage of global water pollution (around 20%) is made by textile treatment and dyeing [13]. In fact, for the aqueous dyeing procedure, which is the traditional dyeing process used in the textile industry, a large amount of water is required: averagely 100–150 L of water per 1 kg of fiber [15]. Hence, it has to be reminded that large amounts of dyes and other chemicals are used in dyeing processes, which are discharged with wastewater. The latter contains various additives (different salts, surfactants and residual dyes) that make it toxic and hard to biodegrade [16]. Moreover, thanks to their high thermal photostability, dyes can remain in the environment for an extended period of time and, when released into seawater and river, they exercise a destructive action against living organisms. Another consideration that must be taken into account is that on average 60% of the humankind cannot reach clean water resources and also the climate change does not help the already difficult situation. Hence, a more careful consumption of water is needed because it is a limited resource and it is an indispensable source of life. The excellent behaviour of water as a solvent, makes it very difficult to replace, increasing its importance especially in the textile sector, one of the leading consumers. [13]

In this scenario, it is important to give relevance to sustainability, a multidimensional issue, which means “the avoidance of the depletion of natural resources to maintain ecological equilibrium” [13]. Its main pillars are the following: economy, environment, and society. Moreover, a measure of sustainability of a textile process can be obtained through life-cycle assessment, water footprint measurements, carbon emission management, eco design, and clean production [13]. **Figure 4-1** reports a schematic representation of the textile industry impact on the environment.

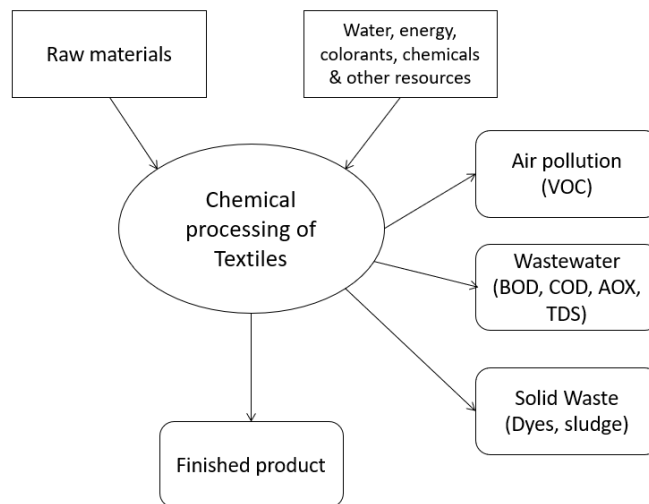


Figure 4-1: Graphical representation of pollution route in textile industry. Adapted by [13]

For these reasons, the needing to find clean solvents to replace water in textile dyeing has emerged; indeed, during these years dyeing techniques with less water consumption or without the use of water (also called waterless dyeing technology) have been investigated by researchers and innovative textile machinery companies [13]. Here some advantages in the utilization of $scCO_2$ in textile applications are reported, particularly dyeing [13]:

- the solvent in excess is easy to remove;
- the density of the solvent can be easily modified;
- it is a nontoxic and sustainable solvent;
- supercritical conditions are easy to achieve;
- there are no greenhouse effects;
- it is good solvent for many nonpolar and low molecular weight molecules;
- it has the possibility to modify functional properties of fibres during dyeing process;
- it helps in reduction of the glass transition temperature of PET.

In conclusion, **Table 4-1** reports a comparison between the conventional process of dyeing (aqueous dyeing) and the supercritical dyeing process. The main advantage in the use of $scCO_2$ dyeing process is undoubtedly the possibility to remove water as dyeing medium, but it shows also a simpler dye formulation, shorter dyeing time and lower energy consumption. Moreover, it is possible to recover in a simple way the unused dye from carbon dioxide: only depressurisation at the end of the process is required. This allows to recycle CO_2 and to obtain directly the final dyed fabric, without drying steps, avoiding an additional high energy-consumption phase [17].

Table 4-1: Differences between conventional aqueous dyeing and scCO₂ dyeing. Adapted by [13]

Conventional dyeing process	scCO₂ dyeing process
Production of large quantity of wastewater (with dyes and other chemicals)	No water needed Dye in excess are in powder form
Difficult chemical recycling	High viability of recycling
The process lasts about 4-6 hours	Rapid coloration: up to 2 hours
Poorly dye efficiency (about 60-85%)	About 99% of dye utilization
More energy required	Less energy required
Small investment, high running costs	Huge investment, low process costs

4.2. Supercritical Fluid Dyeing Process

Schollmeyer was the first who introduced dyeing of textiles using supercritical CO₂ in 1988 [18]. Moreover, a MSc thesis from Ruhr-University of Bochum, in cooperation with G. M. Schneider in 1989, presented the first dyeing experiments of PET (polyethylene terephthalate) in supercritical CO₂ [18].

In this process, the conventional solvent (water) is replaced by scCO₂ and, for this reason this dyeing technique is also called “waterless dyeing” [13].

Supercritical carbon dioxide is suitable for this process due to its low viscosity, in fact a good supercritical dyeing fluid should easily dissolve solid dyestuffs and penetrate small pores structures [19]. As mentioned in the previous chapter, hydrophobic dyes, such as disperse dyes, are ideal candidates for supercritical dyeing because they are easily dissolved in supercritical CO₂ thanks to its liquid-like densities. Since the transport properties are exceptional because of gas-like low viscosities and diffusion characteristics of scCO₂, shorter dyeing times in comparison with an aqueous dyeing counterpart are achieved. Indeed, low-vapour pressure substances, such as dyes, can be dissolved by the liquid-like density and, since in a SCF the viscosity is lower while the diffusion coefficient is bigger than in a liquid, the mass transportation is favourable. In addition, when nonpolar textile materials (such as polyester fibre) are dyed using this technique, the scCO₂ behaves like a swelling agent, which plasticizes the polymer and increases the rate of disperse dye diffusion inside the fibre. [13]

In a typical dyeing process assisted by supercritical carbon dioxide the temperature is set around 130°C and pressures up to 30 MPa, in these conditions the CO₂ density is about 585 kg/m³. Disperse dyes can be fed into the machine along with supercritical CO₂ leading to a uniform distribution of colour both on the surface and in the internal structure of the textile material thanks to the high diffusion of the dye. The most important advantage of dyeing in scCO₂ is the easy separation of solvent and residual dye: the residual dye can be extracted and collected for reuse, making this process more convenient with respect to the conventional one. [13]

Usually, the samples to be dyed are wrapped around a perforated beam suspended inside an autoclave, while the dyestuff powder is placed on the bottom of the vessel. The apparatus is

then sealed, purged with CO₂ and preheated. The compression of CO₂ is then performed ensuring the dissolution of the dyes in carrier fluid (scCO₂) [19]. In a typical scCO₂ dyeing apparatus, once the working pressure is reached, it is maintained until the dyeing process is completed and it requires about 60 minutes in most cases [1]. It has to be highlighted that the average process duration depends on working conditions (temperature and pressure), fibre type, and required depth of shade. [19] In general, referring to recent advance in scCO₂ dyeing process, working temperatures between 80-140°C and operating pressures of 17-29 MPa are used with a variable duration of the dyeing step from 20 to 120 minutes. A typical dyestuff dosage varies between 0.2%-4% on the weight of fibre (wof) [17]. The uniform flow of the dyeing fluid through the porous medium mainly depends on the dye fluid properties, fabric properties, geometric design and flow condition. [1] The final step of the process usually consists in depressurization, which causes the precipitation of the residual dye. In this way, the clean gaseous CO₂ could be collected, and both the compounds (CO₂ and solid dye) can be reused. [13] Generally, the fluid is circulated by means of the circulation pump but is also used the option to reverse the flow in the dyebath from inside-to-outside (I/O) to outside-to-inside (O/I) of the porous material, in order to improve the evenness of dye distribution in the product [17]. These are the basic concepts and procedure of scCO₂ dyeing process, in fact several laboratory-scale and pilot scale equipment have been designed maintaining the same dyeing principles with slight technical and operational difference.

The main parameters affecting the final result are the dye concentration, the working temperature and pressure. To quantify the dye uptake of coloured textiles, the colour strength (K/S) is generally used, while colour fastness can be measured in agreement with textile standards; another parameter often used in literature, is the fixation efficiency (F). Generally, two K/S values are evaluated: “the first one on the just-dyed samples, the second after treating the textiles with an appropriate high temperature solvent extraction to remove the unfixed dye” [17]. F represent the percentage of the initial K/S value that is maintained after solvent extraction, it can be a measure of the percentage of the fixed dye molecules during the supercritical fluid coloration. In general, the dye concentration influences the colour strength in an exponential way, while the diffusion is influenced by temperature. In fact, at high temperatures the dye absorption is higher due to the fact that molecules are more free to move. As said before, the colour strength is influenced mainly by the dye concentration, but also temperature and pressure play a role in this field; moreover, an increase in pressure means an increase in density of the scCO₂, leading to higher dye diffusion [13].

Polyester products show the best results in scCO₂ dyeing due to the structural compatibility of the polyester fiber and the scCO₂ medium: hydrophobic disperse dyes are highly soluble in scCO₂ due to CO₂ hydrophobicity and then penetrate the hydrophobic polyester fibers. The main steps in the polyester dyeing process assisted by scCO₂ are the following [13]:

1. Disperse dye are dissolved in supercritical carbon dioxide.
2. Dissolved dye is transferred to the polyester fiber.
3. Dyestuff is absorbed to the fiber.
4. Dyes diffuse into the fiber.

To sum up, the mechanism that occurs in the disperse dyeing of synthetic textiles allow fibres to be penetrated and swelled by carbon dioxide, facilitating the diffusion of dye molecules. With the depressurisation step, carbon dioxide exits the shrinking fibre allowing the dye to be entrapped in the textile. [20]

The level of dyeing is influenced by each step of the previous mechanisms, which are controlled by the physical properties of the dyes and parameters of the dyeing process (e.g., scCO₂ flow rate, temperature, dyeing time, rate of diffusion). [21]

In fact, the dyeing quality is increased by excellent penetration into the fibre. **Figure 4-2** is a schematic representation of the polyester dyeing process steps in scCO₂ media:

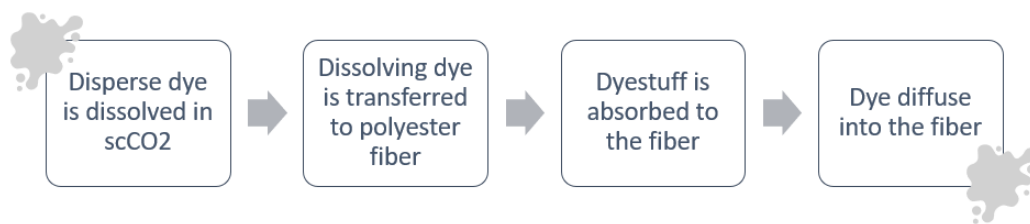


Figure 4-2: Steps of the polyester dyeing process in scCO₂

It is possible to say that the great results of scCO₂ dyeing can be related to the fact that disperse dyes have higher solubility in supercritical carbon dioxide rather than water (where additives must be used to disperse the insoluble dye into the liquor, thus the name "disperse dyes"), moreover scCO₂ can swell and plasticize synthetic fibres [17]

A recent study about scCO₂ dyeing technique discusses the influence of small amount of water in the process: it has been noticed that, under low pressure and temperature, the addition of water in scCO₂ medium makes the process more effective, the reason could be that water interaction leads to a more uniform distribution of the dye, increasing coloration while decreasing colour unevenness. [13]

Non only polyester but also polyamide, PTT, PBT, PP, PLA, and aramid fibres, were dyed successfully in scCO₂ medium such as many natural fibres (wool, cotton, and linen). [13] It has to be said that dyeing of natural fibres is still challenging and there are few papers concerning the dyeing property of cellulose fibres in scCO₂ medium. The main problem is the solubility of the dyestuffs for cotton dyeing (reactive and direct dyes) in the medium. Recent developments show how the textile industry is overcoming this problem: dyeing of cellulose fabrics using Reactive Golden Yellow K-2RA in supercritical carbon dioxide fluid were performed with different amount of water added to the SCF in order to evaluate the influence of humidity on colour strength. The experiment was successful thanks to the reaction in the moist supercritical carbon dioxide involving "monochloro triazine reactive group in the reactive dye and the nucleophilic substitution reaction of the hydroxyl functional groups in cotton" [13]. However, the process is not yet commercially available.

Also, the dyeing of leather using scCO₂ is a promising and innovative technique which can provide better penetration and evenness of dyes. [13]

In a nutshell, it is possible to say that the advantages in the utilization of scCO₂ dyeing process are several and here resumed [19]:

- the complete elimination of water pretreatment and water pollution;
- it is possible to save energy in drying textiles (in fact fabrics are completely dry at the end of the process)
- there is no need of auxiliary agents (no more surfactants or dispersing agents);
- it is reached an high degree of dye levelness
- it is possible to recover easily the residual dyestuff after expansion of the supercritical system;
- it requires very little time;
- for PET, there is no need of after treatment (e.g., reductive washing), making possible to save a complete finishing process;
- it requires a nontoxic solvent, carbon dioxide, of which there is no shortage, it can be obtained from natural sources and it can easily be recycled during the dyeing process;

4.3. Literature review and commercial developments

There is a large variety of scCO₂ dyeing processes reported in literature, using both single dye and dye mixtures, natural or synthetic fibres, yarn bobbins or fabrics. Detailed reviews of these processes and recent developments in this field can be found in literature [17] [22] [23]. Far from being exhaustive, some reviews dealing with recent scCO₂ dyeing apparatuses and commercial developments are reported.

Polyester is the most used material in this field and there are various investigations dealing with its dyeing assisted by supercritical CO₂. To make an example, Schmidt *et al.* [24] examined polyester damage in supercritical carbon dioxide at temperature between 100 °C and 160 °C and pressure of 30 MPa finding that polyester is the most stable fibre and is not affected in supercritical CO₂ up to 160 °C [24]. Hou and Dai [25] also investigated the polyester fabric dyeing in supercritical CO₂ using Disperse Blue 79. It was found that there is a gradual increasing of dye uptake with temperature, reaching equilibrium after 60 min.

Although PET remains the most suitable substrate to be dyed with this technology [17], also dyeing tests on polyamide fibres (e.g., nylon 6), meta-aramid fibres, polypropylene (PP) and ultra-high molecular weight polyethylene (UHMWPE) were conducted. In particular, from the limited studies concerning supercritical dyeing of polyamide fibres resulted that nylon is far less dyeable than PET, mainly because of its higher degree of crystallinity and the presence of polar functional groups (amide group). Meta-aramid fibres show the same difficulty due to their high degree of crystallinity and extremely high glass transition temperature (270°C). In fact, when dyed with conventional methods (water dyeing) specific carriers to promote polymer chain flexibility are required, which brings toxicity issues. To overcome this problem, tests on dyeing of meta-aramid fibres in supercritical carbon dioxide in presence of non-toxic carriers have also been conducted. To sum up, it is possible to say that, among the different synthetic polymers, good K/S and fastness results have been obtained with the coloration of nylon and PP. In fact, a first semi-pilot scale experiment for the dyeing of PP has already been reported in the literature while a pilot-scale coloration of nylon is also under investigation, as has claimed by Femke Zijlstra, the business development manager of DyeCoo, (a Dutch engineering company, leader of waterless textile processing systems) in a recent interview [17].

Hence, it is possible to say that synthetic fibres have been successfully dyed in scCO₂ both on a laboratory scale and in a pilot-scale plant and there are various examples in literature [26] [22] [17].

Natural fibres, have been dyed with synthesized reactive disperse dyes on a laboratory scale [26] but the research in this field is still challenging. In fact, supercritical dyeing of cotton, wool and silk, which are natural hydrophilic fibres, is very difficult with respect to PET dyeing. To be more specific, commercial polar dyes used in conventional aqueous dyeing of natural fibres, are difficult to solubilise because of the non-polar character of supercritical carbon dioxide. Another obstacle is represented by the supercritical environment which does not allow chemical reactions between dye moieties and the functional groups of the textile substrates, which ensure the successful fixation of the colour. [17] Hence, the application of supercritical fluid dyeing technique to natural fibres is difficult and several different methods have been reported in the literature to adapt the process to this purpose [23]. One method is the utilization of CO₂-soluble disperse dyes with reactive group able to react with the cotton fibres by forming chemical bonds. Others approaches are the chemical modification of natural fibres (in order to increase the substantivity of hydrophobic disperse dyes) and the physical modification of the fibre using auxiliary agents (e.g., cotton fabrics were dyed with reactive disperse dyes). A winning strategy seems to be the choice of modifying disperse dyes with appropriate reactive groups which could bind with the textile functionalities [17]. It has to be said that the intensity of coloration of those fibres is still much lower with respect to PET and other synthetic polymers.

One of the developments of the process deals with the research of novel dyes, in order to enlarge the number of supercritical carbon dioxide-soluble dyes, to reach a more economical production or use hypoallergenic molecules. For example, in the literature [17] tests on impregnating a PET fabric with curcumin in laboratory-scale equipment are reported, and good results in terms of K/S and levelness were obtained. However, the application of these natural compounds on synthetic textiles with the conventional method is still challenging: appropriate surface pre-treatment of the fibre and the use of mordant chemicals, are required.

Another innovative purpose is the utilization of dyes able to impart anti-bacterial, fluorescent or photochromic properties to the fabrics. In this regard, recent investigations have demonstrated that the supercritical dyeing technique has started to deal not only with the simple colouring of the fabrics, but also with giving novel functionalities to materials [17], for example the use of fluorescent dyes, which increase colour brightness and visibility of fabrics for the manufacturing of warning clothing (e.g., firefighters, policemen and policewomen). [17] Moreover, also the applications of photochromic textiles cover a wide range of fields from everyday clothing to high-tech smart and functional textiles. One of their advantages is the quick change of colour in response to light although they maintain general textile properties, an example could be found in UV sensing textiles, which show a high flexibility, easy customization and low maintenance compared to conventional sensor systems. [27] Due to their similar molecular structure as the conventional disperse dyes, photochromic dyes could be used in dyeing in scCO₂ medium. Abate et al. [27] investigated the potential application of selected commercial photochromic dyes (i.e., spirooxazine and naphthopyran based dyes) to dyeing polyester fabric using scCO₂ as medium in order to produce UV sensing smart textiles. The authors have successfully incorporated both photochromic dyes into the polyester fabric with a uniform coloration, but distinct characteristics in terms of reaction kinetics, background colour, and wash fastness properties. If exposed to UV light, the fabric samples showed a significant reversible colour changing properties. In addition, they exhibited faster dye kinetics compared to that produced with conventional dyeing techniques.

The authors concluded that a possible utilization of the obtained photochromic fabrics could be as UV sensing smart textile.

Traditionally, textiles material to be dyed were kept in a static mode inside the dyeing vessel, but recent advances show how also a dynamic mode could be performed, bringing some advantages. Examples of those applications are the pilot-scale plant built by Soochow University in 2014 and the industrial-scale multiple plant for the dyeing of PET yarn bobbins by Zheng et al. [15] from Dalian Polytechnic University, but these are not the only ones. In the pilot-scale plant of Soochow University a drive reel (a fabric guide cylinder) magnetically driven by a reversible motor is presented, which allowed clockwise and anticlockwise rotation of the textile inside the dyeing vessel. As result, the mass transfer between supercritical bath and polymer was improved, obtaining also a fast and uniform coloration. [17] The industrial-scale plant described by Zheng et al. [15] shows two vessels (with individual capacity of 500 L) equipped with a rotating bobbing dyeing frame. The latter was composed of different perforated tubes mounted on a rotor device. The dyeing procedure involves both the I/O and O/I external circulation of the fluid and the rotation of the dyeing frame inside the vessel. The plant was also equipped with sensors and high-definition cameras allowing the control of dyeing conditions in the vessels. In this plant, commercially acceptable colour uniformity was achieved and according to the authors, the same dyeing frame can also be used to dye fabrics, garments, skeins and balls.

Finally, Huang *et al.* [26] presented a continuous dyeing processes of zipper tape in scCO₂ with a good quality on a laboratory scale. Two years later, the same Fujian Institute of Research (in cooperation with the University of Chinese Academy of Science and Fujian SBS Zipper Ltd, a major zipper manufacturer in China) also proposed a pilot scale of the continuous dyeing of zipper tape in supercritical carbon dioxide [28]. The continuous process involved two alternative dyeing autoclaves and a simultaneously recycle of gas, lowering the production costs. Its innovation consists in the use of two horizontal dyeing vessels arranged side by side, which resulted in more even fluid distribution with respect to vertical dyeing autoclaves and the main reason is avoiding of dye accumulation at the bottom of the vessel. Although investing in supercritical carbon dioxide dyeing is costly compared to conventional water process, results show that those configurations lead to a significant abatement of the running costs. In particular with a “decrease to ca. 20%- 45% of those of the aqueous process” [17]. In addition higher values of K/S can be obtained with scCO₂ dyeing of zipper tapes with respect to water dyeing, even using a lower amount of dye [17].

To sum up, there are several examples in the literature of laboratory-scale and pilot scale scCO₂ dyeing equipment. Examples of pilot plants using scCO₂ dyeing are: a pilot-scale plant with a capacity of 30 kg of yarn per batch at the Hong Kong Productivity Council and a rope dyeing pilot plant, which uses a special guide tape during the dyeing process [26].

However, it is possible to say that the only fully operational industrial scale scCO₂ dyeing machine is the one built by DyeCoo, a Dutch engineering company. DyeCoo Textile Systems B.V. was founded in March 2008 and is a leader of waterless textile processing systems. [13] [14]

The industrial scale dyeing machine of DyeCoo company is called DyeOx and consists of three dyeing vessels where the fabric is placed wrapped on a beam. The vessel has an open width of 60 or 80 inches, the dyestuff is placed in a separate cartilage which is connected to the beam before the introduction into the vessel for the dyeing process. Each batch has a loading capacity up to 200 kg of fabric and the final products were satisfactory and commercially acceptable, in fact the fabrics dyed in supercritical carbon dioxide medium have a “good wet-wash and rub colour fastness levels (4 to 5 grey scale ratings) and colour

uniformity”. [14] With this innovative technique the uptake and solubility were improved, resulting also in shorter dyeing periods in comparison with the conventional water dyeing process. Moreover, 95% of the carbon dioxide can be recycled after each batch. [14] [17] DyeCoo had a total of 12 dyeing machines operating in Taiwan, Thailand and Vietnam, by the end of 2018. The amount of PET that can be processed by each of DyeCoo dyeing machine is 800 000 kg per year, this allows to an effective saving of 32 million L of water but also to save 160 000 kg of chemicals, which are usually found in discharged water. [17] For these reasons, DyeCoo’s CO₂ technology is the world’s first 100% water-free and process chemical-free textile processing solution [29].

Moreover, sports apparel brand Nike Inc, in 2014, had launched an entire collection of tennis polo shirts dyed using the innovative technique of the “waterless dyeing” in cooperation with DyeCoo. However, one of the possible explanations for the limited diffusion of this technology could be found in the high price tag of the final product. [17] The company has set up collaborations with Nike, Ikea and all large dyestuff suppliers.

Today, with their DyeOx 4, an equipment of 130 tons of steel and pumps, they are able to face a daily nominal capacity of 4000 kg. The DyeOx 4 consists of three dye vessels and it is equipped with an internal electromotor, able to circulate scCO₂ within the pressurized vessel in a closed circuit allowing the recovery of almost 95% of the used CO₂ after every batch and to keep a fixed operating pressure during the entire dye run. DyeOx 4 could be used for different fabric types: woven, non-woven, knitted, yarn, and so on. Moreover, parallel dyeing of knit, woven and yarn are possible; also three separate colours and three separate styles simultaneously could be used. Dyeable materials are 100% PET, No CD-PET and blend only PET dyed while the average dyestuff is 1% wof (on the weight of fibre) [30]. **Figure 4-3** reports a sketch of the reactor used by DyeCoo, while **Figure 4-4** reports the simplified process diagram. The DyeOx 4 dyeing process steps are here reported [29]:

1. The clean fabric is rolled onto a perforated dye beam and loaded into the dye vessel together with pure dye.
2. The liquid CO₂ is released into the vessel.
3. The heat and pressure inside the vessel bring CO₂ to the supercritical state.
4. The scCO₂ and dye are forced through the fabric via perforated beam.
5. Fresh CO₂ is pumped through the machine sending used CO₂ to a separator.
6. In the separator CO₂ is evaporated in order to remove excess dye and residue.
7. The pressure is lowered, and the CO₂ leaves the vessel as a gas.
8. Dyed fabric emerges dry from the vessel, without the needing of additional treatments.

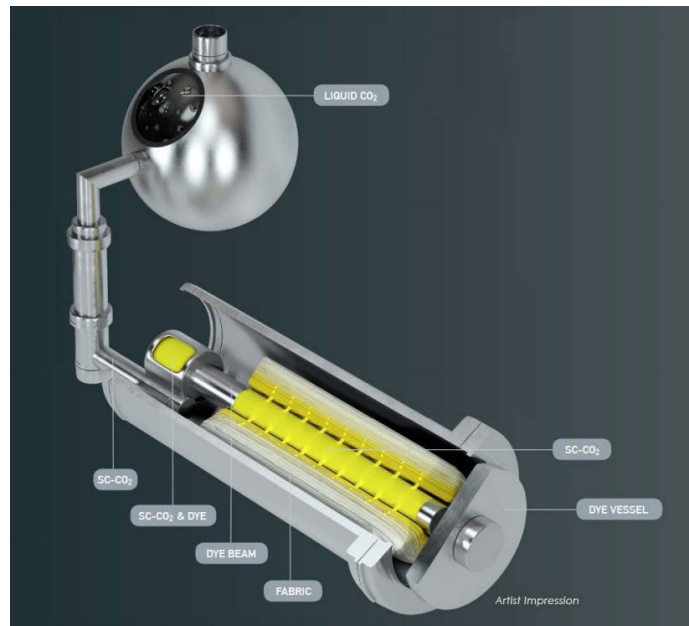


Figure 4-3: DyeCoo reactor [29]

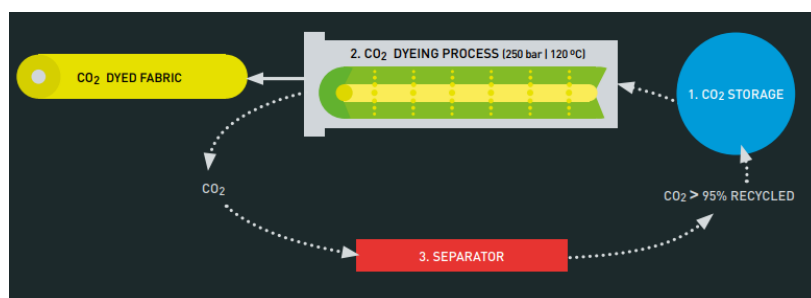


Figure 4-4: DyeCoo simplified process diagram [30]

The problem with this type of technologies seems to be the consumer expectations for inexpensive clothes. Indeed, the fashion industry is “consumer-driven”, so “unless customers are willing to pay more for products made with waterless dye technology, the industry isn’t going to adopt it” [31]. Moreover, it has been reported that Nike, DyeCoo and textile manufacturer Far Eastern New Century (which manufactures ColorDry with DyeCoo machines for Nike) are also working at new processes for dyeing cotton expanding to other material in addition to polyester [31].

4.4. CFD simulations of scCO₂ dyeing systems

The research in this field is mainly finalized to reach uniform coloured textiles as final product of beam dyeing process, which can be achieved ensuring an equal distribution of the fluid through the porous beam. For this reason, the articles in this section are mainly related to the study of the flow distribution of scCO₂, in order to find out the flow characteristics and performance improvement of this kind of process. As above mentioned, CFD is a useful tool in this context and the number of textile processes modelled through this method has been increasing during the last years.

Some authors have studied the behaviour of liquor flow inside a dyeing vessel using computational fluid dynamic. To name a few, Karst *et al.* [32] have highlighted the importance of a collar over the beam surface and side end caps to have uniform flow distribution (their system is discussed in the next Chapter); Scharf *et al.* [33] focused on simulations of a yarn dyeing process on Fluent, modelling the yarn bobbin as a porous medium in order to obtain the pressure and velocity distribution in the vessel. Mancusi *et al.* [34] used numerical simulations to investigate a periodically forced dyeing fluid, modelling convection, dispersion, and adsorption of dye on the threads in a cyclic reversal flow through the bobbins. They also made a comparison between forced and unforced processes, focusing on the dye distribution and the total amount of adsorbed dyes. The results showed how the main effect of the cyclic flow reversal was to enhance a more even dye distribution and dye levelness.

Reji *et al.* [35] studied the theoretical and computational fluid dynamics aspects of beam dyeing to ensure uniform fabric colouring and equal distribution of the dye liquor through the porous beam. They used the commercial software ANSYS CFX based on the finite volume method with a standard $k-\omega$ turbulence model and water as working fluid in the computational domain. For the fabric region a porous medium with isotropic loss model was chosen, with a permeability value of 1.643×10^{-11} m². The simulations are carried out for different values of fluid flow rate. The authors showed the effect of process parameters such as inlet mass flow rate, outlet location, and flow reversal in levelness of dyeing process. Finally, Moreno *et al.* [36] modelled a two-dimensional process of yarn packages dyeing using COMSOL Multiphysics. Their scope was to evaluate the dyeing characteristics of dyeing of acrylic yarn bobbins and it was found that the dyebath flux through the bobbin was related to the dye concentration of the dyebath. Moreover, 1% change of the pressure significantly changed the flow of fluid through the yarn bobbin while 10% variation of the permeability coefficient did not change the flux significantly. In addition, they found out that the value of permeability decreases with the increase of dye concentration in dyebath.

However, the studies related to the computational investigation of the beam dyeing process are few and even fewer are those focusing on the scCO₂ beam dyeing process; the main research concerning a CFD analysis of scCO₂ beam dyeing apparatuses are reported here.

The more interesting research was done by Reji *et al.* [1], who investigated the change of flow distribution of scCO₂ through a porous beam with the variation of the operating parameters (pressure, temperature, mass flow rate). They also made a comparison between compressible and incompressible flow and did simulations under reversed flow condition, in order to find out how these changes in the process affect the flow distribution. As the authors reported, a simple way to reach uniform flow distribution in beam dyeing is achieved with an increase of the main pipe diameter, but for practical reasons it is not convenient. In this study, the scCO₂ beam dyeing machine is simulated as a closed system in which a mixture of dye and dye carrier fluid are pressurized into the beam, enlightening that the flow characteristics depends

on the dye carrier fluid (scCO₂), as the major component in the mixture. Moreover, the performance and the final product quality of the process are mainly influenced by the thermodynamic properties (diffusivity, viscosity and density). The authors evaluated the flow characteristics using three-dimensional CFD and **Figure 4-5** reports the geometry and boundary condition for the system. In this study, the fabric region was considered as a porous medium with isotropic loss model (permeability of $1.643 \times 10^{-11} \text{ m}^2$).

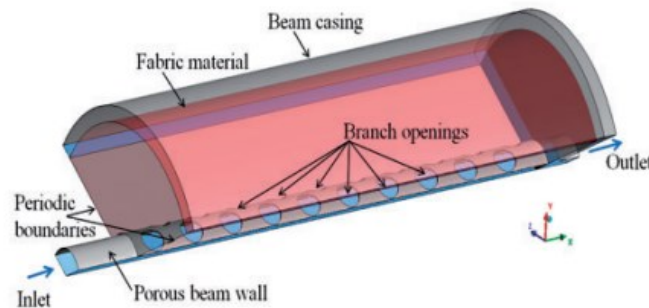


Figure 4-5: Geometry and boundary conditions, Reji et al. [1]

From this investigation, it has been observed that a lower mass flow rate improves levelness, which primarily depends on the uniformity of flow distribution in the beam. They also investigated the distribution of the flow with a reversed flow condition (used in most of the beam dyeing machines), which allows dyeing fluid to flow out through the inlet side, entering from the outlet. They found that the cyclic flow reversal method can significantly improve the levelness in the dyeing process. From this study it can be also seen how the operating conditions, such as pressure and inlet temperature, affect the flow distribution: for a uniform flow distribution, higher operating pressure and lower inlet flow temperature are suggested.

Another study related to the modelling of supercritical fluid flow done by Shannon et al. [37] who considered polyester yarn packages as porous medium (modelled with Darcy's law). They use a 2-D axisymmetric geometry for the numerical flow model with a finite-difference method, in order to predict pressure and velocity profiles of scCO₂ through both isotropic and anisotropic cylindrical yarn packages. It has been reported that "differences in yarn package density result in permeability variations" [37], which are responsible for the different behaviour of the flow within the package; for this reason, the authors utilize experimentally determined permeability correlations, which take into account package density and also supercritical fluid mass flow magnitude and direction. Although this is a very interesting study, it is far from the present examination because it is mainly focused on the fluid flow behaviour through yarns bobbin, while in the present study the focus is on scCO₂ fluid flow through fabrics.

The last relevant study in this field is related to the simulation of CO₂ gas and dyes separation in the separator, which is one of the key components of scCO₂ dyeing process because affects the reutilization of CO₂ but also the whole production. In fact, from a theoretical point of view, scCO₂ can be re-converted into gas after depressurization, allowing the deposition of solid dyes in the separator. An accurate simulation of the flow field in the separator could be achieved with numerical calculation using a reasonable turbulence calculation model and calculation method [38]. It is precisely in this context that the research of Zheng *et al.* [38], which investigated pressure drop and separation efficiency using Fluent15.0 as a software, is

positioned. A pressure-based solver and steady-state solution mode were used in order to perform the fluid area calculation model for a self-developed supercritical CO₂ dyeing apparatus, using also Reynolds stress model for turbulence and SIMPLEC algorithm; the separation efficiency of CO₂ gas and dyes in the separator under different conditions was determined adopting Discrete phase model for the dye particles. A density of 2000 kg/m³ and specific heat capacity of 1680 J/ (kg K) at constant pressure were chosen to model dye particles; moreover, specific boundary condition for particle trajectory tracking were adopted in this study, where particles size followed Rosin-Rammler distribution with an average size of 1 µm. From the numerical calculation it was observed that an increase of the inlet flow rate (from 50 L/h to 2000 L/h) lead to a gradual increase of CO₂ pressure loss at the inlet and at the outlet of the separator. Also, the total separation efficiency of the separator was improved significantly both with an increase of inlet flow and with an increase of particle sizes at constant flow rate. These results could help in the design of the separator for the high efficiency separation of carbon dioxide and dye particles in waterless dyeing processes assisted by scCO₂.

In conclusion, CFD studies concerning scCO₂ dyeing processes are mainly referred to yarn packages and the one related to fabrics adopted an isotropic porous medium to describe the fabric material, ignoring the difference in permeability between the various types of fabrics. Moreover, there are not studies referred to industrial dyeing apparatuses. This could be an interesting field of study in order to see the consistency of fluid dynamic behaviour even for large applications. It would be also interesting to see how specific parameters, such as beam geometry and dimensions, or different fabric structures, could influence the final product quality. By tackling these issues, it would be possible to improve an existing process in terms of dye levelness, colour uniformity, and make it even more convenient.

5. Permeability of fabrics and yarns

In the present work the scCO₂ dyeing system developed by DyeCoo has been modelled using the software Ansys Fluent. In this system textile fabrics are wrapped on a beam and placed inside the dyeing vessel. Here, fabrics are modelled as porous media, the equations used in porous media model and the required inputs for the software Ansys Fluent are specified in the next section.

In the present work the attention is focused on two different types of fabrics, woven and knitted, in order to better understand their behaviour when dyed in scCO₂ medium. Woven fabrics are made by intertwining orthogonally warp yarns and weft yarns. It is possible to have different weave patterns such as plain, twill and satin. A plain weave structure is represented in **Figure 5-1**.

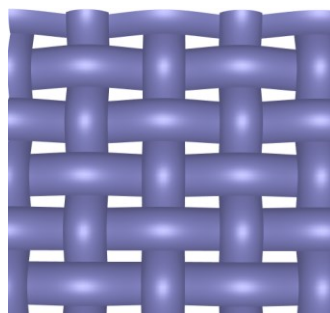


Figure 5-1: Example of a plain weave structure

With the term “knitting” is instead defined the process of forming fabric by interloping yarns in a series of connected loops using needles [39]. According to the direction of a looped thread in the fabric, it is possible to distinguish two main categories of knitted fabrics: warp-knit and weft-knit fabrics. In weft-knit fabrics the looped thread is oriented in horizontal direction (as shown in **Figure 5-2**) while in warp-knit fabrics loops are knit vertically or diagonally. This type of fabric generally has higher air permeability compared to that one of woven fabrics of the same weight and this is related to its loop structure which leads to higher number of pores [40].

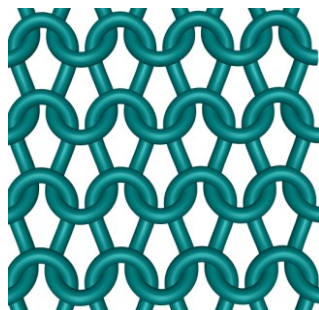


Figure 5-2: Example of a weft-knit fabric structure.

The permeability of woven or knitted fabrics is related to the ability of the fabric to transmit fluids. According to the studies, flow takes place mostly in the spaces between yarns. Indeed,

the inter-yarn pore is the most important parameter for fabrics (although intra-yarn pore also contributes to the total pore volume of the fabric, but it does not affect the flow substantially) [41]. In this work the value of permeability is important to figure out the distribution of supercritical CO₂ inside the fabric. Indeed, a good and homogeneous distribution of the flow inside the porous media is necessary to reach the desirable level of dyeing of the fabric itself. In order to obtain a first attempt value of permeability to set the simulations, literature studies dealing with CFD analysis of a dyeing systems have been reviewed and reported in this chapter. In the next paragraphs also predictive methods for the calculation of fabrics permeability are analysed and a review of articles dealing with the calculation of air permeability for woven and knitted fabrics is presented.

5.1. Fluent porous media model and required inputs

The porous media model on Ansys Fluent can be used for a large variety of single phase and multiphase problems; in this work it is used for modelling the fabric material in a dyeing system.

By applying the porous media model, the pressure loss in the fluid flow is determined according to the momentum equations for porous media, here described [7] [6]; the heat transfer through the medium can also be represented with or without the assumption of thermal equilibrium between the medium and the fluid flow.

The porous media model, in addition to the standard fluid flow equations, has a momentum source term. This source term is composed of a viscous loss term and an inertial loss term. In the following equation

$$S_i = - \left(\sum_{j=1}^3 D_{ij} \mu v_j + \sum_{j=1}^3 C_{ij} \frac{1}{2} \rho |v| v_j \right) \quad (5-1)$$

the viscous loss term (Darcy) is the first term on the right-hand side, while the second term is the inertial loss term, where:

- S_i is the source term for the i^{th} momentum equation
- v is the superficial velocity of the fluid, that is the volumetric flow rate per unit area of the porous medium
- D and C are prescribed matrices.

In the case of simple homogeneous porous media, the equation reduces to:

$$S_i = - \left(\frac{\mu}{K} v_i + C_2 \frac{1}{2} \rho |v| v_j \right) \quad (5-2)$$

where K is the permeability and C_2 is the inertial resistance factor. The actual fluid velocity in the pores is v/ϕ , ϕ being the void fraction (porosity) of the medium.

If the flow through the porous medium is takes place in the creeping flow regime, the constant C_2 can be set equal to zero. In this case the pressure drop is typically proportional to velocity and, ignoring convective acceleration and diffusion, the porous media model reduces to Darcy's law:

$$\frac{\partial P}{\partial x_i} = - \frac{\mu}{K} v \quad (5-3)$$

For the case under investigation, the software requires as input the viscous resistance coefficient (namely, the inverse of absolute permeability, expressed in m^2), the inertial resistance coefficient (C_2) and the porosity of the porous media. In the porous region, the software by default solves the standard conservation equations for turbulence quantities considering that the solid medium has no effect on turbulence generation or dissipation rates. For this reason, in this thesis work, in order to suppress the effect of turbulence in the porous region the Laminar Zone option was enabled.

5.2. Permeability values in CFD simulations of dyeing systems

In this paragraph the literature dealing with CFD analysis of a dyeing system is reviewed in order to obtain the value of permeability to set the simulations.

To characterize the permeability of the fabric to a liquor flow, Karst *et al.* [32] used a *Kretschmer Textiluhr* permeability tester and Darcy's law to calculate the permeability constants in m^2 , as required by the software. Indeed, the fabric beam was specified as porous media with a permeability of $3.964 \times 10^{-12} \text{ m}^2$ in the radial direction and of $4.108 \times 10^{-11} \text{ m}^2$ in the axial direction, parallel to the axis of the beam. They studied the dye liquor flow during beam dyeing to determine in which manner the use of collar placement and end-caps affect liquor flow through the fabric. Both collars and end-caps act as walls impermeable to liquor flow, in particular, end-caps are placed against both sides of the fabric beam. They also studied the behaviour of the system with a condition called *75% leakage*, where the end-cap were not impermeable to the liquor flow and leakage at the end cap was assumed. In this case the permeability constants were set as $1.594 \times 10^{-12} \text{ m}^2$ in the radial direction and $1.643 \times 10^{-11} \text{ m}^2$ in the axial direction.

Reji *et al.* [1] focused on the fluid dynamics aspects of the supercritical CO_2 beam dyeing process at different operating pressure, mass flow rates and inlet temperatures. In this study, the fabric region is modelled as a porous medium with isotropic loss model and permeability of $1.643 \times 10^{-11} \text{ m}^2$.

Shannon *et al.* [37] developed a numerical flow model based on Darcy's law for flow through polyester yarn packages in a supercritical fluid dyeing system. This model utilizes experimentally determined permeability correlations that take into account the package density and supercritical fluid mass flow magnitude and direction. The flow model showed very good agreement with experimental data for O/I (outside-to-inside) flow through the porous material, but only for a specific package density and a volume flow range.

Scharf *et al.* [33] focused on simulations of a yarn dyeing process to provide a deeper understanding of the mechanical flow in the dyeing system. They modelled the yarn bobbin on Fluent as a porous medium with $1/K=3.78 \times 10^{11} \text{ 1/m}^2$.

Moreno *et al.* [36] modelled a two-dimensional process of dyeing yarn packages using COMSOL Multiphysics. They used the model to evaluate the dyeing characteristics of acrylic yarn bobbins, finding that the flux of the dyebath through the bobbin is related to the dye concentration of the dyebath. The authors found that a change of 1% in the pressure significantly changed the flow of fluid through the yarn bobbin while a 10% of variation in the permeability coefficient did not change the flux significantly. Also, they observed a decrease in permeability when the dye concentration in dyebath increases.

All these articles dealt with CFD simulations of a dyeing process but did not investigate the differences between various fabric structures.

5.3. Predictive methods

Fabric permeability is strongly influenced by gaps between yarns, as the easiest path for a fluid which flows through a fabric is between yarns. Indeed, gaps between yarns represent the main flow channel of the fluid. [42] Air permeability is an important factor to consider especially in the studies of the property of clothing. It is defined as the air volume flow rate passing perpendicularly through a unit of fabric area at defined pressure gradient over a time unit. [43] Various research in literature show that permeability of fabrics is related to the geometric structure of fabric and to the path of the fluid through it. In this paragraph a summary of the various theories and mathematical models to predict permeability are presented.

A Newtonian liquid which flows through a stationary porous medium at low Reynolds numbers can be described macroscopically by the Darcy law [44]. Henry Darcy formulated the law on the basis of experiments on the flow of water through beds of sand. The resulting equation is:

$$Q = \frac{KA \Delta P}{\mu L}, \quad (5-4)$$

where Q is the volumetric flow rate, K is the permeability of the porous medium (in m^2), μ is the viscosity of the fluid and $\Delta P/L$ is the pressure gradient and A is the cross-sectional area of the porous medium. In that case, the porous medium was homogeneous and isotropic, the fluid obeys Newton's law of viscosity and the flow behaviour is studied under isothermal conditions. Under these conditions, K was taken as a constant. [45]

Permeability is a property of the specific porous medium and in general, for an anisotropic material, is a tensor. For woven fabrics, the permeability tensor became orthotropic and so there is a principal coordinate system with a principal permeability tensor [42]:

$$[K] = \begin{bmatrix} K_1 & 0 & 0 \\ 0 & K_2 & 0 \\ 0 & 0 & K_3 \end{bmatrix},$$

K_1 and K_2 are the in-plane permeability and K_3 is the through thickness permeability. In general, these three values are different for a textile structure, that is an anisotropic structure.

Moreover, inside a textile, the yarns have two different value of internal permeability. At the yarn level in fact, it is possible to distinguish a permeability along the fibre (K_{\parallel}) and a permeability perpendicular to the fibre (K_{\perp}).

Many authors studied the permeability of fabric and yarns a short summary is reported here.

5.3.1. Permeability of yarns

One of the most known models to describe the flow in porous media is the Kozeny-Carman one, which relates permeability with porosity of the porous medium. Although it was first developed for granular beds, its validity was extended also for porous media consisting of fibres. The Kozeny-Carman equation for beds of granular particles reads as [46]:

$$K = \frac{R^2(1-V_f)^3}{4k'V_f^2}. \quad (5-5)$$

Where k' is the Kozeny constant, R is the radius of the particles and V_f the solid volume fraction. The limit of this equation is that the predicted permeability is isotropic; moreover, research showed that the Kozeny coefficient may vary with the fibre volume fraction for a given fabric [42].

An analytical model for the prediction of permeability in yarns was developed by Gebart [46]. The flow within yarns in fabrics could be reasonably described by this model since it simulated a 2-D flow of a Newtonian fluid in perpendicular and parallel direction with respect to unidirectional filaments [42]. Of course, a real yarn does not have a uniform disposition of fibres inside, but a simple way to describe the arrangement of fibre inside the yarn is to distinguish between hexagonal and quadratic arrangement (both showed in **Figure 5-3** and **Figure 5-4**).

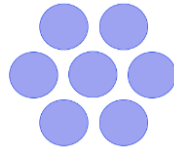


Figure 5-3: Hexagonal fibre packing, adapted by [46]

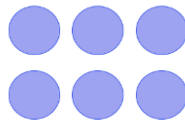


Figure 5-4: Quadratic fibre packing, adapted by [46]

In this way the author, by distinguishing two types of fibre arrays, derived two different equations for the calculation of permeability along the fibres (K_{\parallel}) and perpendicularly to the fibres (K_{\perp}).

$$K_{\parallel} = \frac{8R_f^2(1-V_f)^3}{cV_f^2}, \quad (5-6)$$

$$K_{\perp} = C1 \left(\sqrt{\frac{V_{fmax}}{V_f}} - 1 \right)^{\frac{5}{2}} R_f^2. \quad (5-7)$$

Where R_f is the radius of the fibre and V_{fmax} is the maximum possible fibre volume fraction. The constants $C1$ and c depend on the arrangement of fibres (hexagonal or quadratic). In case of a quadratic arrangement of fibres the values for $C1$, V_{fmax} and c are respectively $16/9\pi\sqrt{2}$, $\pi/4$ and 57, while for a hexagonal arrangement of fibres they are $16/9\pi\sqrt{2}$, $\pi/2\sqrt{3}$ and 53. The assumption of this model are: circular fibre cross-section and specified fibre arrangements. The author also assumed two idealized types of packing of the fibres into a yarn. However, the assumption of constant coefficients gives accurate permeability prediction only for a small range of fibre bundles with high fibre volume fractions (V_f), around 0.7.

Young [47], in a similar way, derived an expression for calculating transverse permeability of yarns depending on fibre volume fraction V_f and radius of the fibres, R_f .

$$K = \frac{R_f^2}{0.8} \left(\sqrt{\frac{0.82}{V_f}} - 1 \right)^3 \left(\frac{0.82}{V_f} \right)^{-1}. \quad (5-8)$$

Berdichevsky et al. [48] reported a self-consistent method and also used finite element simulations in order to estimate the permeability of a fibre bundle. The formulae for longitudinal and transverse permeabilities of aligned fibre bundles were modelled with the continuity theory and the integration of shear stress with the geometric boundary conditions in cylindrical coordinates. The obtained formulae are function of fibre volume fraction and fibre radius (R_f) and were derived for random fibre packing:

$$K_{\parallel} = \frac{R_f^2}{8V_f} \left[\ln \frac{1}{V_f^2} - (3 - V_f)(1 - V_f) \right], \quad (5-9)$$

$$K_{\perp} = \frac{R_f^2}{8V_f} \left[\ln \frac{1}{V_f} - \frac{1 - V_f^2}{1 + V_f^2} \right]. \quad (5-10)$$

Although this methodology could be suited for different fibre packing structures, there was no comparison with experimental data.

The Berdichevsky model was then improved by Later and Cai, making it able to predict the permeability of tight structures containing distributed voids. The flow characteristics of a fibre bundle are well described showing that gaps between neighbouring fibres are the main factors affecting flow resistance in the transverse flow case [42]. The transverse permeability can be calculated as reported:

$$K_{\perp} = 0.229 \left(\frac{1.814}{V_{fmax}} - 1 \right) \left\{ \frac{(1 - \sqrt{V_f/V_{fmax}})}{V_f/V_{fmax}} \right\}^{2.5}. \quad (5-11)$$

The equation depends on two variables, the average V_f value and the maximum packing efficiency (V_{fmax}). The paper showed good agreement with experimental data, but the constant in the derived equation were obtained from curve fitting of experimental data.

5.3.2. Permeability of fabrics

Phelan and Wise [49] determined the macroscopic permeability of unidirectional fabric by studying transverse Stokes flow through elliptical cylinders, which represented yarns. Those cylinders can be treated as a solid or porous material. The main assumption of this model was to ignore the transverse flow velocity components assuming unidirectional flow along the fluid channel axis. Since the scope of the present work it is to investigate the difference in permeability between woven and knitted fabrics, this method is not adequate because it is not directly applicable to woven fabrics. Actually, in that typology of fabrics the flow domain geometry is more complex. For woven fabrics Kulichenko [50] developed an analytical model for through-thickness permeability based on the Poiseuille and Weisbach-Darcy's equations. The author, by simplifying the geometry of gaps in a fabric and after analysis of fabric geometry, found this relation for the predicting through-thickness permeability:

$$K = \frac{\epsilon d_h^2}{80}, \quad (5-12)$$

being ϵ the porosity of the fabric and d_h the hydraulic diameter of the pore. The value of ϵ can be calculated as $\epsilon = A_g/A_u$ (A_g is the area of a gap and A_u the area of a unit cell). The channels in the fabrics were considered as a system of parallel capillaries like straight tubes, **Figure 5-5** shows it graphically.

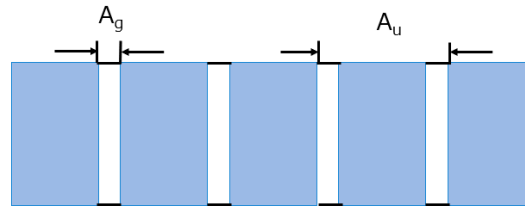


Figure 5-5: Simplified representation of gaps between yarns. Adapted by [42]

This model cannot be used to model textile fabrics accurately due to the fact that it did not consider the curvature of yarn cross-sections, assuming gaps inside fabric as a system of parallel capillaries.

Also Zupin et al. [51] predicted the permeability of one-layer woven fabric by using porosity parameters. In this study the pores were considered circular and in addition the number of macro pores and the total porosity were used for the prediction of air permeability.

Bruschke and Advani [52] [53] developed a model in which the fluid flows through regular arrays of cylinders. A limitation of the model is that cannot predict the permeability over the full porosity range successfully but can only be used for low porosities.

Xiao *et al.* [54] propose an analytical model to predict through-thickness permeability of woven fabric built on viscous and incompressible Hagen–Poiseuille flow. The authors modelled the flow through a unit cell of fabric with a smooth fluid channel at the centre, whose geometry is determined by yarn spacing, yarn cross-section and fabric thickness (**Figure 5-6**).

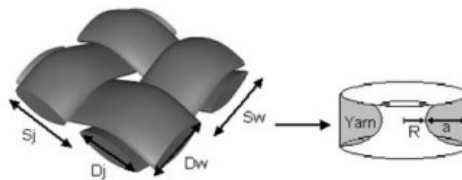


Figure 5-6: Unit cell of fabric and channel geometry [42]

The shape of that channel was approximated by a parabolic function:

$$y = \frac{x^2}{\beta a}, \quad (5-13)$$

where β is a parameter related to the channel geometry, obtained from microscopic measurement. The analytical model was validated with experimental data with very good agreement. Indeed, for most of the sample the comparison with experimental permeability was within 5% errors for most fabrics. They also made a comparison with the model develop by Kulichenko which gives over 60% errors in permeability prediction. This model was suitable for the case in exam except for the fact that only the woven fabric permeability could be found.

Xiao *et al.* [55] also investigated the effect of low air pressure compression (LPC) on through thickness permeability of woven fabric. They found that through-thickness pressure load affects fabric thickness, especially below 200 Pa, resulting in an evident reduction of thickness. Studying these effects on nine woven fabrics, it was found that the LPC reduces the fabric thickness significantly at the initial stage and also that the only factor in determining the variation of fabric through-thickness permeability at the LPC stage is the fabric thickness. Moreover, a linear dependence of through thickness permeability on thickness was found, which was indicated by a linear relationship between air pressure drop and air velocity.

Ogulata and Mavruz [40] created a theoretical model for porosity and air permeability of plain knitted fabrics. The model depends on geometrical parameters, such as the courses per cm, wales per cm, stitch length, fabric thickness, yarn count, diameter of yarn and fiber density. The flow rate of air for a fabric of porous material could be written as the product of the air velocity in pores, the number of pores (m) and the cross-sectional area of the pore. Resulting in:

$$Q = \frac{m\pi d_p^4 10^{-6} \Delta P}{\epsilon 128 \eta t}, \quad (5-14)$$

where d_p is the pore diameter (cm), ϵ the porosity, η the dynamic viscosity of air (Pa*s) and t the fabric thickness (cm). Air permeability can be found simply dividing the flow rate of air Q by the fabric area tested. They compared the predicted permeability with experimental data obtaining an $R^2 = 0.87$. They also noticed that, according to experimental results, the fabrics with the lowest course count per cm and yarn number in tex have the highest air permeability. The loop length also influences the permeability: increasing the loop length increases air permeability.

Referring to the through-thickness permeability of 3D woven fabric Endruweit [56] developed an analytical model. That model was related to the filament count, fibre radius and the angle of the pore axis and the binder in through-thickness tow direction. The analytical model due to the fact that contains a fitting parameter from the experimental data for a particular fabric, cannot predict the permeability directly.

5.3.3. Permeability of multi-layered textile

The studies on multi-layered textiles are mainly dictated by the need to understand how resin flows in a composite production process; in fact, composites are typically made of overlapping layers of textiles.

The in-plane permeability of multi-layered textiles was investigated by Mogavero [57]. He compared experimental results with the effective permeability prediction here reported:

$$\bar{K} = \frac{1}{L} \sum_{i=1}^N l_i K_i. \quad (5-15)$$

In eq. (5-15) K_i is the in-plane permeability of each fabric layer, l_i is the thickness of each fabric layer and L is the total thickness of the preform. From the comparison with experimental data, the effective permeability predictions show average errors between almost 14% and 24%.

An effective through-thickness permeability of multilayer preforms was developed by Chen [58] with a homogenization method by considering interlayer continuity and coupling between in-layer and trans-layer flow. The equation for the calculation of through-thickness permeability is here reported:

$$\bar{K} = \frac{1}{\sum_{i=1}^N (l_i/L)/K_i} \quad (5-16)$$

Also, the author developed an interface layer model from which the effective out-of-plane permeability for a N-layer fabric could be calculated from the following formula:

$$\bar{K} = \frac{N K_{interlayer}}{1+(N-1)\mathcal{L}^2}, \quad (5-17)$$

where \mathcal{L} is equal to 1 for straight channel, major than 1 for a tortuous channel and equal to infinite for non-interconnected channels. While $K_{interlayer}$ depends on the geometry of the channel (S_i , S_{i+1} , S_e , l_i and l_{i+1}) as shown in **Figure 5-7**.

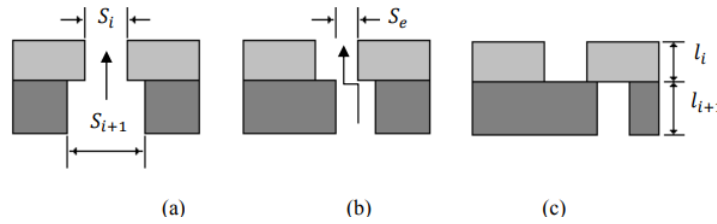


Figure 5-7: Interlayer micro-geometry, Chen et al. (a) straight channel, (b) tortuous channel, (c) non-interconnected. [58]

Good agreement with experimental results was demonstrated.

An analytical model for through-thickness permeability for multilayer fabrics was also developed by Song [59]. This model considers nesting and phase shifting when the preforms were laid up. It depends on the number of layer (N), gap and nesting permeability K_g , fibre-filled region permeability K_f and the fractional area of the channel. The equation:

$$\bar{K} = K_g' \frac{NL}{NL+x_i+\dots+x_{N-1}} A_c + K_f' (1 - A_c). \quad (5-18)$$

It was found by the author that permeability was a function of the number of layers and when the number was more than nine the assembly would show the same permeability.

Xiao [42] also studied the multi-layered woven fabrics air permeability and stated that its value is affected by the number of fabric layers, yarn cross-sectional area, fibre volume fraction of the medium and orientation of the fibres in yarn.

To sum up, the permeability of fibre bundle is a function of fibre radius and fibre volume fraction, one-layer woven fabric permeability is determined by the fabric geometric features (gap shape and fabric thickness), while the 3D woven fabric permeability depends on its internal structure or on the permeability value of each fabric layer. It is noted that there are

various studies on the permeability of porous media analytically, numerically and experimentally, however for one-layer or 3D woven fabrics, no model can predict the permeabilities accurately without fitting factors [42].

Computational fluid dynamics (CFD) can also be an effective tool to predict and model fabric air permeability. Indeed, recently the number of works using CFD for the modelling of fabric air permeability is increasing [60]. Some authors used both CFD simulations and experimental determinations to verify the analytical model. For this type of analysis, a realistic geometric representation of fabrics is essential for modelling properties of textiles and textile composites. Some authors used the open-source software TexGen, developed by the Polymer Composites Group at the University of Nottingham, as a modelling pre-processor for textiles [61].

5.4. Air permeability data

Air permeability is strongly related to the fabric's weight and construction (e.g., thickness and porosity) [62]. It can be defined as the volume of airflow through a specific area under a differential pressure between fabric surfaces; it is usually expressed in cubic centimetre per square centimetre per second [63]. Naming Q the total flow rate of the air (m^3/s), the value of air permeability (R) is obtained by the following equation [40]:

$$R = \frac{Q}{A}, \quad (5-19)$$

where A is the fabric area tested. In this paragraph, a review of studies on air permeability of both knitted and woven fabrics is reported. Complete data about samples, testing conditions and values obtained from these articles are reported in Appendix I.

Zupin *et al.* [64] measured the air permeability of woven fabric samples with the Air Permeability tester *FX 3300 Labotester III (Textest Instruments)* according to the *ISO 9237:1995 (E)* standard. For this purpose, they used 36 woven fabric samples produced using nine frequently implemented weave types together with two warp densities (29.3 and 22 ends/cm) and two weft densities (15 and 20 picks/cm), resulting in four different densities of woven fabrics. The test pressure was set at 200 Pa and the tested area was 20 cm^2 ($\text{L}/\text{m}^2/\text{s}$). In particular, they used cotton yarns and the different samples were indicated with a code: Plain weave (PL), Basket weave (BW), Filling rib 4/2 R4/2, Warp rib 2/4 (R2/4), Twill 1/3 (T1/3), Broken twill 1/3 (BT1/3), Twill 2/2 (T2/2), Broken twill 2/2 (BT2/2), Crossed twill (CT). Weave pattern are usually represented using a squared paper where every column represents one warp yarn while every row represents on weft yarn [65]; when the weft yarn is above the warp yarn, the corresponding square is left uncoloured, otherwise is coloured (often in black). **Figure 5-8** shows the structure of the samples used by the authors for the air permeability tests. **Figure 5-9** reports values of air permeability (R) reported in the article.

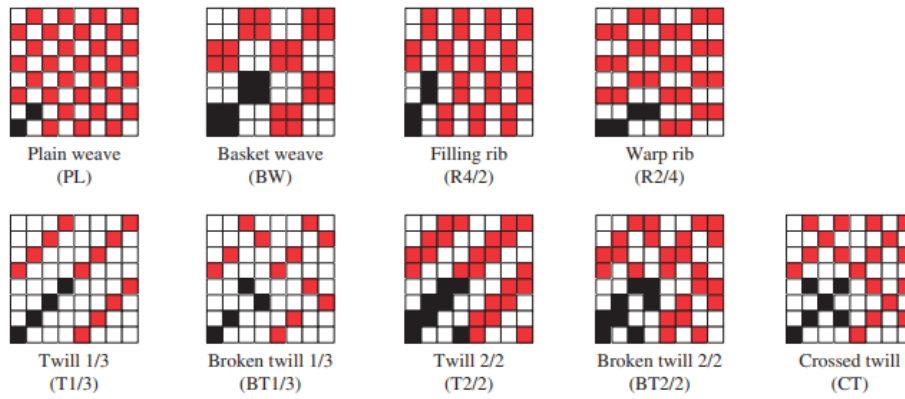


Figure 5-8: Structure of the samples tested by Zupin et al. [64]

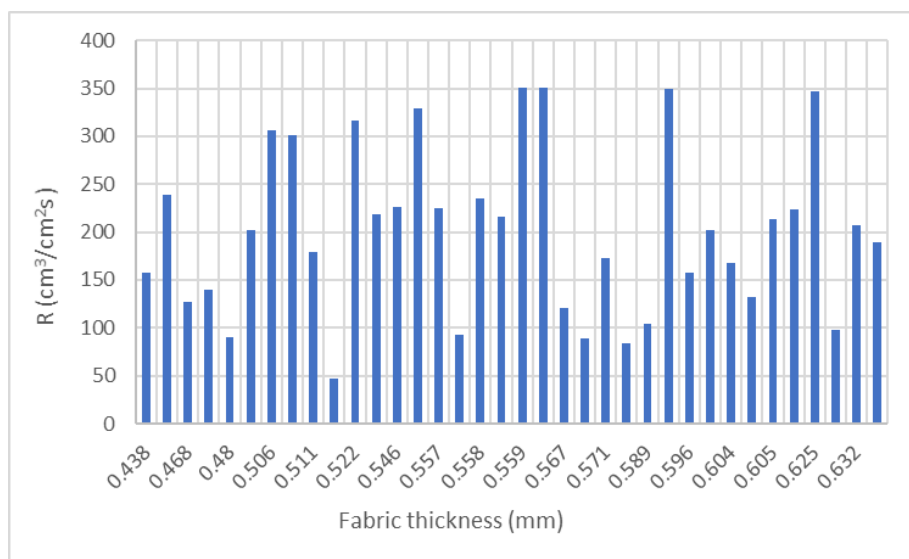


Figure 5-9: Air permeability data from Zupin et al. [66]

Karaca *et al.* [66] investigated air permeabilities of woven fabrics from different cross sectional shaped polyester fibres. They used eight woven fabrics produced in two different weave patterns, which are plain and twill, from polyester yarns of four different fibre cross sectional shapes (round, hollow round, trilobal and hollow trilobal). The fabric air permeability was measured by the authors with a *Textest M821A Air Permeability Tester* according to *TS 391 EN ISO 9237*. The pressure differential was set to 100 Pa. **Figure 5-10** reports air permeability data presented in the article.

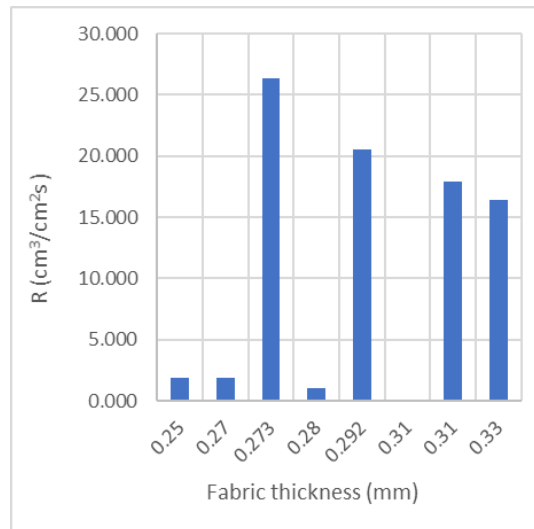


Figure 5-10: Air permeability data from Karaca et al. [66]

Ettehadi *et al.* [67] modelled the fluid flow through a fabric structure using Fluent. In order to compare the result obtained from the simulations with experimental data, they also did experimental analysis of warp-knitted fabrics samples. The samples used by the authors were knitted using 75 denier multifilament polyester yarns composed of 36 monofilaments. They measured air permeability according to BS 5636, with a pressure difference of 100 Pa applied between the two sides of samples (of 0.785 cm² test area). Samples used by the authors are shown in **Figure 5-11**. **Figure 5-12** reports values of air permeability obtained from the article.

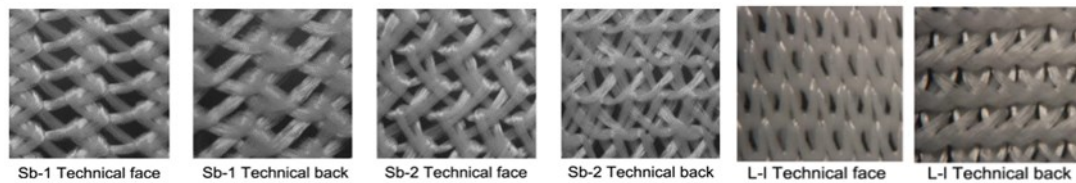


Figure 5-11: Warp-knitted fabrics samples tested by Ettehadi et al. [67]

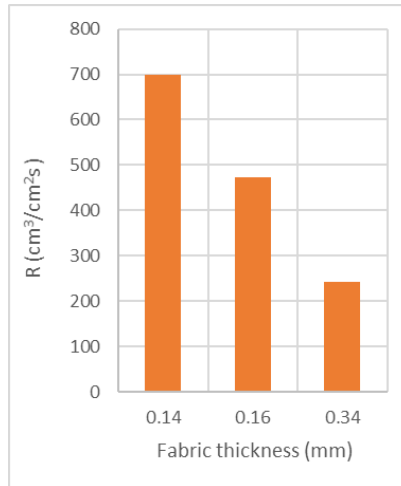


Figure 5-12: Air permeability data from Ettehadi et al. [66]

Dehkordi *et al.* [60] did a similar study, in fact they used CFD to simulate air permeability of knitted fabrics. The authors carried out also air permeability test on all samples. The samples used in this study were knitted fabrics with rib and interlock pattern made on cotton/polyester yarn (30 denier count and 0.22 mm diameter). They reported air permeability tests performed by *Shirley Air Permeability tester* according to *ASTM D737-96 standard*. The test area for air permeability was 78.5 mm² and a pressure difference of 100 Pa was set between two sides of the fabric. Samples used by the authors are shown in **Figure 5-13**. **Figure 5-14** reports air permeability of the samples presented in the article.

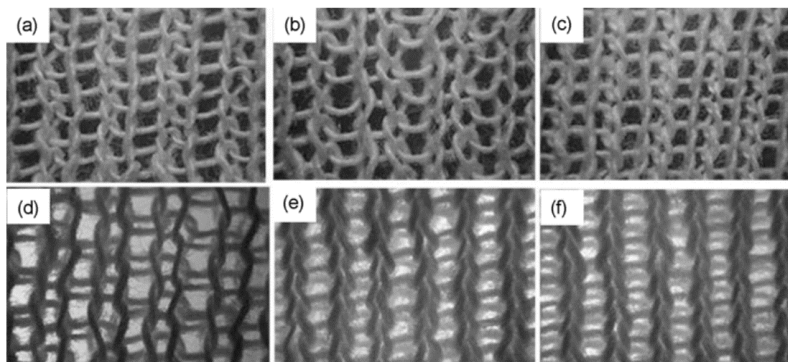


Figure 5-13: Fabrics samples tested by Dehkordi et al. [60]

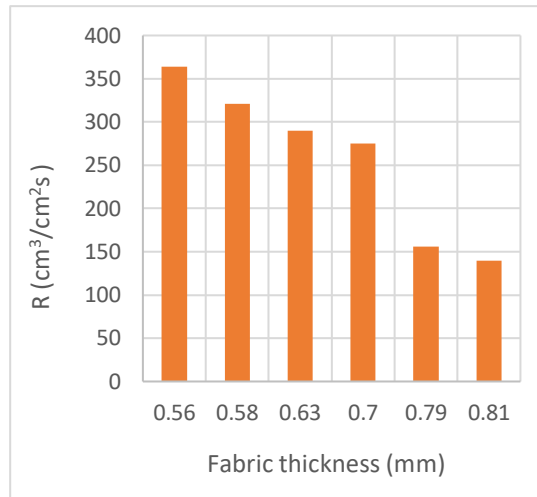


Figure 5-14: Air permeability data from Dehkordi et al. [66]

A graphical comparison between the air permeabilities of woven and knitted fabrics (in m^2) with respect to thickness could be found in **Figure 5-15**. Also air permeabilities of the different types of fabrics against mass (g/m^2) and volume (kg/m^3) are reported in **Figure 5-16** and **Figure 5-17** Those values were obtained from the previous mentioned articles reporting air permeability measurements of fabrics.

On average, within the same range of thickness, air permeability of knitted fabrics seems to be higher than that one of woven fabrics. This behaviour can be observed graphically in **Figure 5-15**. This is an expected result: in fact, as previous mentioned, permeability of fabrics is mainly related to their structure and porosity and knitted fabrics typically present higher porosity compared to woven. Due to their loop structure, knitted fabrics show larger gaps between yarns in a fabric, in which fluids can easily flow:

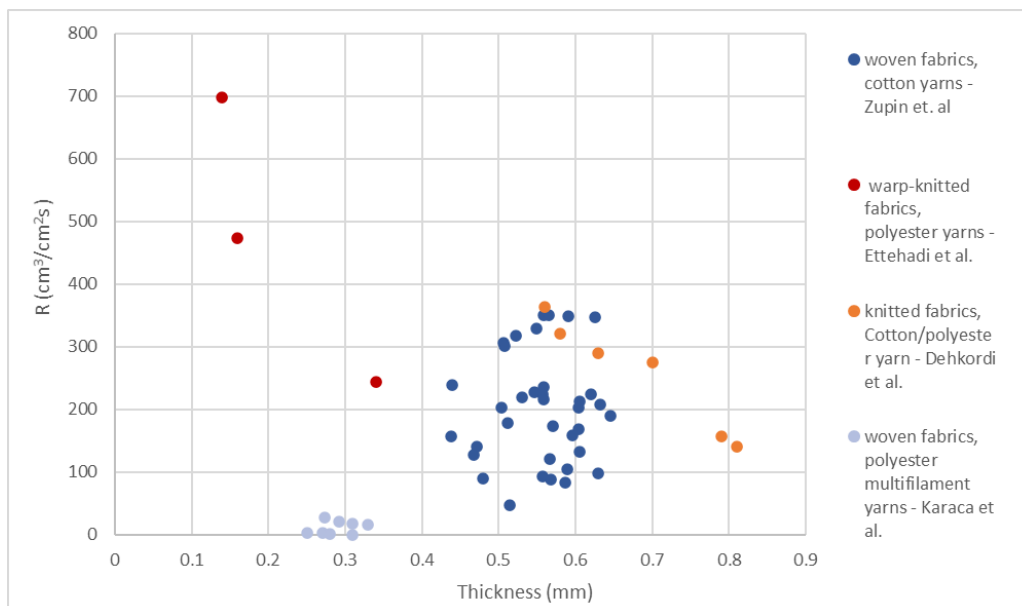


Figure 5-15: Comparison between air permeability of woven and knitted fabrics with different thickness

From **Figure 5-16** it is possible to notice that, between the same range of mass (g/m^2), woven fabrics made on cotton yarns present higher air permeability compared to woven fabrics made on PET. In a similar way, in the same range of mass, knitted fabrics made on cotton-polyester yarns show higher value of air permeability with respect to knitted fabric made on polyester yarns, which also have higher density. Moreover, between the same range of density, air permeability values of woven fabrics are lower compared to those ones of knitted fabrics as expected. This typical behaviour is confirmed by **Figure 5-17**.

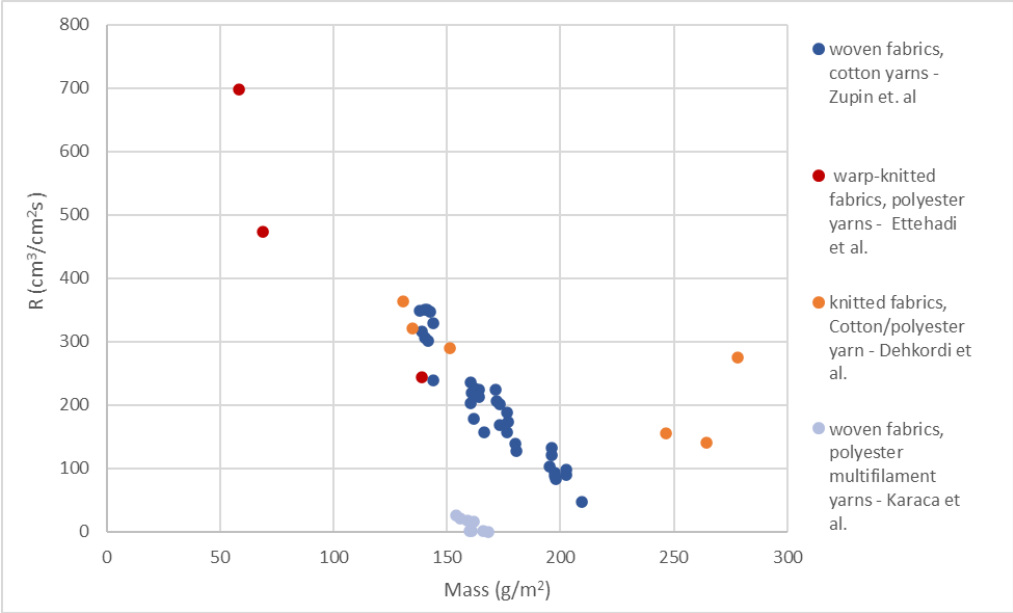


Figure 5-16: Comparison between air permeability of woven and knitted fabrics with different mass (g/m^2)

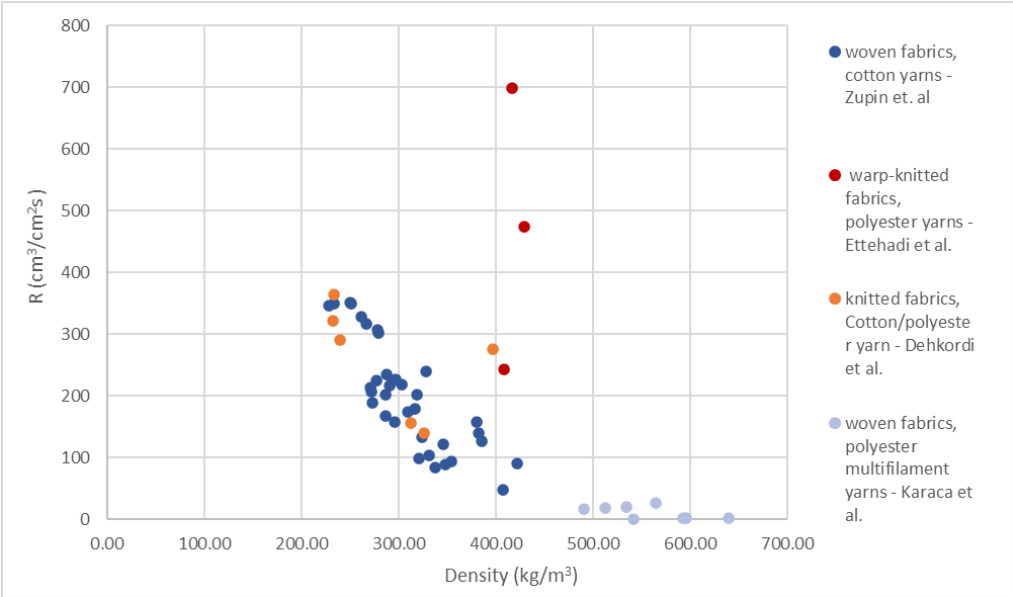


Figure 5-17: Comparison between air permeability of woven and knitted fabrics with different density (kg/m^3)

6. Through-thickness and in-plane permeability: CFD simulations

Permeability values are important in a wide range of applications dealing with air or fluid flows through textile structures, such as outdoor clothing or textile preforms for composite production [2]. For this reason, the interest in the calculations of textile permeability is recently increasing. Some authors in fact used CFD to study the flow through the fabric, modelling the three-dimensional woven fabric geometry as a unit cell to calculate through-thickness and in-plane flow.

In this chapter CFD simulations of the air flow through a plain-woven fabric are presented. The goal of these simulations is to calculate through-thickness and in-plane permeability, values that will be used as input parameters for the simulation of the scCO₂ dyeing process described in Chapter 7.

6.1. Literature review

During last years, more and more researchers have started using CFD for the modelling of fabric air permeability. In fact, studies on CFD simulations and modelling of single layer or two-layered woven fabrics are both presented in literature, with acceptable experimental results agreement. Other studies also deal with the use of CFD to model and simulate the air flow through knitted fabrics. To make some examples, Dehkordi et al. [60] used CFD to simulate air permeability of knitted fabrics with rib and interlock structures. They created a unit cell of each sample using CATIA software. CFD analysis were executed by the authors using the software ANSYS Fluent concluding that their CFD model was an efficient tool in predicting air permeability of knitted fabrics, as numerical results showed good agreement with the experimental data. They simulated the unit cell of fabric immersed in a pipe-like domain (long enough to assure the total flow formation after the sample). In addition, simulating the flow through a single unit cell of fabric, the authors were able to reduce time resolution because of the small dimensions of the model. They used two different turbulent models: $k-\varepsilon$ and $k-\omega$, concluding that the $k-\varepsilon$ model shows smaller errors. The authors set a pressure difference of 100 Pa between two the faces of the fabric.

Ettehadi et al. [67] also investigated air permeability of warp-knitted fabrics using experimental and numerical simulation. The 3D geometry of warp-knitted fabrics was modeled using CATIA, as well. Error of less than 16 % were found by the authors between experimental and numerical results, concluding that they were compatible. CFD analysis was performed by the authors on a repeated unit-cell using ANSYS Fluent software. They also assumed a pipe-like domain with a square cross-section long enough to assure total flow formation after the sample. Tetrahedral elements were used in this study in order to discretize the computational domain. For the boundary conditions, the authors imposed periodic boundary condition on surfaces along x and y-directions and a no-slip boundary condition at the solid/fluid interfaces.

Pezzin [65] modelled fabrics in order to predict their comfort properties. He also investigated the air permeability of different fabrics using CFD modelling. In order to analyse the influence of different fabric structures, different 3D models were realized by the author. Air

permeability was evaluated using COMSOL Multiphysics, where 3D models created with TexGen (a open-source software package for 3D modelling of textiles) were imported. A control volume that contains the base unit of every weave pattern was modelled, constant pressure has been defined as inlet condition and at the side wall a symmetry boundary condition has been used in order to consider an infinite textile fabric; the author reported very good agreement with experimental data.

6.2. Through-thickness and in-plane permeability simulations of a plain woven fabric

In this work, CFD is used to calculate the permeability tensor of a woven fabric. The simulations were set on the basis of air permeability analysis previously conducted in literature using CFD. A plain-woven fabric, with a known experimental air permeability, was built in TexGen and then imported in ANSYS Fluent. A rectangular cross section channel was constructed on the basis of similar studies in literature. The model was validated by setting simulations reproducing the experimental air permeability (R) tests conducted by Zupin [51] on the same fabric structure, which imposed a ΔP of 200 Pa during the test. In fact, the air permeability simulations are usually conducted imposing a ΔP equal to 100 or 200 Pa (depending on the type of fabric, where 100 Pa is set for garments and 200 Pa is set for technical fabrics). The characteristics of the chosen fabric sample are reported in **Table 6-1**. In the present work, once the geometrical model was validated, ΔP much lower than 100 Pa was set in the simulations in order to fall within the range of validity of Darcy law, where ΔP is proportional to the air speed. Thus, the permeability parameter (in m^2) was found for the analysed fabric using Darcy law.

Table 6-1: Characteristics of the chosen fabric sample (plain woven)

Sample	PL22/15
thickness (mm)	0.4390
R (exp.) $cm^3/cm^2 s$	239.2
fabric porosity (%)	78.45
Mass (g/m^2)	143.9

6.2.1. Through-thickness permeability simulations: setup

The fabric geometry was built using TexGen, the open-source software package for 3D modelling of textiles and their composites developed by the Polymer Composites Group at the University of Nottingham [61]. This software is also used to generate models to predict fabric and reinforcement permeability. In fact, it has been used to predict in-plane and through-thickness permeability as input data for macro-scale models of resin infusion during

composites manufacture or water/air permeability for clothes. The software TexGen is written in standard C++ and it is possible to drive its Graphical Unit Interface using script written in Python to create different textile structures. In order to simulate a fabric whose value of air permeability is already known, the script written by Pezzin [65] has been adapted to the present work (reported in Appendix II). A plain weave with 22 ends/cm for warp yarns and 15 ends/cm for weft yarns was built using TexGen and then imported into the simulation software. The unit base of every weave patterns of the plain-woven fabric, generated with TexGen, is presented in **Figure 6-1**. Although the textile fabric has been considered as infinite, in order to reduce the computational time only a control volume containing the base unit of the fabric has been modelled, following the examples in the literature previous described.

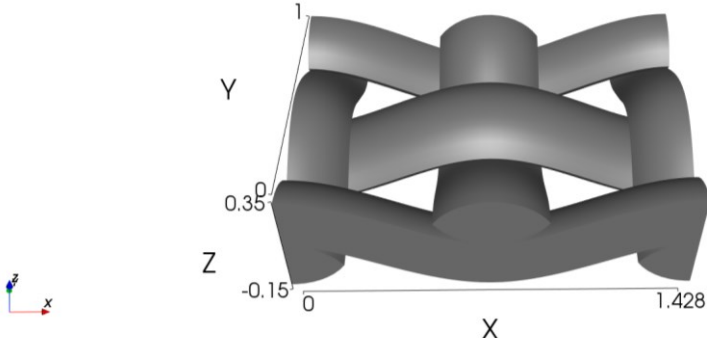


Figure 6-1: Base unit of plain woven fabric generated with TexGen

In the CFD simulation, a rectangular cross section channel with a total length of 10 mm was constructed on the basis of similar examples in the literature concerning air permeability testing of textiles. **Figure 6-2** shows the geometry for the through-thickness permeability simulations of the woven fabric in ANSYS Fluent.

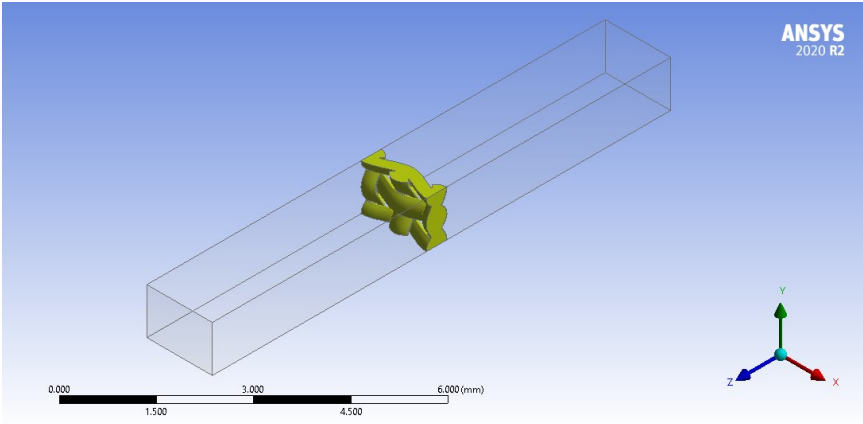


Figure 6-2: Geometry for the through-thickness permeability simulations of the woven fabric in ANSYS Fluent

The mesh was created using tetrahedral elements for both free and porous domain, considering an element size of 1×10^{-4} m, for a total of 591095 nodes and 2677686 elements. The growth rate was reduced to 1.1 and curvature min size set as 1×10^{-5} m with a curvature normal angle equal to 2° . Inflation layers in correspondence of contact region between fabrics yarns and the free channel domain were set, with a first layer thickness of 1×10^{-5} m. **Figure 6-3** to **Figure 6-5** report a graphical representation of the mesh used in ANSYS Fluent for the entire domain, with a magnification on fabric domain.

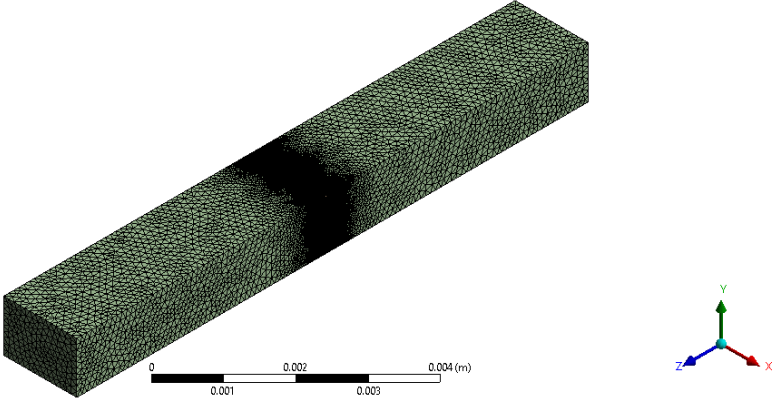


Figure 6-3: Mesh for the through-thickness permeability simulations of the woven fabric in ANSYS Fluent - Entire domain

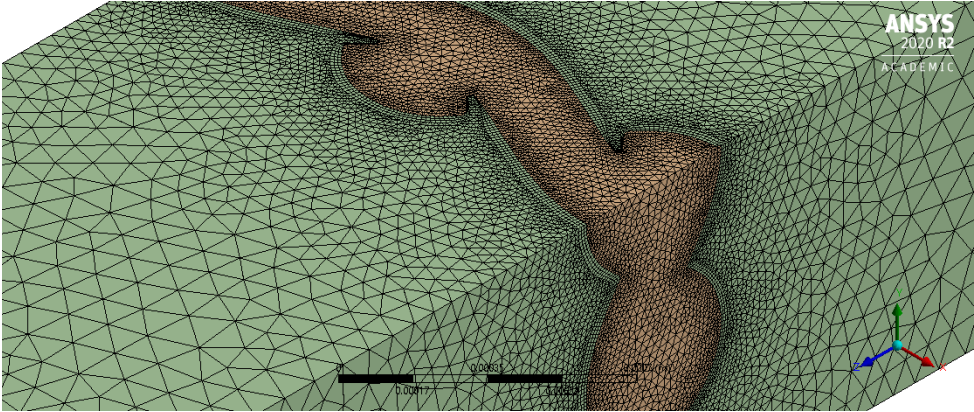


Figure 6-4: Mesh for the through-thickness permeability simulations of the woven fabric in ANSYS Fluent – Entire domain (magnification)

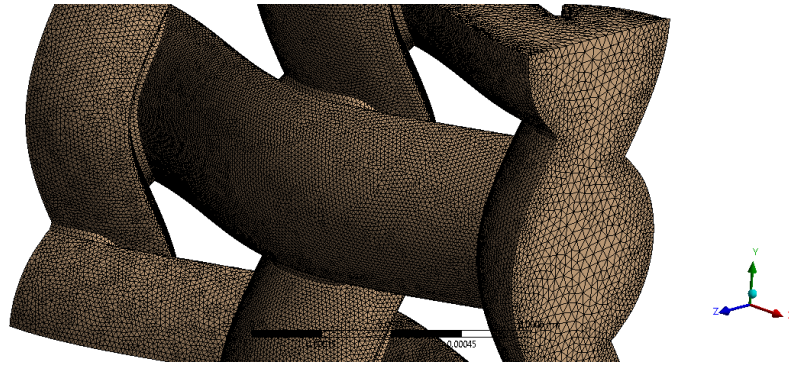


Figure 6-5: Mesh for the through-thickness permeability simulations of the woven fabric in ANSYS Fluent – Fabric domain

The steady-state simulations were conducted prescribing a laminar model when low air velocity was set. The Realizable $k-\varepsilon$ turbulence model was instead used for those simulation conducted at higher air velocities, in order to validate the results with the experimental test. A pressure-based solver with SIMPLE Pressure-Velocity Coupling and second order spatial discretization was selected. This choice was made because Steady-state calculations generally use SIMPLE or SIMPLEC, which have similar convergence rates.

The yarns constituting the fabric were specified as porous medium on ANSYS Fluent (specifying the value of yarn permeability) and boundaries conditions were defined for inlet, outlet and for the side walls of the control volume. For the side walls, symmetry boundary condition were set in order to consider an infinite textile fabric, as shown in **Figure 6-6**.

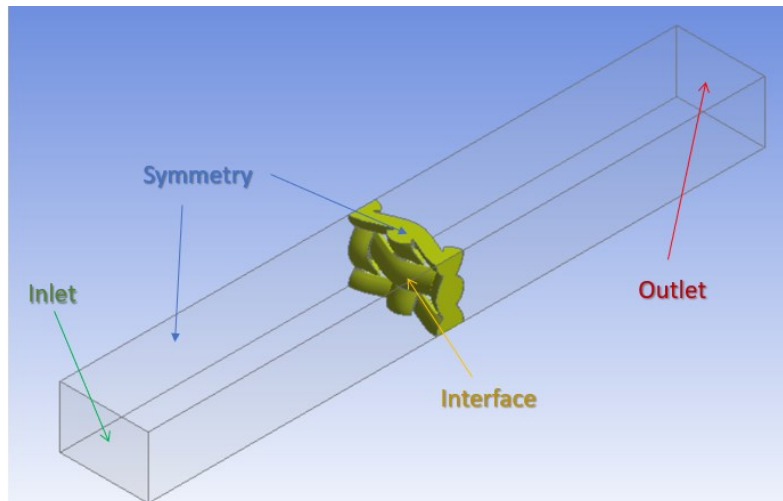


Figure 6-6: Boundary conditions - through-thickness permeability simulations of the woven fabric

6.2.2. Through-thickness permeability simulations: results

In order to capture correctly the physics of the flow, three cases were investigated: the first one prescribes a null yarn permeability, indeed the yarns were designated as walls for the system. In the second case, isotropic yarn permeability and in the third case anisotropic

permeability of yarns were specified. The last two tests have been done in order to take into account the difference between the permeability along the yarns and the permeability perpendicular to the yarns, both calculated with formulas reported by Gebart [46] and described in the previous Chapter.

It was concluded that the higher deviation from the experimental air permeability reported by Zupin [64] is obtained specifying zero permeability of yarns. This test was done because, according to studies, air flow takes place mostly in the spaces between yarns. But from this simulation it has been noticed that the small quantity of air that passes through the yarns influences considerably the result. The other two cases gave very similar deviation from the experimental air permeability test, for this reason it was concluded to continue the study assuming an isotropic permeability of the yarns. Yarn permeability has been calculated considering an hexagonal array disposition of the fibres in the yarns and the values are reported in **Table 6-2**.

Table 6-2: Cotton yarn permeability

Fibre packing	Quadratic	Hexagonal
permeability along the fibres - K_{\parallel} (m^2)	2.65×10^{-12}	2.83×10^{-12}
Permeability perpendicularly to the fibres - K_{\perp} (m^2)	1.26×10^{-11}	1.35×10^{-11}

Deviation between the CFD calculation of air permeability and the experimental one ($239.167 \text{ cm}^3/\text{cm}^2\text{s}$) is shown in **Table 6-3** for the three different set-ups previous described.

Table 6-3: Deviation of the air permeability values calculated from the simulations and the experimental data

Test	Air permeability, R ($\text{mm}^3/\text{mm}^2\text{s}$)	Deviation with the experimental data
Zero permeability of yarns	1964.89	17.84%
Isotropic permeability	2203.01	7.89%
Anisotropic permeability	2203.80	7.86%

In conclusion, for the following simulations cotton yarns are specified as porous medium with an isotropic permeability of $K=1.35 \times 10^{-11} \text{ m}^2$.

Figure 6-7 shows the path lines obtained from a simulation in which the inlet air velocity was set to 1 m/s. From this image it is clear that the preferred path for the air is through the gaps between yarns, but a small fraction also flows through the yarns. This is the main difference with respect to the simulations done specifying zero as yarn permeability: that configuration does not allow to appreciate the contribution of the air flow through the yarns, resulting in higher deviation from experimental air permeability.

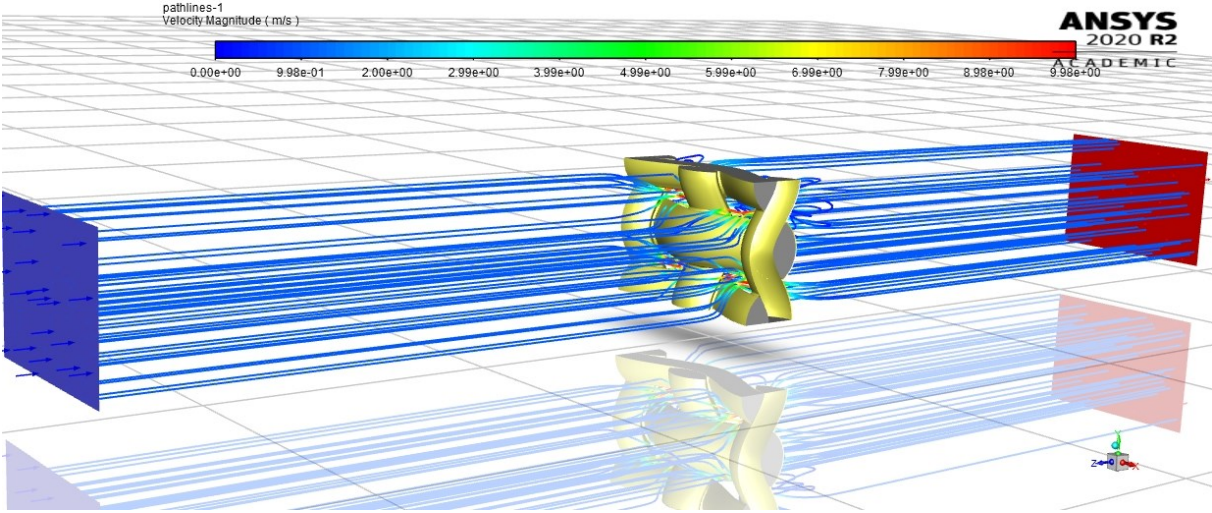


Figure 6-7: Pathlines of the air flowing through the fabric domain

In the simulations with $\Delta P = 200$ Pa the contribution of the inertial term to the fluid flow is substantial. Thus, in order to fall within the range of validity of the Darcy law and calculate the through-thickness permeability parameter K_T (in m^2), three different tests were conducted, specifying low inlet velocities. From those results, the parameter K_T was calculated using the following formula (Darcy law):

$$\Delta P = \frac{\mu L Q}{K_T A}, \tag{6-1}$$

where ΔP is the pressure difference through the fabric thickness (L), A is the fabric area simulated and Q is the air flow rate passing through the fabric. The obtained values are reported in **Table 6-4** whereas the values of ΔP versus velocity obtained from the simulations are shown in **Figure 6-8**. It can be observed a direct proportionality, which confirms the use Darcy law for the calculation of K_T .

Table 6-4: Results of the first set of simulations – through-thickness permeability

Inlet velocity (m/s)	ΔP (Pa)	K_T (m^2)
0.01	0.210	4.21×10^{-10}
0.05	1.08	4.15×10^{-10}

0.025	0.536	4.19×10^{-10}
-------	-------	------------------------

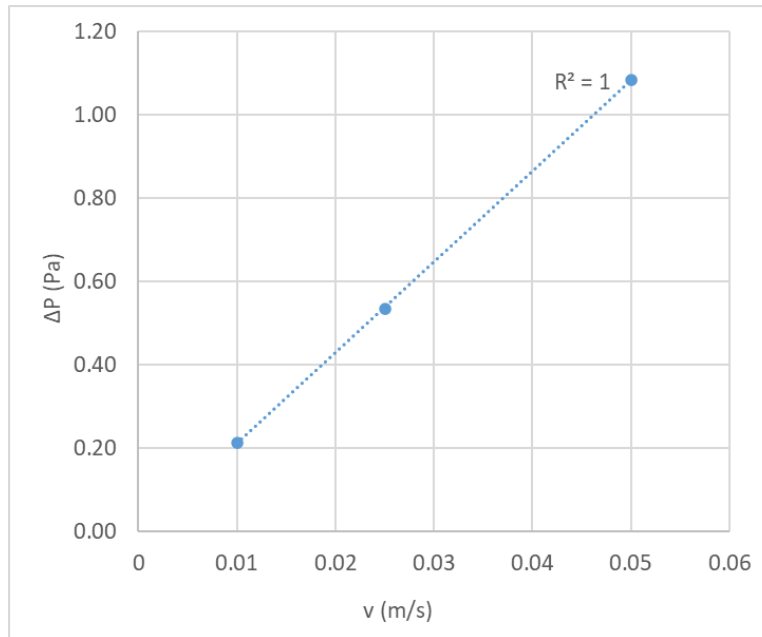


Figure 6-8: Plot of pressure drop versus air velocity – first set of simulations, through-thickness permeability

A further test, setting scCO₂ (instead of air) as fluid and the operating conditions of the DyeCoo dyeing process, was carried out. Also in this case, the calculated through-thickness permeability is consistent with the previous calculations, as shown in **Table 6-5**. This was considered as a further confirmation of the model.

Table 6-5: Results considering scCO₂ as fluid - through-thickness permeability

Fluid	Inlet velocity (m/s)	ΔP (Pa)	K_T (m ²)
scCO ₂	0.0265	0.57	4.19×10^{-10}

It is worth to say that a linear relationship between pressure drop and flow velocity can be assumed in a porous medium only under low pressure drop. By increasing the pressure drop, Reynolds number increases too, although the flow regime is still laminar. In this condition, a non-linear relationship between pressure drop and flow velocity applies. This means that Darcy's law cannot be used for accurate flow analysis and in this case an inertial term must be introduced. The equation used for describing the behaviour of the porous medium on ANSYS Fluent under these conditions is here reported:

$$\Delta P = \frac{\mu L}{K_T} v + \frac{LC_2\rho}{2} v^2. \quad (6-2)$$

Hence a second set of simulations are conducted on the fabric in order to calculate the inertial coefficient (C_2) required by the software ANSYS Fluent, in the case of higher air velocity.

Table 6-6 shows the value obtained from those simulations, where the value C_2 has been calculated from the Equation (6-2) specifying an average value of K_T obtained from the first set of simulations (in which a low inlet velocity was imposed). In this way, the equations describing the relationship between the pressure drop and the flow velocity has been calculated ($\Delta P=35.19v^2+21.51v$) and reported graphically in **Figure 6-9**.

The final results of the simulations are summarized in **Table 6-7**.

In order to fully validate the results, the experimental value of air permeability for this type of fabric was substituted in Equation (6-2), specifying the K_T value found from the first set of simulations under small pressure drops and low velocities. The C_2 value resulted from this calculation showed a deviation of 12% from the value reported in **Table 6-7** and calculated from the second set of simulations. This deviation was considered acceptable.

Table 6-6: Results of the second set of simulations – through-thickness permeability

Inlet velocity (m/s)	ΔP (Pa)	K_T (m ²)	C_{2T} (1/m)
1	5.90×10^1	4.18×10^{-10}	1.22×10^5
2	1.84×10^2	4.18×10^{-10}	1.15×10^5
3	3.59×10^2	4.18×10^{-10}	1.07×10^5

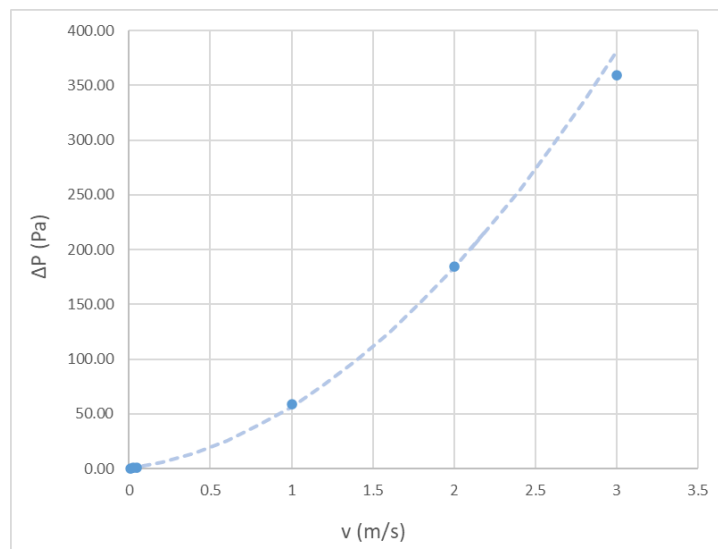


Figure 6-9: Plot of pressure drop versus air velocity – second set of simulations, through-thickness permeability

Table 6-7: Results of the simulations - through-thickness permeability

$K_T(\text{m}^2)$	4.18×10^{-10}
$1/K_T(1/\text{m}^2)$	2.39×10^9
$C_2(1/\text{m})$	1.15×10^5

6.2.3. In-plane permeability simulations: setup

The simulations for the in-plane permeability calculation were set similarly to those for through-thickness permeability, previously described. A rectangular cross section channel of length 10 mm was built in ANSYS Fluent, having similar dimensions to the previous simulation geometry, with the difference that the fabric was placed obliquely inside the channel in order to calculate the contribution of the in-plane component of the permeability tensor. The geometry for these types of simulations of the woven fabric in ANSYS Fluent is represented in **Figure 6-10**.

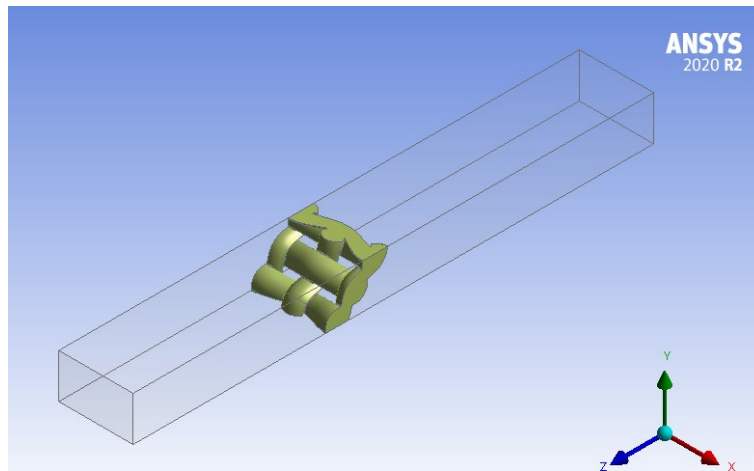


Figure 6-10: Geometry for the in-plane permeability simulations of the woven fabric in ANSYS Fluent

The mesh was created using tetrahedral elements for both free and porous domain, considering an element size of 0.0001 m, for a total of 670118 nodes and 3044646 elements. The growth rate was reduced to 1.1 and curvature min size was set to 1.00×10^{-5} m with a curvature normal angle equal to 2° . Inflation layers in correspondence of contact region between yarns and the free channel domain were set, with a first layer thickness of 1×10^{-5} m. In **Figure 6-11** and **Figure 6-12** a graphical representation of the mesh used in ANSYS Fluent, for the entire domain with a magnification on the fabric domain, is reported.

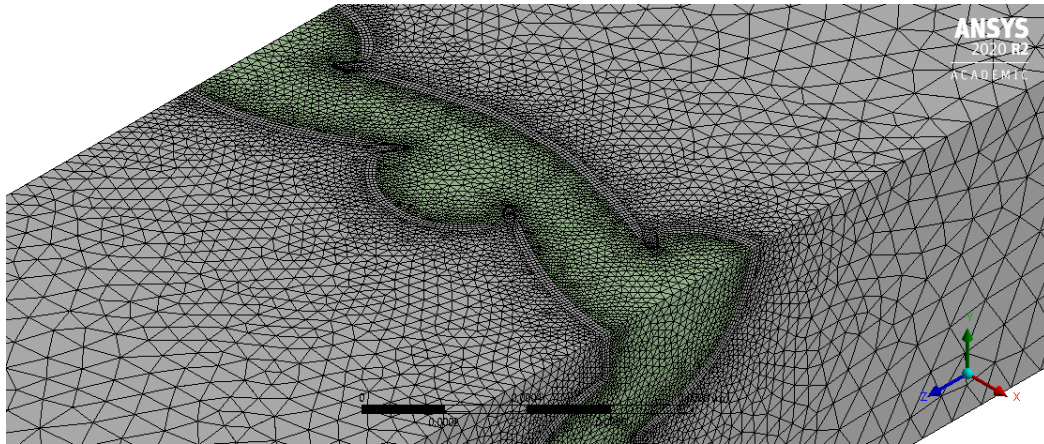


Figure 6-11 Mesh for the in-plane permeability simulations of the woven fabric in ANSYS Fluent (magnification)

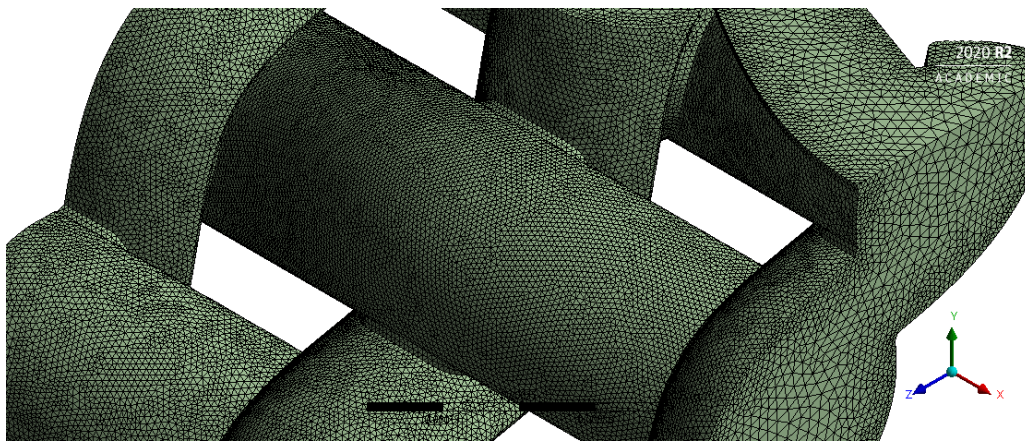


Figure 6-12: Mesh for the in-plane permeability simulations of the woven fabric in ANSYS Fluent – fabric domain

The steady-state simulations were conducted specifying a laminar model for the simulations under low pressure drops and low air velocity, while the $k-\varepsilon$ turbulence model was used for those simulation which considers higher air velocities, as in the previous case. A pressure-based solver, SIMPLE Pressure-Velocity Coupling and second order spatial discretization have been selected.

The cotton yarns constituting the fabric were specified as porous medium on ANSYS Fluent with permeability of $1.35 \times 10^{-11} \text{ m}^2$ and the selected fluid was air. Boundary conditions were defined for inlet, outlet and for the side walls of the control volume. Regarding the side walls of the channel, in this case they are not defined as symmetry but are instead specified as walls with zero shear stress.

6.2.4. In-plane permeability simulations: results

The two in-plane permeabilities were considered similar and approximated to K_P due to the particular structure of the fabric (plain woven). In order to fall within the range of validity of Darcy law and calculate the in-plane permeability parameter K_P (in m^2), low inlet velocities were set for an initial set of simulations, as in the previous case. From those simulations, it was possible to calculate the permeability parameter K' , from which the in-plane permeability K_P (in m^2) was calculated. The value of K' was calculated from Darcy law:

$$\Delta P = \frac{\mu L Q}{K' A}. \quad (6-3)$$

Then the value of K_P was calculated with the following relationship:

$$K' = K_T + K_P \quad (6-4)$$

The values of K_P are reported in **Table 6-8** whereas the values of ΔP versus velocity are reported in **Figure 6-13**. It is clear that there is a direct proportionality, and this allows the use Darcy law for the calculation of K_P . The chosen value of K_P is $8.85 \times 10^{-10} \text{ m}^2$, which is the mean value resulted from the simulations. This value is higher with respect to K_T , as expected. In fact, this result agrees with literature studies.

Table 6-8: Results from the first set of simulations – in-plane permeability

Inlet velocity (m/s)	ΔP (Pa)	K'	K_P (m^2)
0.01	0.19	1.31×10^{-9}	8.90×10^{-10}
0.05	0.938	1.30×10^{-9}	8.77×10^{-10}
0.025	0.47	1.31×10^{-9}	8.87×10^{-10}

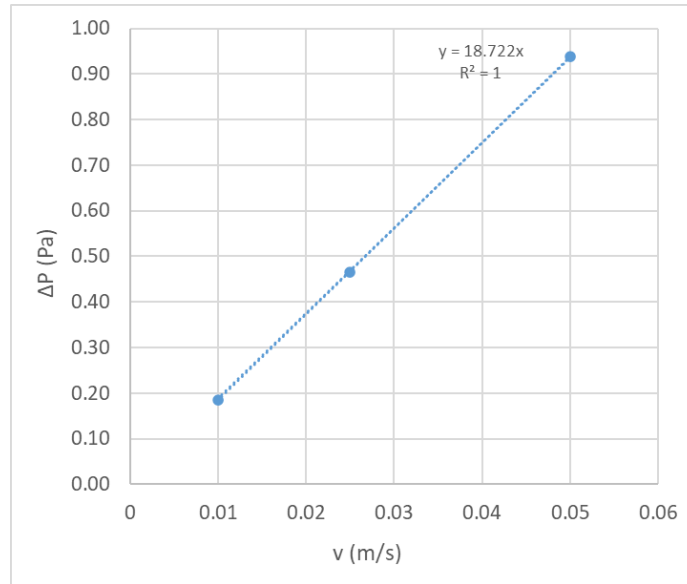


Figure 6-13: Plot of pressure drop versus air velocity – first set of simulations, in-plane permeability

Also in this case a second set of simulations was performed specifying higher velocities of the air at the inlet in order to calculate the inertial coefficient (C_2'). As for the calculation of through-thickness permeability, the equation modelling the behaviour of the porous medium on ANSYS Fluent is here reported:

$$\Delta P = \frac{\mu L}{K'} v + \frac{LC_2' \rho}{2} v^2. \quad (6-5)$$

From this Equation (6-5) the value C_2' has been calculated using the average value of K' obtained from the previous simulations.

Table 6-9 shows the values obtained from this second set of simulations, once calculated the value of C_2' from the Equation (6-5). In this way the equations describing the relationship between the pressure drop and the flow velocity has been calculated ($\Delta P = 24.837v^2 + 18.650v$) and represented in **Figure 6-14**.

The final results of the simulation are summarized in **Table 6-10**.

Table 6-9: Results from the second set of simulations – in-plane permeability

Inlet velocity (m/s)	ΔP (Pa)	K' (m ²)	C_2' (1/m)
1	43.601	1.3×10^{-9}	30175.876
2	137.933	1.3×10^{-9}	30425.815
3	275.561	1.3×10^{-9}	29510.213

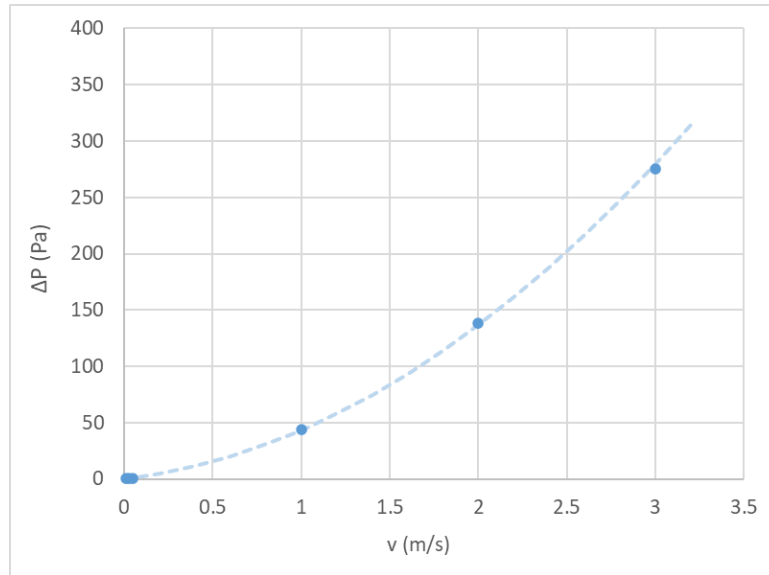


Figure 6-14: Plot of pressure drop versus air velocity – second set of simulations, in-plane permeability

Table 6-10: Results of the simulations – in-plane permeability

K_P (m^2)	8.85×10^{-10}
$1/K_P$ ($1/m^2$)	1.13×10^9
C_2' ($1/m$)	3.00×10^4

7. System under investigation: scCO₂ dyeing apparatus

The dyeing vessel of the DyeCoo equipment was modelled with the software ANSYS Fluent. The industrial scale dyeing machine of the DyeCoo company (called DyeOx) consists of three dyeing vessels where the fabric is wrapped on a beam. The dyestuff is placed in a separate cartridge connected to the beam before the introduction of scCO₂ into the vessel for the dyeing process. More details about this process can be found in paragraph 4.3.

Here a single dyeing vessel was modelled in order to investigate the flow distribution of the scCO₂ inside the fabric. In the next paragraphs the geometry, method and setup of the simulations are described.

7.1. Modelling supercritical fluid

In this work, to evaluate thermodynamic and transport properties of supercritical carbon dioxide, the NIST real gas models on Fluent has been selected. The latter uses the National Institute of Standards and Technology (NIST) model which incorporates the equation of state for carbon dioxide of Span and Wagner. Once the appropriate NIST real gas model is enabled on Ansys Fluent, the software loads data for the chosen material from a library of pure fluids supported by the REFPROP database, and reports that it is opening the shared library (librealgas.so) where the compiled REFPROP database source code is located [6]. If carbon dioxide is selected, these are the properties used by the software:

Matl name: "carbon dioxii"

: "carbon dioxide lfull name"

: "124-38-9"

Mol Wt : 44.0098

Critical properties:

Temperature : 304.128 (K)

Pressure : 7.3773e+06 (Pa)

Density : 10.6249 (mol/L) 467.6 (kg/m³)

Equation Of State (EOS) used:

Helmholtz Free Energy (FEQ)

EOS:"FEQ Helmholtz equation of state for carbon dioxide of Span and Wagner (1996)."

EOS Range of applicability

Min Temperature: 216.592 (K)

Max Temperature: 2000 (K)

Max Density : 1638.92 (kg/m³)

Max Pressure : 8e+08 (Pa)

Thermal conductivity Range of applicability

Min Temperature: 216.58 (K)
Max Temperature: 2000 (K)
Max Density : 1638.92 (kg/m³)
Max Pressure : 8e+08 (Pa)

Viscosity Range of applicability
Min Temperature: 216.592 (K)
Max Temperature: 2000 (K)
Max Density : 1638.92 (kg/m³)
Max Pressure : 8e+08 (Pa)

The Span and Wagner equation of state for carbon dioxide is a Maxwell–Helmholtz fundamental equation of state and is the most accurate relationship for carbon dioxide in the literature.

When dealing with supercritical fluids, an accurate prediction of the turbulence at supercritical conditions with low computational cost is crucial [68]. In fact, turbulence plays a very important role in the behaviour of chemical engineering equipment since the dramatic change of fluid properties near and above the critical point leads to a change in the fluid-dynamic behaviour. Hence, “the choice of the appropriate turbulence closure for each problem is a crucial unresolved task” [68]. For this scope Sierra-Pallares et al. [68] did an assessment of turbulence models to discern which is the most suitable choice when dealing with supercritical fluids. Their results show that the *Realizable k-ε* model was the most accurate choice for the simulation of high-pressure systems.

On the basis of the literature studies, in this work the *Realizable k-ε* was chosen as turbulence model to deal with SCFs.

7.2. Geometry and mesh

A two-dimensional axisymmetric domain was considered in order to model the dyeing vessel of DyeCoo system.

The company uses beams of different dimensions for this process and the choice depends on the type of fabric which have to be processed. Diameter of 200 mm for the beam is usually used for knitted fabrics, while beam diameter of 200 mm, 400 mm, and 600 mm are generally used for woven [29] [30]. In the present work, the 200 mm beam diameter, which is suitable for both knitted and woven fabrics, was chosen. The maximum dyeable fabric width is 2000 mm for this equipment, but here only 1520 mm (60") has been considered since it is a typical fabric dimension and working condition. The inner vessel diameter was set to 900 mm resulting in a total length of 1820 mm.

Usually, the fabric weight on the beam is 80-140 kg. Here, choosing the condition of load of 80 kg, the approximate height of the fabric wrapped on the beam was calculated. Knowing the weight of the fabric on the beam and taking under consideration an average density value typical of these materials, the total volume of the fabric to be processed was calculated. Then,

by knowing the beam surface on which the fabric will be wrapped, the height of the porous medium on the beam was calculated. This value represents a first approximation value for the height of the porous medium. The details of the calculation are reported in **Table 7-1**.

Table 7-1: Radial thickness of the fabric wounded on the beam

Density (g/m ²)	123
Fabric thickness (mm)	0.500
Fabric weight on beam (kg)	80.0
External radius of fabric material (m)	0.280
Chosen value of external fabric radius (m)	0.300
Chosen value of radial thickness (m)	0.200

Two different geometries were considered in this work: the first one considered the beam lateral surface as interface with the fabric, while the second one takes into account the perforated beam structure, which is made of interface zones alternating with walls. The pore dimensions (5 mm) and the interval distance between the holes (5 mm) of the perforated beam were modelled on the basis of a similar study in literature and [1]. In order to reduce the computational cost, a two-dimensional axisymmetric geometry was considered.

The simplified beam configuration is shown in **Figure 7-1**, while the perforated beam configuration is built considering alternating openings of 5 mm (set as interfaces) and walls of 5 mm for all the beam length, as shown in **Figure 7-2**.



Figure 7-1: Two-dimensional axisymmetric domain on ANSYS Fluent

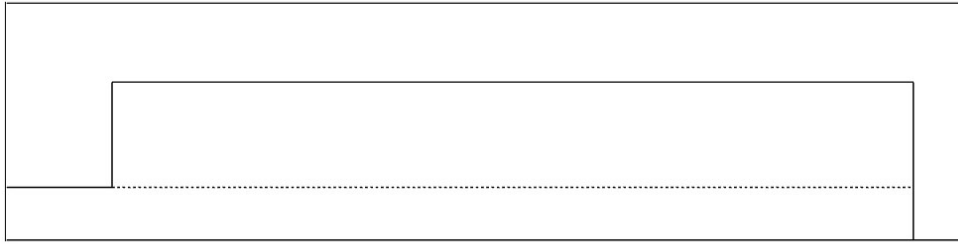


Figure 7-2: Two-dimensional axisymmetric domain for the perforated beam construction

The computational domain for the configuration with the simplified beam is shown in **Figure 7-3**, while a magnification of the beam and the interface with the porous medium is represented in **Figure 7-2**. The details of the mesh are reported in **Table 7-2**

Table 7-2: Mesh details, simplified beam

Element size (m)	5.00×10^{-3}
Nodes	35828
Elements	34611

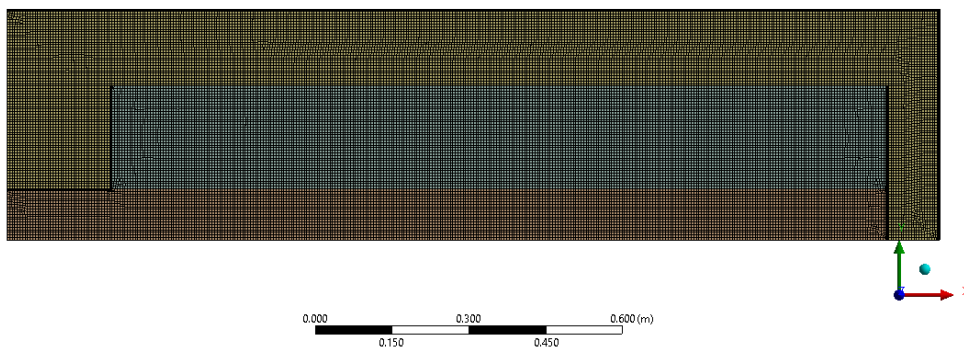


Figure 7-3: Computational domain for the simplified beam geometry in ANSYS Fluent

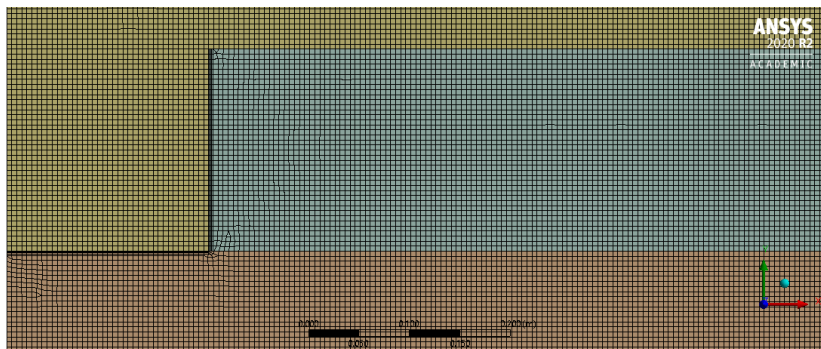


Figure 7-4: Computational domain for the simplified beam geometry in ANSYS Fluent (magnification)

The details of the computational domain for the perforated beam configuration are reported in **Table 7-3**. While a magnification of the beam and the interface with the porous medium is represented for the perforated beam configuration in **Figure 7-5**. In particular, a refinement was done in correspondence of the perforated structure of the beam.

Table 7-3: Mesh details, perforated beam

Element size (m)	5.00×10^{-3}
Nodes	70354
Elements	68150

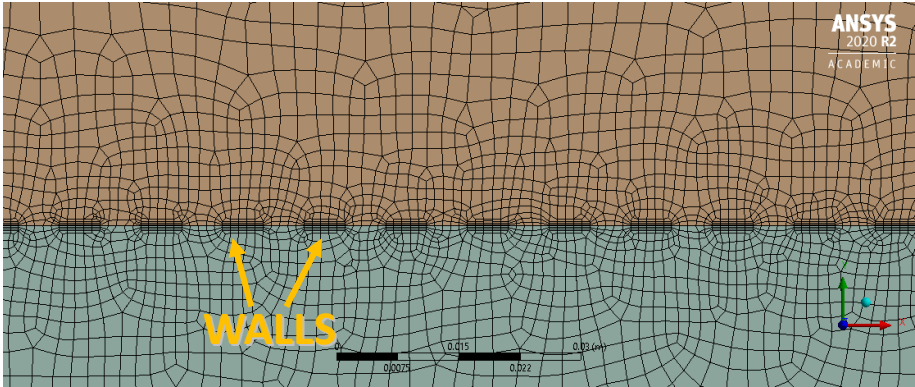


Figure 7-5: Computational domain for the perforated beam geometry, perforated beam interface with the porous medium

In both cases cell inflation at the walls have been set. Regarding the wall treatment, wall functions were used to bridge the viscosity-affected region between the wall and the fully turbulent region in ANSYS Fluent [7] [6]. The near-wall modelling is the main responsible for the quality of numerical solutions and also the walls are the main source of mean vorticity and turbulence. Hence, successful predictions of wall-bounded turbulent flows is mainly related to the representation of the flow in the near-wall region, which must be accurate.

Experiments have shown that the near-wall region can be largely subdivided into three layers: The innermost layer, called viscous sublayer, the outer layer, called fully turbulent layer, and the interim region between the viscous sublayer and the fully turbulent layer. In the viscous sublayer the flow is almost laminar, and the viscosity plays the major role, while in fully-turbulent layer what dominates is turbulence. A graphical subdivision of the near-wall region is shown in **Figure 7-6**.

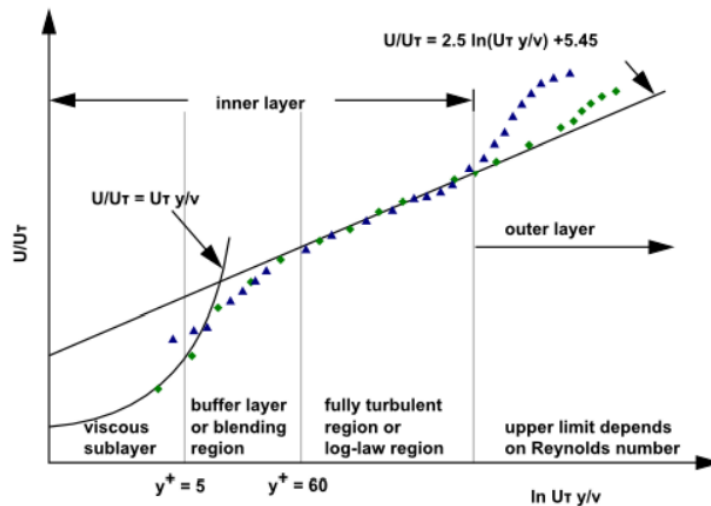


Figure 7-6: Subdivisions of the near-wall region [7]

Two approaches are traditionally used in modelling the near-wall region and one of these refers to the use of the wall functions. With this approach, the viscosity affected inner region is not resolved and wall functions are used to bridge the viscosity-affected region between the wall and the fully turbulent region. Wall functions are a set of semi-empirical formulas and their usage obviates the need to modify the turbulence models to account for the presence of the wall. In the second approach, the turbulence models are modified to enable the viscosity-affected region to be resolved with a mesh all the way to the wall, including the viscous sublayer. In this thesis work, Enhanced Wall Functions are used as wall treatment, since a Realizable $k-\varepsilon$ turbulence model is selected. Enhanced Wall Treatment combines a two-layer model to have a near-wall formulation that can be used with coarse meshes and fine meshes (low-Reynolds number meshes). For this reason, excessive error should not be incurred for meshes where the first near-wall node is placed neither in the fully turbulent region nor in the direct vicinity of the wall [6] [7].

7.3. Setup of the simulations

For the steady-state simulations a density-based solver and Realizable $k-\epsilon$ model was chosen on the basis of the literature studies previously reported dealing with SCFs modelling.

The density-based solver in ANSYS Fluent solves the governing equations of continuity, momentum, energy and species transport simultaneously [7]. In ANSYS Fluent, coupled-explicit formulation and coupled-implicit formulation are the two algorithms available for solving the coupled set of equations. In this work an implicit formulation and second order spatial discretization has been chosen as solution method. If this solution method is selected, each equation in the coupled set of governing equations is linearized implicitly with respect to all dependent variables in the set. This results in a system of linear equations with N equations for each cell in the domain, where N is the number of coupled equations in the set. The unknown value for a given variable in each cell is computed using a relation that includes both existing and unknown values from neighbouring cells. The difference with the explicit formulation is that this approach solves for all variables (pressure, velocities and temperature) in all cells at the same time.

The material is specified as real gas CO₂ (NIST Real gas model), as previous described, since dye carrier fluid is the major component in scCO₂ dyeing. In fact, in beam dyeing the prime levelness consideration is from the flow distribution of dye at various axial locations of the beam [1]. In the present work, a focus on the flow distribution was made, since the colour levelness is influenced by the evenness in flow distribution.

The operating condition of the simulations are reported in **Table 7-4**. A typical flow rate condition is 500 m³/h, but also 1000 m³/h can be used. In these simulations the condition of 500 m³/h was chosen. In next paragraphs a comparison with the condition of 1000 m³/h was made.

Table 7-4: Operating conditions

Temperature	120 °C
Pressure	250 bar
scCO₂ flow rate	500 m ³ /h
ρ_{CO_2} (120°C, 250 bar)	505.56 kg/m ³

For a first set of simulations, the fabric region was modelled as a porous medium with a viscous resistance ($1/K$) of 6.086×10^{10} 1/m² (as specified in the literature [1]) and an inertial resistance (C_2) equal to zero.

Mass flow inlet and pressure outlet (250 bar) were specified as boundary condition. Stationary wall, no slip and standard roughness model with a temperature of 393.15 K were specified at the vessel walls. Computational domain and boundary conditions are shown in **Figure 7-7**.

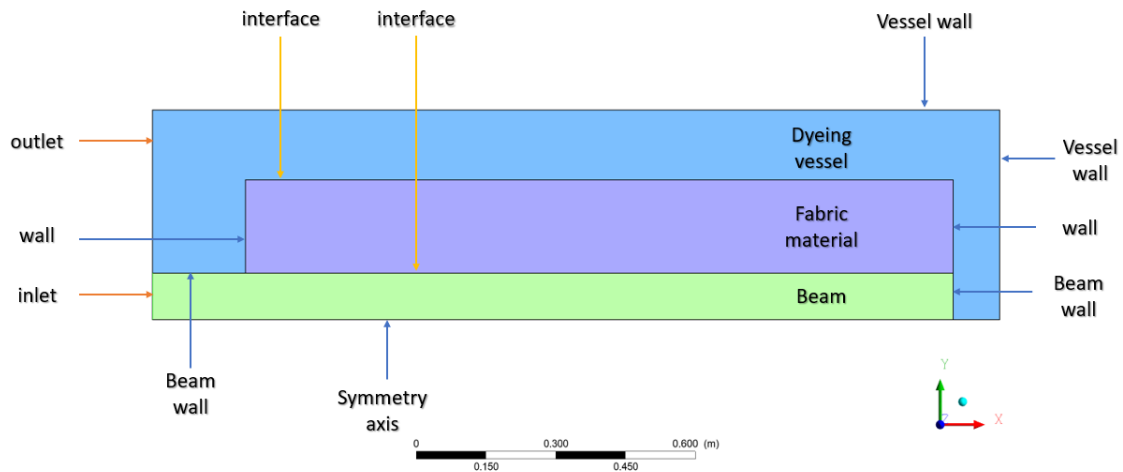


Figure 7-7 Computational domain and boundary conditions

7.4. Results and discussion

In this section the results of the simulations of the dyeing system are shown and discussed. Grid independence tests are illustrated for both the configurations (perforated and simplified beam). Then flow rate sensitivity and tests with different fabric permeability values are presented.

7.4.1. Grid independence study for the simplified beam configuration

Among the crucial factors of the CFD simulations there is the grid generation. Since the solution of the simulation could be affected by the choice of the grid, it is important to perform a grid independence study. The study is performed both on the simplified geometry and on the geometry with the perforated beam. In this type of study the grid is refined until certain key results do not change, making the simulation grid independent [3].

The various grids used in this work are indicated with M1, M2, M3, M4. Basically, the difference between them is the element size imposed. The first attempt was done considering an element size of 0.02 m for the whole domain, then two finer meshes (M3, M4) and a coarser one (M2) have been tested. The element sizes, nodes and elements of the four different tests are reported in **Table 7-5**.

Table 7-5: Grid independence study, simplified beam configuration

Mesh	Element size (m)	Nodes	Elements
M1	2.00×10^{-2}	2546	2241
M2	4.00×10^{-2}	812	656
M3	5.00×10^{-3}	35828	34611

M4	2.00×10^{-3}	209584	206612
-----------	-----------------------	--------	--------

To evaluate the effectiveness of the results, a comparison has been made in terms of average velocity magnitude and pressure difference within the fabric, which represent the key parameters. These are evaluated for each test, ensuring that their values do not change when a grid refinement is performed. To compare the scCO₂ average velocity magnitude inside the fabric along the axial direction, its value is calculated at the three different radial heights shown in **Figure 7-8**. The fixed radial heights correspond respectively to:

- the interface of the fabric with the beam ($y=0.1$ m),
- the middle radial height of the wounded fabric ($y=0.2$ m),
- and the upper part of the porous material, corresponding to the interface with the vessel ($y=0.3$ m).

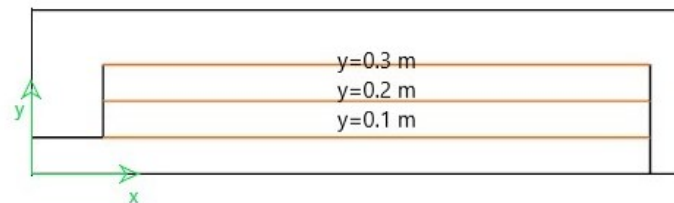


Figure 7-8: Two-dimensional axisymmetric geometry, lines at $y=0.1$ m, $y=0.2$ m and $y=0.3$ m are highlighted

The comparison in terms of average velocity magnitude and pressure difference within the porous medium is shown in **Table 7-6**, where the mesh M3 is taken as reference. It is worth observing that, between grid tests M3 and M4, the pressure difference inside the porous medium does not change and the average velocity magnitude deviation in the first contact region between the beam and the fabric is very low (1%), acceptable deviations were obtained also for the other two layers. For these reasons mesh M3 was chosen in order to have a lower computational cost, while having a lower number of cells with respect to M4.

From the comparison of the velocity field using mesh M3 and M4, the velocity distribution along the fabric was analysed graphically in **Figure 7-9** and **Figure 7-10**. The comparison shows that the velocity distribution is almost the same, confirming the choice of mesh M3 for obtaining reasonable results.

Table 7-6: Grid independence study, deviation of average velocity magnitude at fixed y -coordinate (m) and deviation of ΔP inside the porous medium - Simplified beam configuration

Mesh	M3-M1	M3-M2	M3-M4
average velocity magnitude at $y=0.1$ m	-2%	-1%	1%

average velocity magnitude at y=0.2 m	1%	1%	4%
average velocity magnitude at y=0.3 m	12%	12%	-9%
ΔP (Pascal)	23%	57%	0%

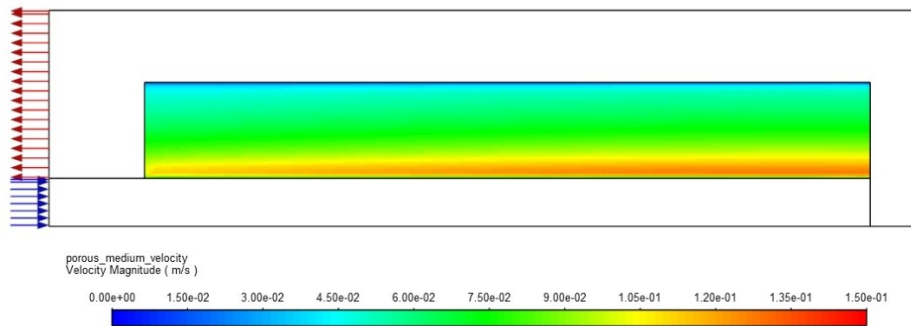


Figure 7-9: Contour of velocity magnitude inside the porous medium (m/s), mesh M3

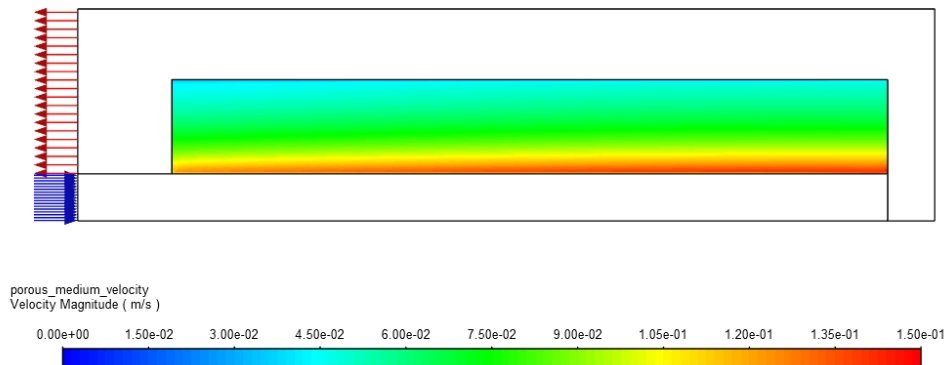


Figure 7-10: Contour of velocity magnitude inside the porous medium (m/s), mesh M4

7.4.2. Grid independence study for the perforated beam geometry

In this section the grid independence study for the perforated beam configuration is reported. The different meshes tested in this analysis are indicated with M1, M2, M3, M4 and M5 and the main difference between them is the basic element size used for grid generation. The first attempt was done considering the element size of 0.02 m, then finer meshes (M3, M4 and M5) and a coarser one (M2) have been tested. The element sizes, nodes and elements of the four different simulations are reported in **Table 7-7**.

Table 7-7: Grid independence study, perforated beam configuration

MESH	Element size (m)	Nodes	Elements
M1	2.00×10^{-2}	31909	30723
M2	4.00×10^{-2}	35138	33912
M3	5.00×10^{-3}	70354	68150
M4	1.00×10^{-2}	47377	45787
M5	2.50×10^{-3}	154606	151791

To evaluate the effectiveness of the results, also in this case a comparison in terms of average velocity magnitude and pressure difference inside the fabric was made. The velocity magnitude of the scCO₂ inside the fabric along the axial direction was monitored at three different height of the fabric material, which are the same described in the previous paragraph (7.4.1) and showed in **Figure 7-8**.

The comparison in terms of average velocity magnitude and pressure difference inside the fabric material is shown in **Table 7-8**, where M3 was chosen as the reference mesh. Since the pressure difference inside the porous medium was almost the same (only 1% of deviation) and the average velocity magnitude deviation was considered acceptable between mesh M3 and the finer mesh M5, no more refinements were necessary. The final mesh choice was made in order to have a low computational, for this reason mesh M3 was preferred to M5.

Table 7-8: Grid independence study, deviation of average velocity magnitude at fixed y-coordinate (m) and deviation of ΔP inside the porous medium – Perforated beam configuration

Mesh	M3-M1	M3-M2	M3-M4	M3-M5
average velocity magnitude at y=0.1 m	-1%	-1%	0%	0%
average velocity magnitude at y=0.2 m	2%	4%	-1%	1%
average velocity magnitude at y=0.3 m	17%	36%	8%	-10%
ΔP (Pascal)	8%	10%	3%	-1%

The numerical results in terms of average velocity magnitude and ΔP inside the porous medium are shown in **Table 7-9** and **Table 7-10**; in the next section these results are discussed in depth.

Table 7-9: Results of average velocity magnitude at fixed y-coordinate (m) inside the porous medium - Perforated beam configuration, M3

MESH	M3
Average velocity magnitude (m/s) at y=0.2 m	7.30×10^{-2}
Average velocity magnitude (m/s) at y=0.3 m	2.63×10^{-2}

Table 7-10: Results of average ΔP inside the porous medium - Perforated beam configuration, M3

MESH	M3
ΔP (Pascal)	3.85×10^4

7.4.3. Comparison between perforated beam and the simplified configuration

In this section, results obtained from the simulations with the perforated beam configuration and the simplified one are compared. This comparison is done taking into account the pressure drop and the fluid velocity in the porous medium, monitoring also the temperature and pressure of the entire system for both configurations.

For the simplified beam configuration, the pressure and temperature inside the domain were almost constant, as shown in **Figure 7-11** and **Figure 7-12**. The variation of temperature in the system is around 1 K, while the pressure drop in the fabric is about 1 bar, in front of values of absolute pressure of about 250 bar. In **Figure 7-13** the pressure field within the porous medium is represented in more detail. It is possible to notice that the highest value of pressure was obtained at the beam interface, then it decreases with the height of the fabric up to the interface with the internal vessel, where the speed of the dye carrier fluid inside the fabric was the lowest. This is an expected result and is considered plausible.

Figure 7-14 shows the path of scCO_2 from the entrance of the beam to the exit of the vessel. Here the difference in the fluid velocity between the beam and the porous medium can be seen, since different colours represent different values in velocity magnitude. It is clear how the first layers of the fabrics are submitted to the highest fluid velocity, which immediately decreases once the fluid diffuses into the porous medium. Out of the fabric, the scCO_2 speed increases in correspondence to the outlet of the vessel.

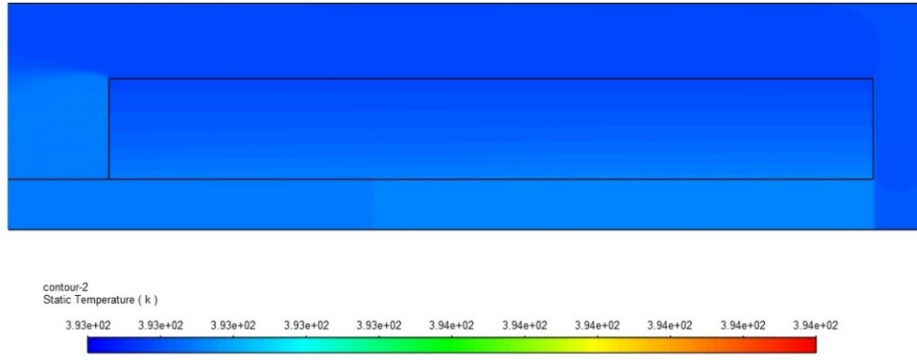


Figure 7-11: Contour of static temperature - simplified beam configuration

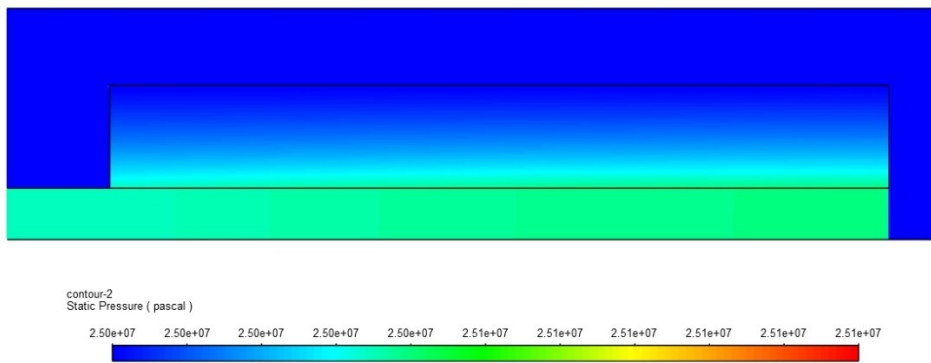


Figure 7-12: Contour of static pressure - simplified beam configuration

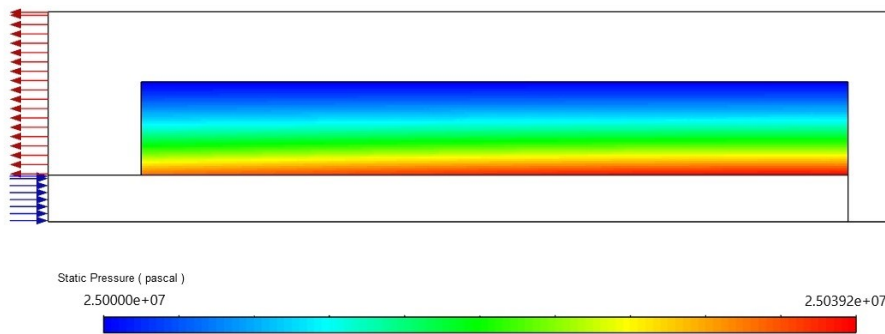


Figure 7-13: Contour of static pressure inside the porous medium - simplified beam configuration

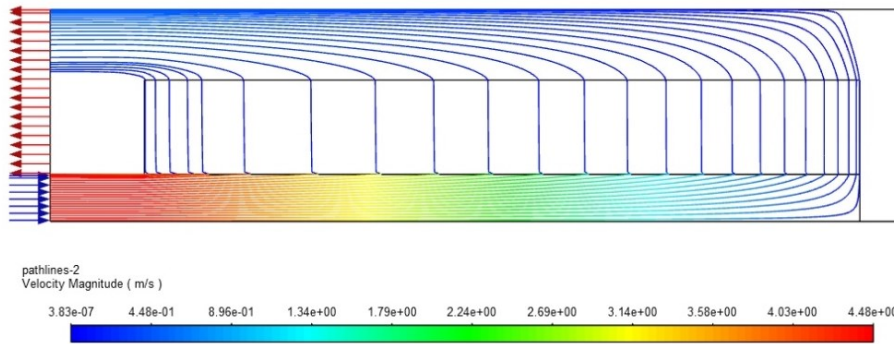


Figure 7-14: Pathlines coloured by velocity magnitude - simplified beam configuration

Turning to the results obtained from the simulations with the perforated beam configuration, the fields of pressure and temperature inside the reactor are shown in **Figure 7-15** and **Figure 7-16**. They are very similar to the previous case, concluding that also in this case pressure and temperature are almost constant inside the reactor. From this first analysis it is possible to conclude that the beam configuration does not influence the process parameters in terms of pressure and temperature, showing that the simplified configuration of the beam is good enough for describing the system. In fact, is clear from **Figure 7-17** that the pressure distribution inside the fabric is very similar between the two configurations, considering the same pressure range. In fact, also in this case the pressure is higher in correspondence with the lower part of the fabric and decreases with the radial direction, up to the interface with the vessel. At this point the speed of the dye carrier fluid is also the lowest.

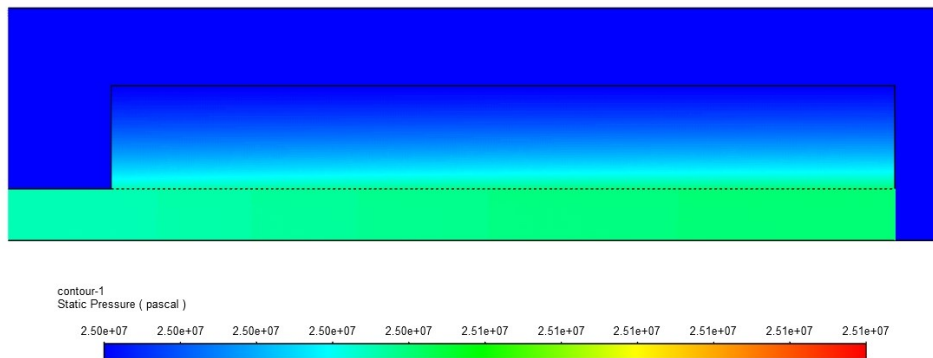


Figure 7-15: Contour of static pressure - perforated beam configuration

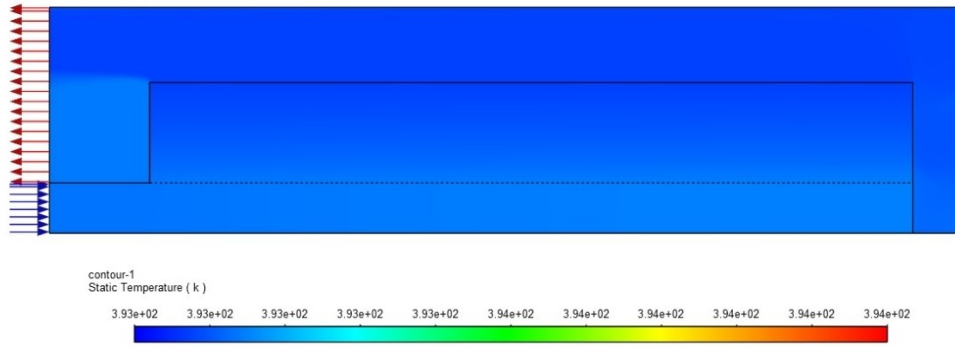


Figure 7-16: Contour of static temperature - perforated beam configuration

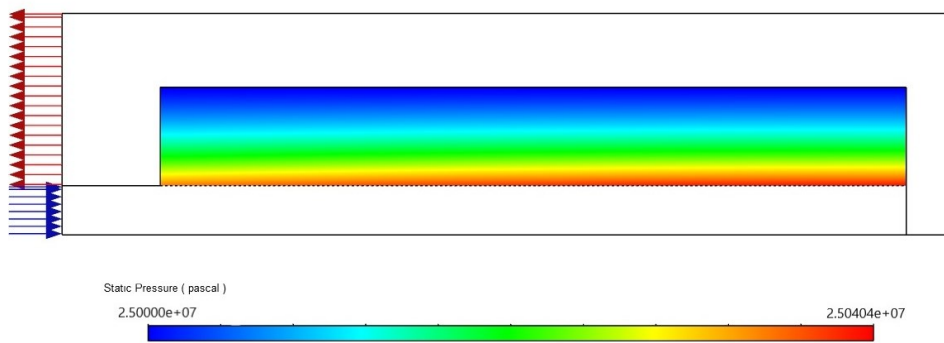


Figure 7-17: Contour of static pressure inside the porous medium - perforated beam configuration

From the previously discussed results it is possible to say that the two configurations give very similar results. To confirm this behaviour a deeper investigation of the scCO₂ velocity distribution inside the fabric is conducted. **Figure 7-18** shows the speed of the scCO₂ in the first layers of the fabric wrapped on the beam: it smooths out to uniform value almost immediately after exiting the holes. The graphical trend is confirmed by the numerical values presented in **Table 7-11**, which reports the average velocity magnitude at fixed y-coordinate inside the porous medium, in the fabric region near the beam. Radial heights of 0.11, 0.12 and 0.13 m were chosen, corresponding respectively to 1, 2 and 3 cm after the interface between the porous and the beam. The deviation between the results obtained with the perforated beam configuration and the simplified one in terms of average velocity magnitude show how immediately after the first layer in contact with the beam, the speed of scCO₂ is practically equal in both the simulations: already after two centimetres the velocity magnitude differs only for the 1%. In **Table 7-11** the scCO₂ velocity magnitude at heights 0.11, 0.12 and 0.13 m inside the fabric are reported.

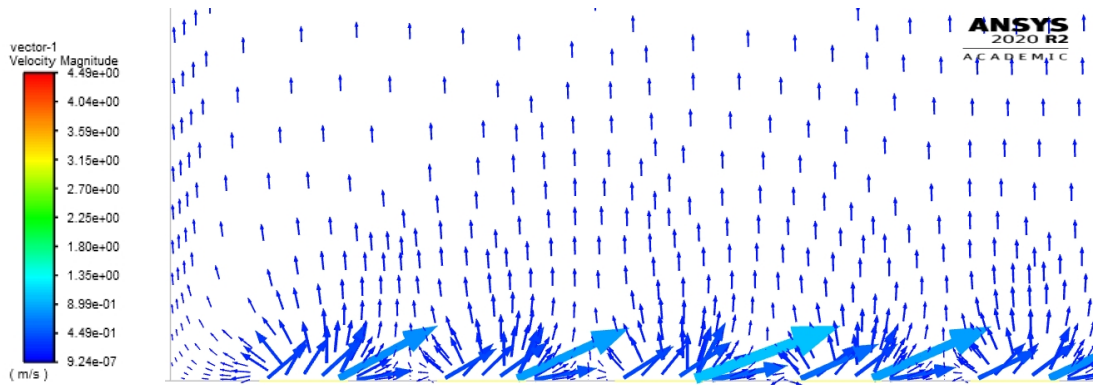


Figure 7-18: Magnification of velocity vectors inside the porous medium - perforated beam configuration

Table 7-11: Average velocity magnitude at fixed y-coordinate (m) inside the porous medium: deviation between perforated beam configuration and simplified one

	Simplified	Perforated	Deviation
average velocity magnitude (m/s) at y=0.11 m	1.15×10^{-1}	1.30×10^{-1}	-13%
average velocity magnitude (m/s) at y=0.12 m	1.21×10^{-1}	1.19×10^{-1}	1%
average velocity magnitude (m/s) at y=0.13 m	1.13×10^{-1}	1.10×10^{-1}	3%

Table 7-12 to **Table 7-15** report the average values of radial velocity, axial velocity, velocity magnitude and ΔP inside the fabric at fixed y-coordinate for both perforated beam configuration and simplified one. It can be concluded that the axial velocity component is very low compared to the radial component, as expected, since the flow is mainly headed in the radial direction. The deviation of 1% in the velocity magnitude is maintained throughout the height of the porous medium, up to the interface with the vessel, as indicated in the following tables. Furthermore, the radial component is the one that dominates in this kind of process, as expected. However, it is evident that the dye carried fluid speed decreases with the height inside the porous.

Table 7-12: Average radial velocity at fixed y-coordinate (m) inside the porous medium: deviation between perforated beam configuration and simplified one

	Simplified	Perforated	Deviation
average radial velocity (m/s) at y=0.2 m	7.34×10^{-2}	7.30×10^{-2}	1%
average radial velocity (m/s) at y=0.3 m	2.65×10^{-2}	2.63×10^{-2}	1%

Table 7-13: Average axial velocity at fixed y-coordinate (m) inside the porous medium: deviation between perforated beam configuration and simplified one

	Simplified	Perforated	Deviation
average axial velocity (m/s) at y=0.2 m	-4.93×10^{-4}	-4.95×10^{-4}	0%
average axial velocity (m/s) at y=0.3 m	-2.64×10^{-5}	-3.56×10^{-5}	-35%

Table 7-14: Average velocity magnitude at fixed y-coordinate (m) inside the porous medium: deviation between perforated beam configuration and simplified one

	Simplified	Perforated	Deviation
average velocity magnitude (m/s) at y=0.2 m	7.34×10^{-2}	7.30×10^{-2}	1%
average velocity magnitude (m/s) at y=0.3 m	2.65×10^{-2}	2.63×10^{-2}	1%

Table 7-15: ΔP inside the porous medium: deviation between perforated beam configuration and simplified one

	Simplified	Perforated	Deviation
ΔP (Pascal)	3.73×10^4	3.85×10^4	-3%

In both cases, the speed increases along the x-axis as shown in **Figure 7-19**. With the simplified beam, a slight further increase takes place in the last part of the beam, near the wall, while with the perforated beam configuration the speed along the fabric is more uniform. In any case, the radial velocity values are quite similar, especially in the final part of the porous medium (at heights $y=0.2$ m and $y=0.3$ m), where practically the two lines overlap.

In conclusion, it can be said that, except for the first two centimetres inside the porous medium, the two configurations are practically similar in terms of flow distribution. Consequently, in order to simplify the problem and reduce the computational cost it has been decided to continue the work choosing the simplified beam configuration.

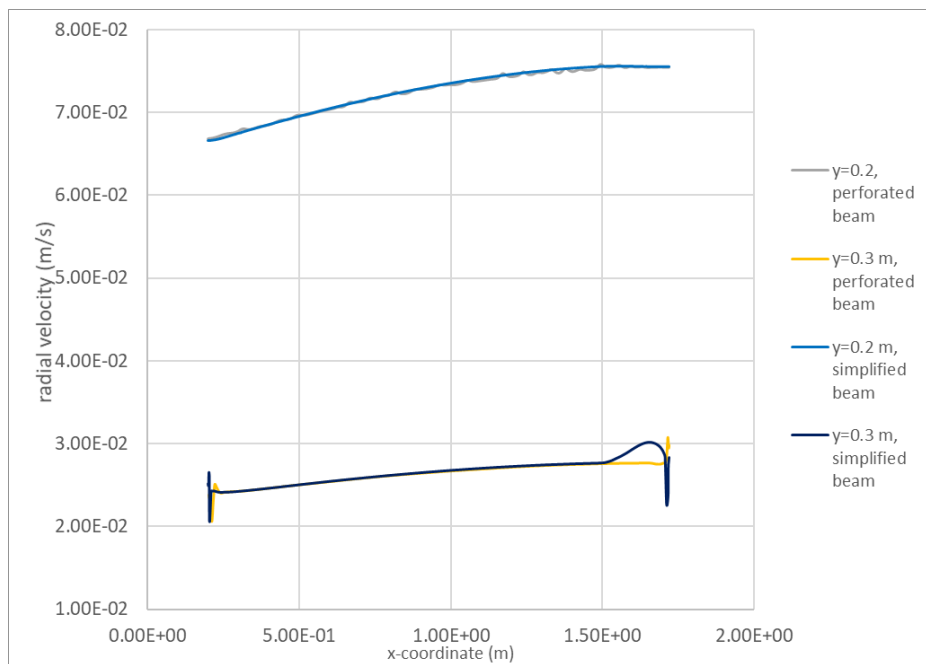


Figure 7-19: Average radial velocity inside the porous medium along the axial direction at fixed y-coordinate (m). Graphical comparison between results of simplified beam and perforated beam configuration.

7.4.4. Flow rate sensitivity analysis

In this section, the flow rate influence on the scCO₂ dyeing process is analysed. This was done increasing the inlet flow rate of the supercritical carbon dioxide from 500 m³/h to 1000 m³/h and keeping constant all the other parameters of the simulations. The operating condition for both the simulations are reported in **Table 7-16**.

Table 7-16: operating conditions for the flow rate sensitivity analysis

	Case A	Case B
Temperature	120 °C	120 °C

Pressure	250 bar	250 bar
scCO₂ flow rate	500 m ³ /h	1000 m ³ /h

In **Figure 7-20** the velocity at different radial heights of the porous medium, representing the fabric wrapped on the beam, can be observed for the Case A. It is evident from the graph that the velocity lines are almost flat; this allows us to say that on average the speed remains fairly uniform along the fabric at the same height. The distribution of the dye flow in various axial positions of the beam allows to make considerations on levelness and since the present work focuses on the flow distribution in the fabric, the levelness terms refer to evenness in flow distribution.

From **Figure 7-21** the velocity along the beam at different radial heights of the porous medium for the Case B is shown. It is possible to see how increasing the flow rate the scCO₂ velocity tends to increase along the x-axis. This uneven speed distribution could result in uneven colouration of the fabric along the axial direction. The behaviour is consistent for all three different heights investigated but is more accentuated at the lower part of the fabric in direct contact with the beam. At higher radial positions inside the porous medium the difference in speed along the x-direction tends to be damped. This result is consistent with the literature [1], where is reported that an increase in mass flow rate through the system leads to higher non-uniformity in distribution.

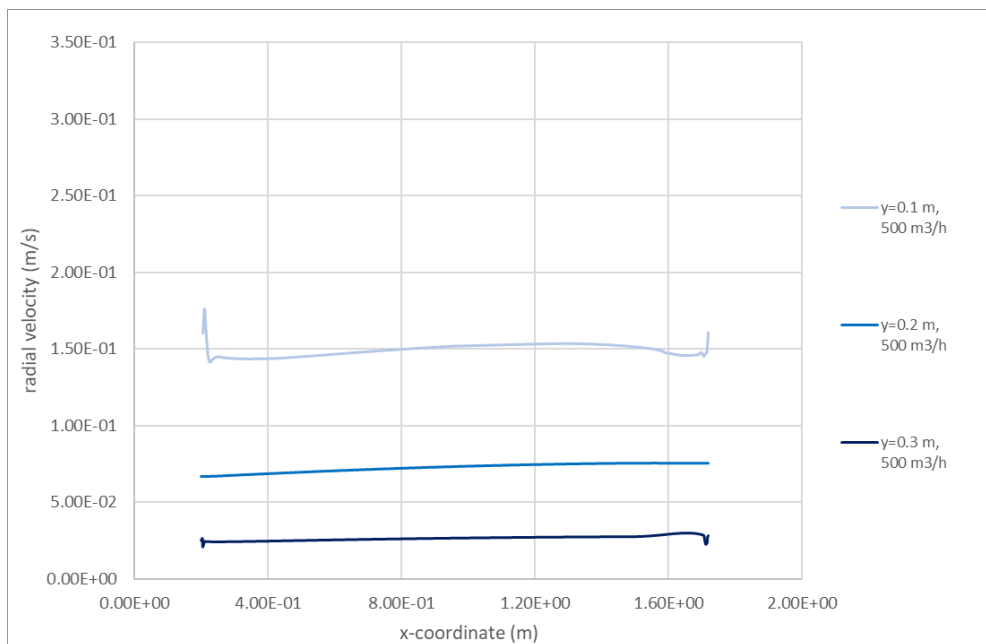


Figure 7-20: Average radial velocity inside the porous medium along the axial direction at fixed y-coordinate (m) - inlet flow rate: 500 m³/h

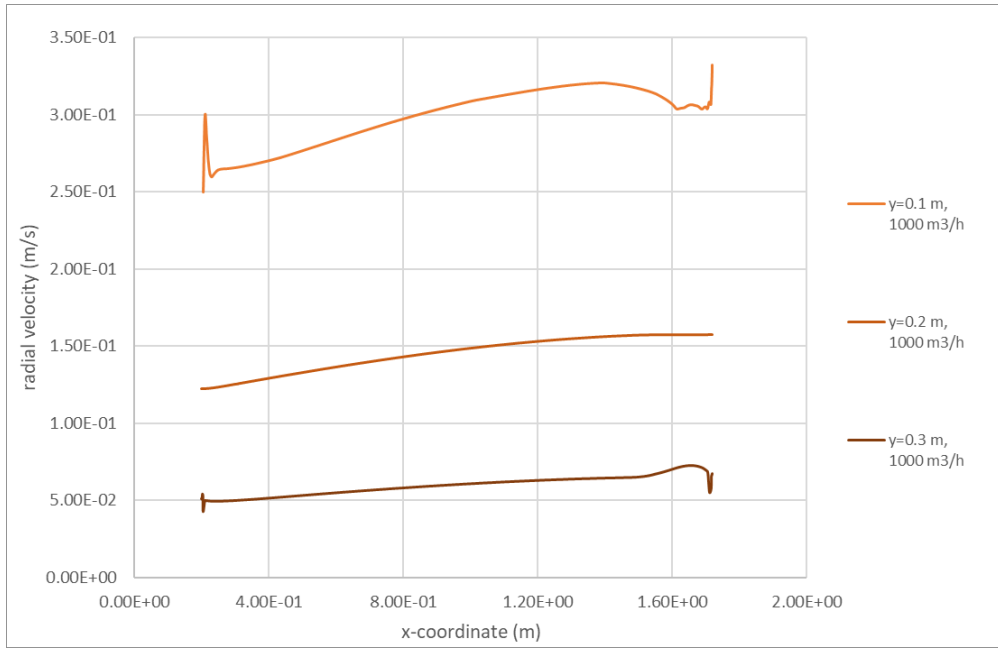


Figure 7-21: Average radial velocity inside the porous medium along the axial direction at fixed y-coordinate (m) - inlet flow rate: 1000 m³/h

The speed of scCO₂ is very high at the inlet and decreases along the beam, as shown in **Figure 7-22**. On the contrary, the velocity of the fluid increases along the x-axis in the porous medium, in fact at the end of the beam the fluid is forced to enter the porous by the side walls of the beam itself.

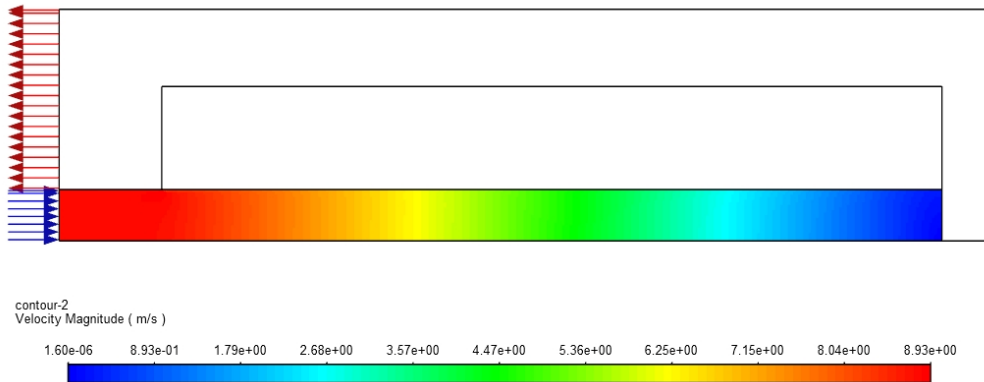


Figure 7-22: Contour of velocity magnitude inside the beam – scCO₂ flow rate: 1000 m³/h

Temperature fields for cases A and B can be evaluated from **Figure 7-23** and from the similar case in the previous paragraph (**Figure 7-11**). Making a graphical comparison, the temperature field is almost the same in both simulations, with an average value of 120 °C in all domain. In Case B, increasing the scCO₂ flow rate at the inlet a pressure increase is observed compared to the previous case, especially along the beam and at interface with the

fabric as shown in **Figure 7-24**. The ΔP inside the porous medium in this case is higher and equal to 7.53×10^4 Pa.

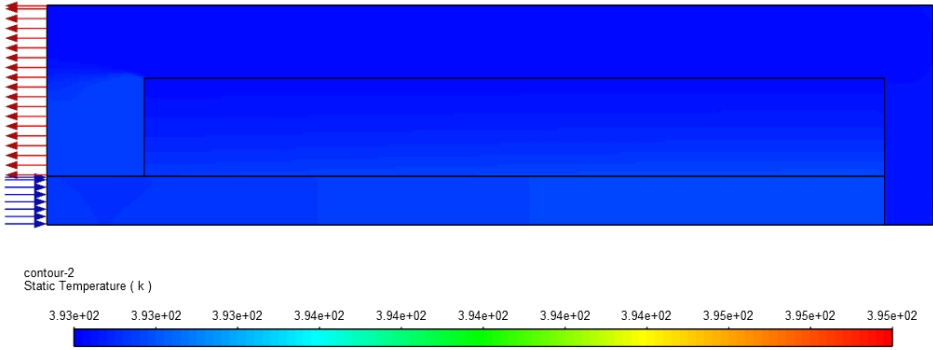


Figure 7-23: Contour of static temperature inside the reactor – scCO₂ flow rate: 1000 m³/h

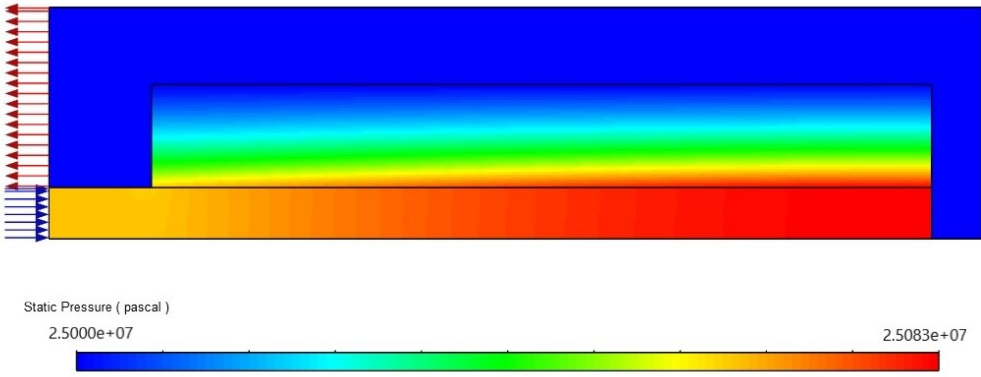


Figure 7-24: Contour of static pressure inside the reactor – scCO₂ flow rate: 1000 m³/h

7.4.5. Influence of fabric permeability

To comprehend the influence of the fabric structure on the scCO₂ distribution inside the vessel, a new set of simulations is presented. In the previous results, the fabric was modelled as porous medium with isotropic permeability and null inertial coefficient, as specified in **Table 7-17**.

Table 7-17: Porous medium inputs, Case A

Case A	
Fabric Permeability, K (m ²)	1.643×10^{-11}
Viscous resistance, $1/K$ (1/m ²)	6.086×10^{10}

Inertial resistance, C_2 (1/m)	0
--	---

The results of the permeability analysis (reported in Chapter 6 for a plain-woven fabric) are used as inputs for the porous media model in ANSYS Fluent to setup the tests presented in this section.

The operating conditions for all the simulations are reported in **Table 7-18**, and are the same used for the Case A (in 7.4.5).

Table 7-18: Operating conditions for the permeability sensitivity analysis

Temperature	120 °C
Pressure	250 bar
scCO₂ flow rate	500 m ³ /h
pCO₂ (120°C, 250 bar)	505.56 kg/m ³

In a first test, the fabric has been modelled as a porous medium with an isotropic permeability equal to the through-thickness permeability of the plain-woven fabric described in Chapter 6. This case is called Case C and the porous medium parameters imposed in ANSYS Fluent are reported in **Table 7-19**.

Table 7-19: Porous medium inputs, Case C

Case C	
Fabric Permeability, K (m²)	4.184×10^{-10}
Viscous resistance, $1/K$ (1/m²)	2.39×10^9
Inertial resistance, C_2 (1/m)	0

Now from the simulation indicates that the pressure difference between the first layer of textile (at the interface with the beam) and the upper part (in correspondence with the vessel interface) is 1.51×10^3 Pa. This value is one order of magnitude lower compared to Case A, reflecting the much higher permeability used in Case C is higher than the one specified in Case A. **Figure 7-25** shows how the pressure field is non-homogeneous along the axial direction, in contrast with the previous cases. Only in correspondence to the final part of the beam, close to the beam wall, the pressure increases, because of the presence of the beam wall and only there the dye carrier fluid is forced to enter the porous material.

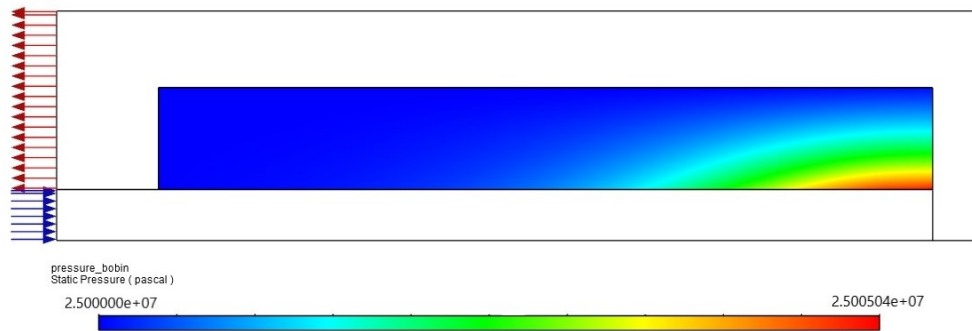


Figure 7-25: Contour of static pressure inside the dyeing reactor - Case C

This behaviour is confirmed by **Figure 7-26**, which shows a comparison between the average radial velocity at fixed radial positions inside fabric for Cases A and C. From this graphical representation it is possible to deduce that the fluid does not enter the fabric bobbin in a homogeneous way, penalizing the initial part of the material. Looking at the scCO_2 velocity distribution inside the fabric it is possible to confirm that higher values are reached in correspondence of the final zone of the porous medium, indeed the scCO_2 radial velocity increases very fast with the axial position. This behaviour can lead to a very non-homogeneous distribution of flow rate inside the porous medium, resulting in an uneven colouring. In fact, there is a disproportion: it seems that in the first half of the length of the fabric the scCO_2 speed is nearly zero while in the second half it is very high.

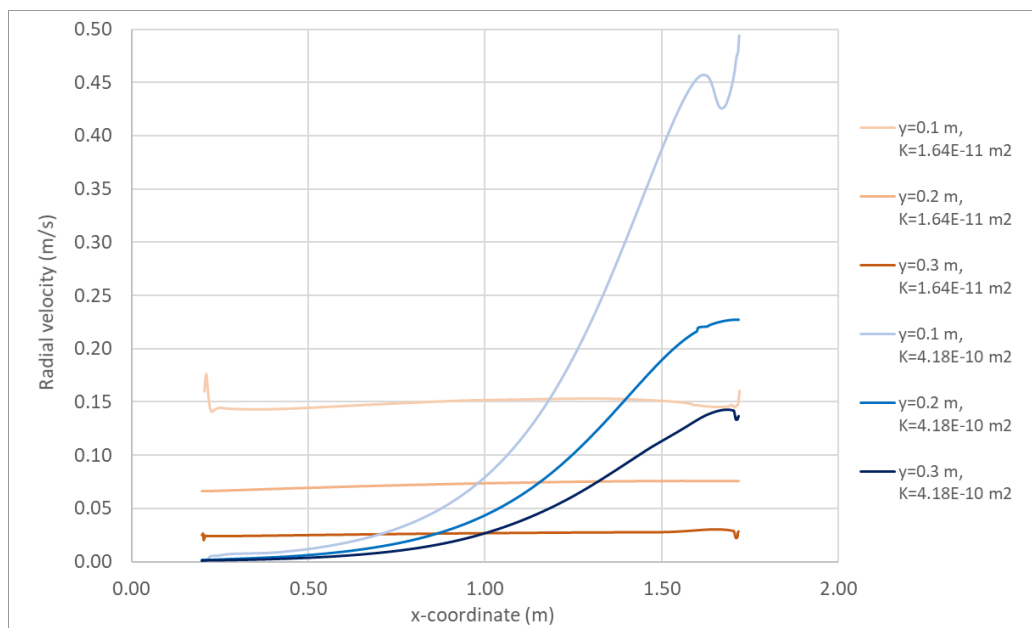


Figure 7-26: Average radial velocity inside the porous medium along the axial direction at fixed y-coordinate (m) – Cases A and C

It is important to highlight that the specified value of K in Case C is higher than that one used for the case A. It seems that specifying higher value of fabric permeabilities uneven flow distributions are obtained. This is confirmed graphically by **Figure 7-27**, in which the scCO_2

velocity distribution through the fabric at the interface with the beam is compared to the one obtained prescribing different permeabilities of the porous medium. In particular, other two permeabilities were simulated, in addition to cases A and C: one intermediate between the two cases ($8.00 \times 10^{-11} \text{ m}^2$) and one with lower value ($8.00 \times 10^{-12} \text{ m}^2$). Their trend is consistent: increasing the fabric permeability, the scCO_2 radial velocity became non-homogeneous, increasing considerably with the axial direction.

This behaviour could be interesting when considering tests with more permeable fabrics: in fact, from the analysis reported in Chapter 5, knitted fabrics are in general more permeable to air with respect to woven fabrics. Hence, those types of fabrics have a high permeability due to their particular structure. Referring to these data, it could be presumed that knitted fabrics would probably face the problem of a non-homogeneous flow distribution.

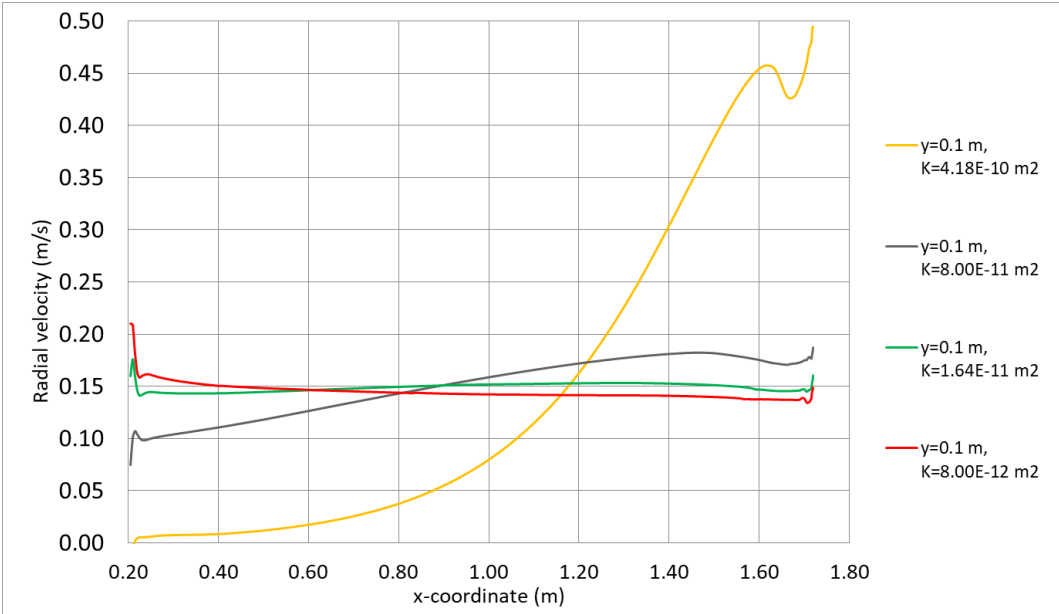


Figure 7-27: Supercritical carbon dioxide velocity distribution through the fabric at the interface with the beam. Same operating conditions but different permeability of the porous medium

Another issue to consider is that the permeability value imposed in Case C is referred to a single layer of woven fabric, resulting of course in higher permeability of the fabric than considering more layers overlapped. For this purpose, it has to be highlighted that fabric permeability is mainly influenced by the gaps between yarns, which represent the preferential path for the fluid. Overlapping different layers of fabric probably obstructs the gaps between yarns, preventing the fluid flow within the structure. An interesting improvement could be to simulate the behaviour of the air flow through various layers of fabric and observe how it influences permeability.

Another test (Case D) has been set in which the fabric was modelled as porous medium with an isotropic permeability, this time taking into account also the inertial coefficient (C_2). The values specified in the simulation are those obtained from the through-thickness permeability analysis performed in the previous chapter for a plain-woven fabric, reported in **Table 7-20**.

Table 7-20: Porous medium inputs, Case D

Case D	
Fabric Permeability, K (m^2)	4.184×10^{-10}
Viscous resistance, $1/K_T$ ($1/m^2$) (isotropic)	2.39×10^9
Inertial resistance, C_2 ($1/m$) (isotropic)	1.15×10^5

Considering the inertial resistance of the fabric, the results of the simulations are totally different from the previous case, demonstrating that the contribution of the inertial term on the flow distribution is high. More homogeneous speed and pressure were obtained in this case, hence inertial effects return a sort of levelling in the speed and pressure field. This behaviour is confirmed graphically by **Figure 7-28** and **Figure 7-29**, from which is possible to notice that the vectors of velocity of the fluid are homogenous both in distribution and magnitude.

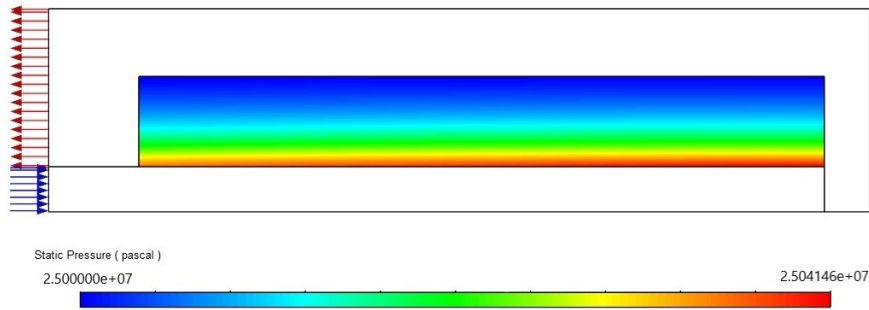


Figure 7-28: Contour of static pressure inside the fabric bobbin – Case D

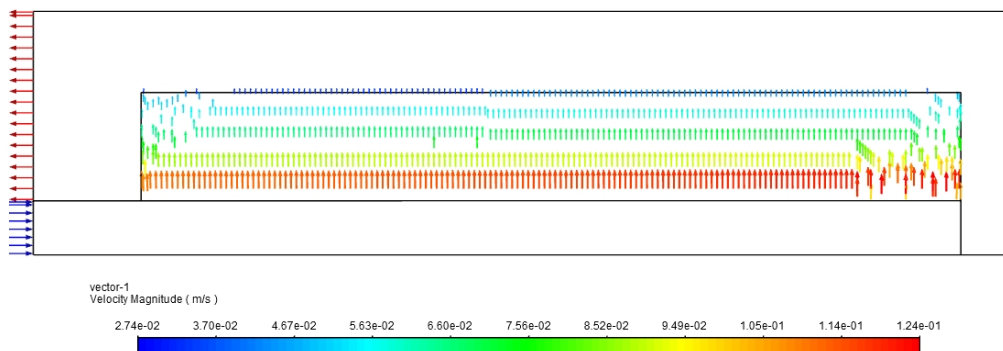


Figure 7-29: Vectors of velocity magnitude - porous material

These results are more plausible and show a uniform trend in speed and pressure distribution both inside the dyeing vessel and the fabric (**Figure 7-30**). In fact, although the velocity magnitude is extremely low in large part of the porous medium, in the first layers of the fabric in contact with the beam the scCO₂ velocity magnitude has the highest value. This behaviour is maintained for the whole fabric length, as shown in **Figure 7-29**, which is a graphical representation of the vectors inside the fabric coloured by their velocity magnitude. Moreover, their direction is maintained uniform in all the bobbin. The pressure drop inside the porous region is equal to 3.90×10^4 Pa, which is an higher value with respect to Case C, from which a deviation of 96% is obtained.

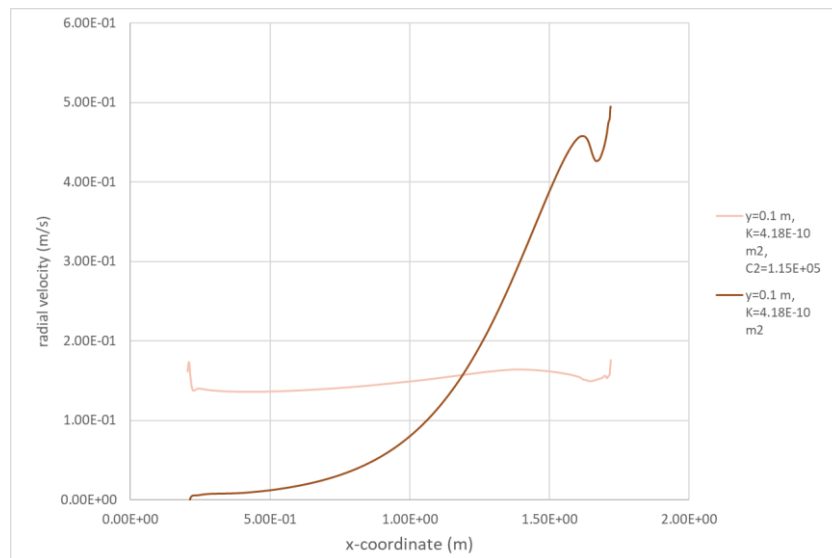


Figure 7-30: Average radial velocity inside the porous medium along the axial direction at the inlet of the porous medium – Cases C and D

These results show a completely different behaviour in velocity distribution inside the fabric, resulting in high deviations from Case C, although the same permeability value was specified. The main difference between them is the presence of the inertial contribution (which is taken into account specifying C_2) in the momentum equation for the porous medium (reported in Chapter 5). The greatest deviation is obtained in correspondence of the final part of the porous medium, which is the preferred fluid path in Case C. From this comparison it seems that the inertial term is important in applying a sort of levelling in the flow distribution within the porous medium.

Although the two trends are very different, it is possible to make some considerations about the term K and its influence, too. The high permeability value set in this simulation also influences the radial velocity distribution in the radial direction within the porous region. From **Figure 7-31** it is possible to observe the effect of the high permeability value by observing the final section of the curves. This shows that the high permeability value results in a non-homogeneous flow distribution at inlet, as previously seen, but the scCO₂ radial

velocity tends to become more uniform with the increase of radial height within the porous material.

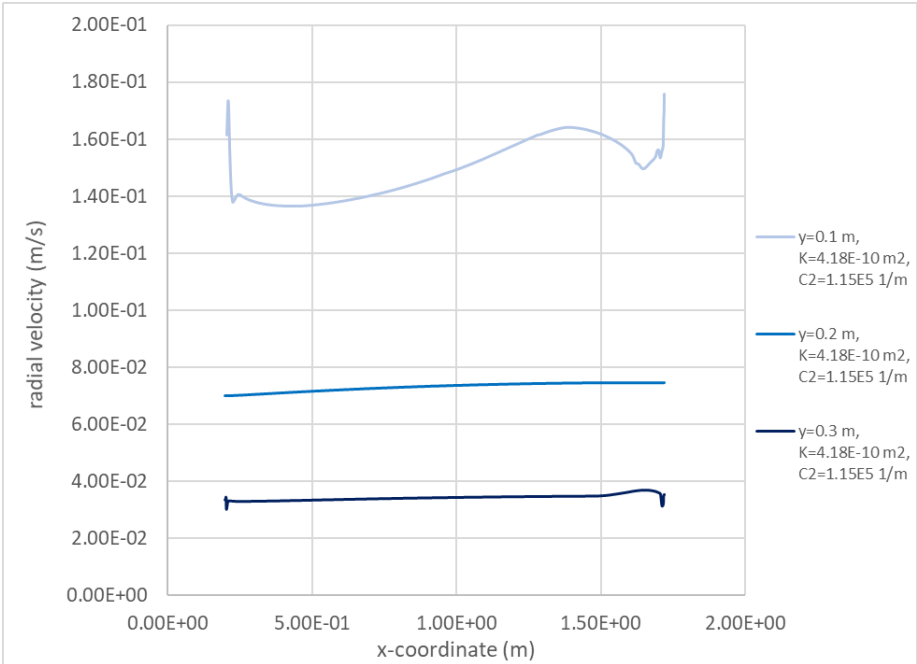


Figure 7-31: Average radial velocity inside the porous medium along the axial direction at fixed y-coordinate (m) – Case D

The last case (Case E) refers to the CFD simulation in which the fabric was modelled as porous medium with an anisotropic permeability, considering both the in-plane permeability and through-thickness permeability value (K_T , K_P) and the relative inertial coefficients (C_2 , C_2') obtained for the plain-woven fabric reported in Chapter 6. The porous medium parameters specified for the Case E on the software are reported in **Table 7-21**.

Table 7-21: Porous medium inputs, Case E

Case E	
Viscous resistance, $1/K_T$ ($1/m^2$) (radial direction)	2.39×10^9
Inertial resistance, C_2 ($1/m$) (radial direction)	1.15×10^5
Viscous resistance, $1/K_P$ ($1/m^2$) (axial direction)	1.13×10^9

Inertial resistance, C_2' (1/m) (axial direction)	3.00×10^4
---	--------------------

As it can be seen, the results are quite similar to those of the Case D, in which an isotropic permeability was considered. This may be justified by the fact that the axial velocity component is much lower than the radial component, that in fact dominates the system behaviour, therefore the in-plane permeability value has a very little influence on the behaviour of the whole system, from a fluid dynamic point of view. In **Figure 7-32** a contour of the axial velocity inside the fabric wrapped on the beam is shown; from this figure is clear that the axial component of the scCO₂ velocity is very small in the whole fabric domain. The low influence of in-plane permeability on the behaviour of the system is an expected result: what influences the scCO₂ flow inside the fabric is the radial component of velocity and consequently the corresponding inertial and permeability constants. For this purpose in Case D, where the assumption of isotropic the permeability has been made, K is set equal to the through-thickness permeability of the fabric.

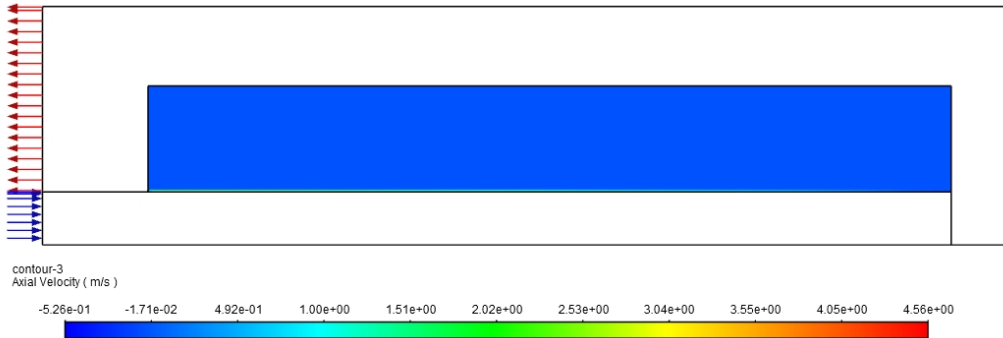


Figure 7-32: Contour of axial velocity inside the fabric bobbin – Case E

The pressure field in these conditions is almost the same as Case D (showed in **Figure 7-33**). Hence, also the pressure drop inside the porous has in practice no deviation (-0.08%) from Case D, and is equal to a 3.91×10^4 Pa. A comparison of the result obtained for Case D and E is reported in **Table 7-22**.

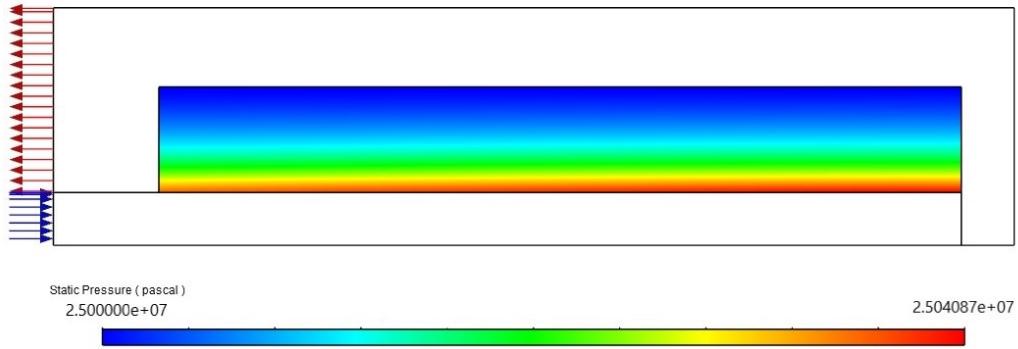


Figure 7-33: Contour of static pressure inside the fabric bobbin – Case E

Table 7-22: Average radial velocity: deviation between Case D and E

Radial position (m)	average radial velocity (m/s)	Deviation with CASE D
0.1	1.48×10^{-1}	-0.89%
0.2	7.38×10^{-2}	-0.13%
0.3	3.42×10^{-2}	-0.13%

8. Conclusions

In this thesis, the industrial scale scCO₂ dyeing machine by the Dutch engineering company DyeCoo has been modelled using the software ANSYS Fluent. First, the state-of-the-art of the scCO₂ dyeing technology and numerical simulations of the scCO₂ beam dyeing process has been analysed. Then, the attention has been focused on the influence of the beam structure, the scCO₂ inlet flow rate and the fabric structure, in order to investigate the flow distribution inside the dyeing vessel.

Two types of fabrics, woven and knitted, were compared in terms of air permeability and geometrical structure in order to understand whether the type of fabric plays a role when dyed in scCO₂ medium. Since fabrics were modelled as porous media on ANSYS Fluent, permeability is important to investigate the distribution of supercritical CO₂ inside the fabric. For this purpose, three-dimensional CFD simulations were carried out to characterize the permeability constants of a plain-woven fabric. The air permeability test conducted on fabrics according to the standard EN ISO9237:1997 has been reproduced, in fact, this methodology has been validated by comparing the results with experimental data from literature. Inertial constants in both axial and radial direction and fabric permeability components (in-plane permeability and through thickness permeability) were obtained from the simulations for a plain-woven fabric. These values have been used in the second part of the work, which was focused to modelling the scCO₂ dyeing vessel in ANSYS Fluent.

In the second part of the work, the influence of different parameters of the scCO₂ dyeing process was studied. It was demonstrated that the porous structure of the beam does not have much influence on the scCO₂ flow distribution. In fact, if the pores are small with respect of the global dimensions of the systems, the speed of the scCO₂ in the first layers of the fabric wrapped on the beam becomes uniform almost immediately out from the holes.

Another interesting result is that increasing the scCO₂ inlet flow rate, scCO₂ radial velocity tends to increase with the beam length at fixed heights inside the porous medium. This reflects an uneven velocity distribution, which could result in non-uniform colouration of the fabric along the axial direction. This behaviour is consistent in all the height of the fabric bobbin but is more accentuated at the contact with the beam, where the scCO₂ firstly permeates the fabric. This result is consistent with the literature [1], where it is reported that an increase in mass flow rate through the system leads to higher non-uniform distribution. Indeed, a good and homogeneous distribution of the flow inside the porous medium is necessary to reach the desirable level of dyeing of the fabric itself.

To comprehend the influence of the fabric structure on the scCO₂ distribution inside the vessel, and particularly inside the porous material, additional simulations were done. Firstly, isotropic permeability, equal to through-thickness permeability of a plain-woven fabric, was specified for the porous medium. The results showed that higher value of fabric permeability results in uneven flow distributions. In fact, it was demonstrated that increasing porous medium permeability, the scCO₂ radial velocity became non-homogeneous, increasing considerably along the axial length. This could be relevant when more permeable fabrics are considered: in fact, from the analysis reported in Chapter 5, it was concluded that knitted fabrics are in general more permeable to air with respect to woven fabrics. Referring to these data, knitted fabrics would probably face the problem of a non-homogeneous flow distribution. An important factor to consider is that the permeability value imposed in this

simulation refers to a single layer of woven fabric, resulting of course in a higher permeability than considering more fabric layers overlapped. This could be considered a limitation of the model; hence, an interesting improvement could be to simulate the behaviour of the air flow through various layers of fabric overlapped and observe how it affects permeability. A further result was obtained by considering not only permeability but also the inertial coefficient of the fabric, that is important when the velocities of the fluid within the porous material are higher and therefore the hypothesis of direct proportionality between ΔP and velocity is no longer reasonable. This condition affects the first part of the porous thickness in contact with the perforated beam in which the scCO₂ reaches the highest velocity values. The results show that the inertial term is crucial for describing the scCO₂ flow in the porous accurately. By making this adjustment it has been found that the scCO₂ velocity distribution changes significantly obtaining much more homogeneous flow distribution and pressures within the fabric. Hence, it was concluded that inertial effects return a sort of levelling in the velocity and pressure field when a fabric with high permeability is considered. Moreover, it was found that the velocity and pressure fields are similar regardless the porous medium is considered anisotropic or isotropic. Therefore, the permeability value was assumed uniform and equal to the permeability through the thickness. This was an expected result, which allows to conclude that the scCO₂ flow inside the fabric is mainly radial and consequently the corresponding inertial and permeability constants are sufficient to describe the system fluid dynamics.

To conclude, the present work was mainly focused on three main parameters of the process (mass-flow rate, pressure and temperature) and their influence on the scCO₂ flow rate distribution inside the porous medium. It was limited to the evaluation of the flow characteristics of the beam dyeing machine, not considering the presence of the dye. Hence, as a future improvement could be simulated the mixture of scCO₂ and dye on ANSYS Fluent.

One of the possible developments of the present work could be the estimation of the fabric permeability of the overall system made of several layer of fabrics.

Finally, it would be interesting to use three-dimensional CFD also to characterize the permeability constants of a knitted fabric. Consequently, once obtained the porous media features, a comparison between woven and knitted fabric behaviour in terms of scCO₂ flow distribution could be made for the scCO₂ dyeing process.

List of tables

Table 4-1: Differences between conventional aqueous dyeing and scCO ₂ dyeing. Adapted by [13]	29
Table 6-1: Characteristics of the chosen fabric sample (plain woven).....	58
Table 6-2: Cotton yarn permeability.....	62
Table 6-3: Deviation of the air permeability values calculated from the simulations and the experimental data	62
Table 6-4: Results of the first set of simulations – through-thickness permeability	63
Table 6-5: Results considering scCO ₂ as fluid - through-thickness permeability.....	64
Table 6-6: Results of the second set of simulations – through-thickness permeability.....	65
Table 6-7: Results of the simulations - through-thickness permeability	66
Table 6-8: Results from the first set of simulations – in-plane permeability.....	68
Table 6-9: Results from the second set of simulations – in-plane permeability	69
Table 6-10: Results of the simulations – in-plane permeability	70
Table 7-1: Radial thickness of the fabric wounded on the beam	73
Table 7-2: Mesh details, simplified beam.....	74
Table 7-3: Mesh details, perforated beam.....	75
Table 7-4: Operating conditions	77
Table 7-5: Grid independence study, simplified beam configuration	78
Table 7-6: Grid independence study, deviation of average velocity magnitude at fixed y-coordinate (m) and deviation of ΔP inside the porous medium - Simplified beam configuration.....	79
Table 7-7: Grid independence study, perforated beam configuration.....	81
Table 7-8: Grid independence study, deviation of average velocity magnitude at fixed y-coordinate (m) and deviation of ΔP inside the porous medium – Perforated beam configuration.....	81
Table 7-9: Results of average velocity magnitude at fixed y-coordinate (m) inside the porous medium - Perforated beam configuration, M3.....	82
Table 7-10: Results of average ΔP inside the porous medium - Perforated beam configuration, M3.....	82
Table 7-11: Average velocity magnitude at fixed y-coordinate (m) inside the porous medium: deviation between perforated beam configuration and simplified one	86
Table 7-12: Average radial velocity at fixed y-coordinate (m) inside the porous medium: deviation between perforated beam configuration and simplified one	87
Table 7-13: Average axial velocity at fixed y-coordinate (m) inside the porous medium: deviation between perforated beam configuration and simplified one	87

Table 7-14: Average velocity magnitude at fixed y-coordinate (m) inside the porous medium: deviation between perforated beam configuration and simplified one	87
Table 7-15: ΔP inside the porous medium: deviation between perforated beam configuration and simplified one	87
Table 7-16: operating conditions for the flow rate sensitivity analysis	88
Table 7-17: Porous medium inputs, Case A.....	91
Table 7-18: Operating conditions for the permeability sensitivity analysis	92
Table 7-19: Porous medium inputs, Case C.....	92
Table 7-20: Porous medium inputs, Case D.....	95
Table 7-21: Porous medium inputs, Case E.....	97
Table 7-22: Average radial velocity: deviation between Case D and E.....	99
Table 0-1: Air permeability data from Ettehadi et al. [67] (knitted).....	115
Table 0-2: Air permeability data from Dehkordi et al. [60] (knitted)	115
Table 0-3: Air permeability data from Zupin et al. [51] (woven)	115
Table 0-4: Air permeability data from Karaca et al. [66] (woven)	117

List of figure

Figure 2-1: Process development by simulation compared to conventional method [2]	4
Figure 2-2: Two-dimensional rectangular cell [5]	5
Figure 2-3: Graphical representation of the difference between structured (left) and an unstructured (right) cross-linking [2]	6
Figure 2-4: Small fluid element for the conservation equations [3].....	7
Figure 2-5: Mass flow of the fluid elements (in and out) [3].....	7
Figure 2-6: x-direction stress component [3].....	8
Figure 2-7: Turbulent flow: a typical point velocity measurement [3]	11
Figure 3-1: Single substance phase diagram.....	19
Figure 3-2: Phase diagram of pure carbon dioxide [12].....	20
Figure 4-1: Graphical representation of pollution route in textile industry. Adapted by [13].	28
Figure 4-2: Steps of the polyester dyeing process in scCO ₂	31
Figure 4-3: DyeCoo reactor [29].....	36
Figure 4-4: DyeCoo simplified process diagram [30].....	36
Figure 4-5: Geometry and boundary conditions, Reji et al. [1]	38
Figure 5-1: Example of a plain weave structure	41
Figure 5-2: Example of a weft-knit fabric structure.	41
Figure 5-3: Hexagonal fibre packing, adapted by [46].....	45
Figure 5-4: Quadratic fibre packing, adapted by [46]	45
Figure 5-5: Simplified representation of gaps between yarns. Adapted by [42]	47
Figure 5-6: Unit cell of fabric and channel geometry [42]	47
Figure 5-7: Interlayer micro-geometry, Chen et al. (a) straight channel, (b) tortuous channel, (c) non-interconnected. [58].....	49
Figure 5-8: Structure of the samples tested by Zupin et al. [64].....	51
Figure 5-9: Air permeability data from Zupin et al. [66].....	51
Figure 5-10: Air permeability data from Karaca et al. [66].....	52
Figure 5-11: Warp-knitted fabrics samples tested by Ettehadi et al. [67]	52
Figure 5-12: Air permeability data from Ettehadi et al. [66]	53
Figure 5-13: Fabrics samples tested by Dehkordi et al. [60]	53
Figure 5-14: Air permeability data from Dehkordi et al. [66]	54
Figure 5-15: Comparison between air permeability of woven and knitted fabrics with different thickness	54

Figure 5-16: Comparison between air permeability of woven and knitted fabrics with different mass (g/m^2)	55
Figure 5-17: Comparison between air permeability of woven and knitted fabrics with different density (kg/m^3).....	55
Figure 6-1: Base unit of plain woven fabric generated with TexGen	59
Figure 6-2: Geometry for the through-thickness permeability simulations of the woven fabric in ANSYS Fluent	59
Figure 6-3: Mesh for the through-thickness permeability simulations of the woven fabric in ANSYS Fluent - Entire domain	60
Figure 6-4: Mesh for the through-thickness permeability simulations of the woven fabric in ANSYS Fluent – Entire domain (magnification).....	60
Figure 6-5: Mesh for the through-thickness permeability simulations of the woven fabric in ANSYS Fluent – Fabric domain	61
Figure 6-6: Boundary conditions - through-thickness permeability simulations of the woven fabric.....	61
Figure 6-7: Pathlines of the air flowing through the fabric domain.....	63
Figure 6-8: Plot of pressure drop versus air velocity – first set of simulations, through-thickness permeability	64
Figure 6-9: Plot of pressure drop versus air velocity – second set of simulations, through-thickness permeability	65
Figure 6-10: Geometry for the in-plane permeability simulations of the woven fabric in ANSYS Fluent	66
Figure 6-11 Mesh for the in-plane permeability simulations of the woven fabric in ANSYS Fluent (magnification).....	67
Figure 6-12: Mesh for the in-plane permeability simulations of the woven fabric in ANSYS Fluent – fabric domain.....	67
Figure 6-13: Plot of pressure drop versus air velocity – first set of simulations, in-plane permeability	69
Figure 6-14: Plot of pressure drop versus air velocity – second set of simulations, in-plane permeability	70
Figure 7-1: Two-dimensional axisymmetric domain on ANSYS Fluent.....	73
Figure 7-2: Two-dimensional axisymmetric domain for the perforated beam construction ...	74
Figure 7-3: Computational domain for the simplified beam geometry in ANSYS Fluent.....	74
Figure 7-4: Computational domain for the simplified beam geometry in ANSYS Fluent (magnification).....	74
Figure 7-5: Computational domain for the perforated beam geometry, perforated beam interface with the porous medium.....	75
Figure 7-6: Subdivisions of the near-wall region [7]	76

Figure 7-7 Computational domain and boundary conditions.....	78
Figure 7-8: Two-dimensional axisymmetric geometry, lines at $y=0.1$ m, $y=0.2$ m and $y=0.3$ m are highlighted.....	79
Figure 7-9: Contour of velocity magnitude inside the porous medium (m/s), mesh M3	80
Figure 7-10: Contour of velocity magnitude inside the porous medium (m/s), mesh M4	80
Figure 7-11: Contour of static temperature - simplified beam configuration.....	83
Figure 7-12: Contour of static pressure - simplified beam configuration	83
Figure 7-13: Contour of static pressure inside the porous medium - simplified beam configuration.....	83
Figure 7-14: Pathlines coloured by velocity magnitude - simplified beam configuration	84
Figure 7-15: Contour of static pressure - perforated beam configuration.....	84
Figure 7-16: Contour of static temperature - perforated beam configuration.....	85
Figure 7-17: Contour of static pressure inside the porous medium - perforated beam configuration.....	85
Figure 7-18: Magnification of velocity vectors inside the porous medium - perforated beam configuration.....	86
Figure 7-19: Average radial velocity inside the porous medium along the axial direction at fixed y -coordinate (m). Graphical comparison between results of simplified beam and perforated beam configuration.	88
Figure 7-20: Average radial velocity inside the porous medium along the axial direction at fixed y -coordinate (m) - inlet flow rate: $500 \text{ m}^3/\text{h}$	89
Figure 7-21: Average radial velocity inside the porous medium along the axial direction at fixed y -coordinate (m) - inlet flow rate: $1000 \text{ m}^3/\text{h}$	90
Figure 7-22: Contour of velocity magnitude inside the beam – scCO_2 flow rate: $1000 \text{ m}^3/\text{h}$	90
Figure 7-23: Contour of static temperature inside the reactor – scCO_2 flow rate: $1000 \text{ m}^3/\text{h}$	91
Figure 7-24: Contour of static pressure inside the reactor – scCO_2 flow rate: $1000 \text{ m}^3/\text{h}$	91
Figure 7-25: Contour of static pressure inside the dyeing reactor - Case C	93
Figure 7-26: Average radial velocity inside the porous medium along the axial direction at fixed y -coordinate (m) – Cases A and C	93
Figure 7-27: Supercritical carbon dioxide velocity distribution through the fabric at the interface with the beam. Same operating conditions but different permeability of the porous medium	94
Figure 7-28: Contour of static pressure inside the fabric bobbin – Case D.....	95
Figure 7-29: Vectors of velocity magnitude - porous material	95
Figure 7-30: Average radial velocity inside the porous medium along the axial direction at the inlet of the porous medium – Cases C and D.....	96

Figure 7-31: Average radial velocity inside the porous medium along the axial direction at fixed y-coordinate (m) – Case D97

Figure 7-32: Contour of axial velocity inside the fabric bobbin – Case E98

Figure 7-33: Contour of static pressure inside the fabric bobbin – Case E99

Bibliography

- [1] R. Reji, S. Raman, T. Kim and H. Kim, "Computational fluid dynamics simulation of the supercritical carbon dioxide flow in beam dyeing," *Textile Research Journal*, vol. 89, no. 13, pp. 2604-2615, 2019.
- [2] P. Jungbecker and D. Veit, *Simulation in Textile Technology, Theory and Applications*, RWTH Aachen University, Germany: Woodhead Publishing Series in Textiles, 2012.
- [3] H. Versteeg and W. Malalasekera, *An Introduction to Computational Fluid Dynamics*, Pearson, 2007.
- [4] C. Hirsch, *Numerical Computation of Internal and External Flows*, Oxford: Butterworth-Heinemann, 2007.
- [5] R. Bhaskaran and L. Collins, "Introduction to CFD Basics," *Lecture notes*, 2003.
- [6] ANSYS Fluent User's Guide, Canonsburg, PA: ANSYS, Inc., 2013.
- [7] ANSYS Fluent Theory Guide, Canonsburg,: ANSYS, Inc., 2013.
- [8] R. Van Eldik and C. Hubbard, *Comprehensive Organometallic Chemistry III*, Elsevier Science, 2007.
- [9] G. Brunner, "Applications of Supercritical Fluids," *Annual Review of Chemical and Biomolecular*, vol. 1, pp. 312-42, 2010.
- [10] D. Green and R. Perry, *Perry's chemical engineers' handbook*, McGraw-Hill, 2007.
- [11] M. Sihvonen, E. Jarvenpaa, V. Hietaniemi and R. Huopa, "Advances in supercritical carbon dioxide technologies," *Trends in Food Science & Technology*, vol. 10, pp. 217-222, 1999.
- [12] J. DeSimone and W. Tumas, *Green Chemistry using liquid and supercritical carbon dioxide*, USA: New York Oxford University Press, 2003.
- [13] S. Muthu and G. Gardetti, *Sustainability in the Textile and Apparel Industries*, Switzerland: Springer, 2020.
- [14] H. Eren, O. Avinc and S. Eren, "Supercritical carbon dioxide for textile applications and recent developments," *IOP Conference Series: Materials Science and Engineering*, pp. 254. 082011. 10.1088/1757-899X/254/8/082011., 2017.
- [15] H. Zheng, J. Zhang, J. Yan and L. Zheng, "An industrial scale multiple supercritical

- carbon dioxide apparatus and its eco-friendly dyeing production,” *Journal of CO2 utilization*, vol. 16, pp. 272-281, 2016.
- [16] C. Hicks and R. Dietmar, “Improving cleaner production through the application of environmental management tools in China,” *Journal of Cleaner Production*, vol. 15, no. 5, pp. 395-408, 2007.
- [17] M. Banchemo, “Recent advances in supercritical fluid dyeing,” *Coloration technology*, vol. 136, pp. 317-335, 2020.
- [18] E. Bach, E. Cleve and E. Schollmeyer, “Past, present and future of supercritical fluid dyeing technology - an overview,” *Review of Progress in Coloration and Related Topics*, vol. 32, pp. 88-102, 2002.
- [19] W. Saus, D. Knittel and E. Schollmeyer, “Dyeing of Textiles in Supercritical Carbon Dioxide,” *Textile Research Journal*, pp. 135-142, 1993.
- [20] M. van der Kraan, M. Fernandez Cid, G. Woerlee, W. Veugelers and G. Witkamp, “Dyeing of natural and synthetic textiles in supercritical carbon dioxide with disperse reactive dyes,” *Journal of Supercritical Fluids*, vol. 40, pp. 470-476, 2007.
- [21] G. Montero, C. Smith, W. Hendrix and D. Butch, “Supercritical Fluid Technology in Textile Processing: An Overview,” *Industrial & engineering chemistry research*, vol. 39, pp. 4806-4812, 2000.
- [22] M. Banchemo, “Supercritical fluid dyeing of synthetic and natural textiles – a review,” *Coloration Technology*, vol. 129, pp. 2-17, 2012.
- [23] E. Abd El-Aziz and T. Abou Elmaaty, “Supercritical carbon dioxide as a green media in textile dyeing: A review,” *Textile Research Journal.*, vol. 88, no. 10, pp. 1184-1212, 2018.
- [24] A. Schmidt, E. Bach and E. Schollmeyer, “Damage to Natural and Synthetic Fibers Treated in Supercritical Carbon Dioxide at 300 bar and Temperatures up to 160°C,” *Textile research journal*, vol. 72, no. 11, pp. 1023-1032, 2002.
- [25] A. Hou and J. Dai, “Kinetics of dyeing of polyester with CI Disperse Blue 79 in supercritical carbon dioxide,” *Coloration Technology*, vol. 121, no. 1, pp. 18-20, 2006.
- [26] T. Huang, H. Cui, D. Yang, X. Kong and J. Lin, “Continuous dyeing processes for zipper tape in supercritical carbon dioxide,” *Journal of Cleaner Production*, vol. 158, pp. 95-100, 2017.
- [27] M. T. Abate , S. Seipel, J. Yu, M. Viková, M. Vik, A. Ferri, J. Guan, G. Chen and V. Nierstrasz, “Supercritical CO2 dyeing of polyester fabric with photochromic dyes to fabricate UV sensing smart textiles,” *Dyes and Pigments*, vol. 183, 2020.

- [28] T. Huang, X. Kong, H. Cui, T. Zhang, W. Li, P. Yu and J. Lin, “Waterless dyeing of zipper tape using pilot-scale horizontal supercritical carbon dioxide equipment and its green and efficient production,” *Journal of Cleaner Production*, vol. 233, pp. 1097-1105,, 2019.
- [29] “DyeCoo,” DyeCoo, 2019. [Online]. Available: <http://www.dyecoo.com/dyecoo/wp-content/uploads/2019/09/BNid-DyeCoo-Brochure-cor-120919.pdf>. [Accessed 2 February 2021].
- [30] “DyeCoo,” DyeCoo, 2019. [Online]. Available: <http://www.dyecoo.com/dyecoo/wp-content/uploads/2020/01/BNiD-DyeCoo-Techspec-cor-210120-Online.pdf>. [Accessed 2 February 2021].
- [31] S. Hepburn, “The Guardian,” Guardian News & Media Limited, 2021. [Online]. Available: <https://www.theguardian.com/sustainable-business/sustainable-fashion-blog/2015/apr/24/nike-and-adidas-show-cautious-support-for-eco-friendly-dye-technology>. [Accessed 3 February 2021].
- [32] D. Karst, W. Rapp and Y. Yang, “The Modeling of Liquor Flow in Textile beam dyeing,” *The Journal of The Textile Institute*, vol. 95, no. 1-6, pp. 243-250, 2004.
- [33] S. Scharf, E. Cleve, E. Bach, E. Schollmeyer, “Three-Dimensional Flow Calculation in a Textile Dyeing Process,” *Textile Research Journal*, pp. 783-788, 2002.
- [34] E. Mancusi, S. Ulson de Souza and A. Ulson de Souza, “Numerical Analysis of a Periodically Forced Dyeing Process,” *Industrial & Engineering Chemistry Research*, vol. 49, p. 8568–8574, 2010.
- [35] R. Reji, T. Kim, S. Son, A. Suryan and H. Kim, “Computational investigation on the flow characteristics in beam dyeing process,” *The Journal of The Textile Institute*, 2019.
- [36] M. Moreno, J. Borges Valle, C. Lange de Aguiar and A. Da Silva, “Influence of permeability and pressure on the dye concentration profile in acrylic yarn bobbins in bidirectional flow by simulation,” *Brazilian Journal of Chemical Engineering*, vol. 37, p. 515–524, 2020.
- [37] B. Shannon, W. Hendrix, B. Smith and G. Montero, “Modeling of supercritical fluid flow through a yarn package,” *Journal of Supercritical Fluids*, vol. 19, pp. 87-99, 2000.
- [38] H. Zheng, Y. Su, L. Zheng and H. Ke, “Numerical simulation of CO₂ and dye separation for supercritical fluid in separator,” *Separation and Purification Technology*, vol. 236, 2020.
- [39] N. Tou, “An Investigation of Arcing in Two Structure Weft Knit Fabrics,” *North Carolina State University*, 2005.

- [40] R. Ogulata and S. Mavruz, "Investigation of Porosity and Air permeability values of plain knitted fabrics," *FIBRES & TEXTILES in Eastern Europe*, vol. 18, no. 82, pp. 71-75, 2010.
- [41] S. Stankovic, D. Popovic and G. Poparic, "Thermal properties of textile fabrics made of natural and regenerated cellulose fibers," *Polymer Testing*, vol. 27, no. 1, pp. 41-48, 2008.
- [42] X. Xiao, Modeling the Structure-permeability Relationship, PhD thesis, University of Nottingham, 2012.
- [43] G. Bedek, F. Salaün, Z. Martinkovska, E. Devaux and D. Dupont, "Evaluation of thermal and moisture management properties on knitted fabrics and comparison with a physiological model in warm conditions," *Applied Ergonomics*, vol. 42, no. 6, pp. 792-800, 2011.
- [44] T. Lundstrom, S. Toll and M. Hakanson, "Measurement of the Permeability Tensor of Compressed Fibre Beds," *Transport in Porous Media*, vol. 47, p. 363–380, 2002.
- [45] S. Sharma and D. Siginer, "Permeability Measurement Methods in Porous Media of Fiber Reinforced Composites," *Applied Mechanics Review*, vol. 63, no. 2, 2010.
- [46] B. Gebart, "Permeability of unidirectional reinforcements for RTM," *Journal of Composite Materials*, vol. 26, no. 8, pp. 1100-1133, 1992.
- [47] W. Young, "Consolidation and Cure Simulations for Laminated Composites," *Polymer composites*, vol. 17, no. 1, pp. 142-148, 1996.
- [48] A. Berdichevsky and Z. Cai, "Preform permeability predictions by self-consistent method and finite-element simulation," *Polymer Composites*, vol. 14, no. 2, pp. 132-143, 1993.
- [49] F. Phelan and G. Wise, "Analysis of transverse flow in aligned fibrous porous," *Composites Part A-Applied Science and Manufacturing*, vol. 27, no. 1, pp. 25-34, 1996.
- [50] A. Kulichenko, "Theoretical analysis, calculation, and prediction of the air," *Fibre Chemistry*, vol. 37, no. 5, pp. 371-380, 2005.
- [51] Z. Zupin, A. Hladnik and K. Dimitrovski, "Prediction of one-layer woven fabrics air permeability using porosity parameters," *Textile Research Journal*, vol. 82, no. 2, pp. 117-128, 2012..
- [52] M. Bruschke and S. Advani, "Flow of generalized Newtonian fluids across a periodic array of cylinders," *Journal of Rheology*, vol. 37, no. 3, pp. 479-498, 1993.

- [53] M. Brusckhe and S. Advani, "A finite element/control volume approach to mold filling in anisotropic porous media," *Polymer Composites*, vol. 11, no. 6, pp. 398-405, 1990.
- [54] X. Xiao, X. Zeng, A. Long, H. Lin, M. Clifford and E. Sldaeva, "An analytical model for through-thickness permeability of woven fabric," *Textile Research Journal*, vol. 82, no. 5, pp. 492-501, 2012.
- [55] X. Xiao, J. Hu, T. Hua, X. Zeng and A. Long, "Through-thickness air permeability of woven fabric under low pressure compression," *Textile Research Journal*, vol. 85, no. 16, pp. 1732-1742, 2015.
- [56] A. Endruweit and A. Long, "Analysis of compressibility and permeability of selected 3D woven reinforcements," *Journal of Composite Materials*, vol. 44, no. 24, pp. 2833-2862, 2010.
- [57] J. Mogavero and S. Advani, "Experimental investigation of flow through multilayered preforms," *Polymer Composites*, vol. 18, no. 5, pp. 649-655., 1997.
- [58] Z. Chen, L. Y. Ye and H. Liu, "Effective permeabilities of multilayer fabric preforms in liquid composite moulding," *Composite Structures*, vol. 66, no. 1, pp. 351-357, 2004.
- [59] Y. Song, D. Heider and J. Youn, "Statistical characteristics of out-of-plane permeability for plain-woven structure," *Polymer Composites*, vol. 30, no. 10, pp. 1465-1472, 2009.
- [60] S. Dehkordi, M. Ghane, S. Abdellahi and M. Soultanzadeh, "Numerical Modeling of the Air Permeability of Knitted Fabric Using Computational Fluid Dynamics (CFD) Method," *Fibers and Polymers*, vol. 18, no. 9, pp. 1804-1809, 2017.
- [61] H. Lin, L. Brown and A. Long, "Modelling and Simulating Textile Structures using TexGen," *Advanced Materials Research*, vol. 331, pp. 44-47, 2011.
- [62] R. Ogulata, "Air permeability of Woven Fabrics," *Journal of Textile and Apparel, Technology and Management*, vol. 5, no. 2, 2006.
- [63] K. Nataajan, "Air Permeability of elastomeric fabrics as a function of uniaxial tensile strain," *M Sc., North Carlina.*, 2003.
- [64] Z. Zupin, A. Hladnik and K. Dimitrovski, "Prediction of one-layer woven fabrics air permeability using porosity parameters," *Textile Research Journal*, vol. 82, no. 2, pp. 117-128, 2012.
- [65] A. Pezzin, Thermo-physiological comfort modelling of fabrics and garments, PhD in Chemical Engineering, Politecnico di Torino, 2014.
- [66] E. Karaca, N. Kahraman, S. Omeroglu and B. Becerir, "Effects of Fiber Cross Sectional Shape and weave Pattern on thermal comfort properties of polyester woven fabrics,"

Fibres & Textile in Eastern Europe, vol. 92, no. 3, pp. 67-72, 2012.

- [67] Z. Ettehadi, S. Ajeli, P. Soltani and M. Zarrebini, “Experimental and CFD Analysis of Air Permeability of warp-knitted structures,” *Fibers and Polymers*, vol. 21, no. 16, pp. 1362-1371, 2020.
- [68] J. Sierra-Pallares, M. Parra-Santos, J. García-Serna, F. Castro and M. Cocero, “Numerical analysis of high-pressure fluid jets: Application to RTD prediction in supercritical reactors,” *The Journal of Supercritical Fluids*, vol. 49, p. 249–255, 2009.

Appendix I: Air permeability data

Table 0-1: Air permeability data from Ettehadi et al. [67] (knitted)

Sample code	Thickness (mm)	Air permeability (cm ³ /cm ² s)	Areal density (g/m ²)
Sb-1 - Single bar 1×1	0.140	698.090	58.400
Sb-2 - Single bar 2×1	0.160	473.880	68.700
L-1 - Locknit	0.340	243.310	138.700

Table 0-2: Air permeability data from Dehkordi et al. [60] (knitted)

Sample	Thickness (mm)	Air permeability (cm ³ /cm ² s)	Areal density (g/m ²)
R1 (a) - rib 1x1	0.560	364.000	130.820
R2 (b) - rib 1x1	0.580	321.000	134.610
R3 (c)-rib 1x1	0.630	290.000	151.230
I1 (d) - interlock	0.700	275.000	278.040
I2 (e) - interlock	0.790	156.000	246.700
I3 (f) - interlock	0.810	140.000	264.140

Table 0-3: Air permeability data from Zupin et al. [51] (woven)

Sample	Thickness (mm)	Air permeability (cm ³ /cm ² s)	Areal density (g/m ²)
PL22/15	0.439	239.167	143.910
PL22/20	0.438	157.167	166.590
PL29.3/15	0.468	126.833	180.410
PL29.3/20	0.514	46.967	209.500
BW22/15	0.506	306.500	140.520
BW22/20	0.531	218.667	160.900
BW29.3/15	0.604	201.917	173.120

BW29.3/20	0.567	120.917	195.980
R4/222/15	0.591	349.167	138.140
R4/222/20	0.558	235.250	160.600
R4/229.3/15	0.620	224.167	171.530
R4/229.3/20	0.605	132.500	196.300
R2/422/15	0.549	328.833	143.770
R2/422/20	0.557	224.750	163.890
R2/429.3/15	0.471	139.500	179.930
R2/429.3/20	0.480	89.833	202.520
T1/322/15	0.565	350.583	141.360
T1/322/20	0.558	216.167	162.240
T1/329.3/15	0.596	157.917	176.610
T1/329.3/20	0.586	83.300	198.110
BT1/322/15	0.559	350.167	140.480
BT1/322/20	0.546	226.500	162.130
BT1/3 29.3/15	0.571	173.333	176.760
BT1/3 29.3/20	0.557	92.992	197.520
T2/2 22/15	0.508	301.625	141.780
T2/2 22/20	0.504	202.333	160.660
T2/2 29.3/15	0.604	168.167	173.340
T2/2 29.3/20	0.568	88.550	197.480
BT2/2 22/15	0.522	316.917	139.010
BT2/2 22/20	0.511	178.833	161.610
BT2/2 29.3/15	0.632	206.917	171.980
BT2/2 29.3/20	0.589	103.583	195.360
CT 22/15	0.625	346.583	142.530
CT 22/20	0.605	213.000	164.050
CT 29.3/15	0.646	189.000	176.650

CT 29.3/20	0.630	97.817	202.350
-------------------	-------	--------	---------

Table 0-4: Air permeability data from Karaca et al. [66] (woven)

Sample	Thickness (mm)	Air permeability (cm³/cm²s)	Areal density (g/m²)
R-P - ROUND - plain	0.270	1.867	161.000
HR-P - HOLLOW ROUND - plain	0.310	0.100	168.000
T-P TRILOBAL - plain	0.250	1.900	160.000
HT-P HOLLOW TRILOBAL - plain	0.280	1.050	166.000
R-T TOUND - twill	0.292	20.567	156.000
HR-T HOLLOW ROUND - twill	0.330	16.450	162.000
T-T TRILOBAL - twill	0.273	26.400	154.000
HT-T HOLLOW TRILOBAL - twill	0.310	17.917	159.000

Appendix II

Here is reported the script written by Pezzin [65], which has been adapted to the present work in order to create the plain weave with 22 ends/cm for warp yarns and 15 ends/cm for weft yarns in TexGen.

```
# Create a textile
Textile = CTextile()

#create weft yarn
# Create a lenticular section
Section = CSectionLenticular(0.398, 0.219)

# Create yarns
Yarns = (CYarn(), CYarn())

# Add nodes to the yarns to describe their paths
Yarns[0].AddNode(CNode(XYZ(0, 0, 0)))
Yarns[0].AddNode(CNode(XYZ(0, 0.5, 0.218)))
Yarns[0].AddNode(CNode(XYZ(0, 1, 0)))

Yarns[1].AddNode(CNode(XYZ(0.714, 0, 0.218)))
Yarns[1].AddNode(CNode(XYZ(0.714, 0.5, 0)))
Yarns[1].AddNode(CNode(XYZ(0.714, 1, 0.218)))
# create the same interpolation and section shape for all the yarns
for Yarn in Yarns:
    # Set the interpolation function
    Yarn.AssignInterpolation(CInterpolationCubic())
    # Assign a constant cross-section along the yarn
    Yarn.AssignSection(CYarnSectionConstant(Section))
    # Set the resolution
    Yarn.SetResolution(30)
    # Add repeats to the yarn
    Yarn.AddRepeat(XYZ(1.428, 0, 0))
    Yarn.AddRepeat(XYZ(0, 1, 0))
    # Add the yarn to the textile
    Textile.AddYarn(Yarn)

#create warp yarn
Section=CSectionLenticular(0.398, 0.219)
#create yarns
Yarns=(CYarn(), CYarn())
#Add nodes to the yarns to describe their paths
Yarns[0] .AddNode(CNode(XYZ(0, 0, 0.218)))
Yarns[0] .AddNode(CNode(XYZ(0.714, 0, 0)))
Yarns[0] .AddNode(CNode(XYZ(1.428, 0, 0.218)))
Yarns[1] .AddNode(CNode(XYZ(0, 0.5, 0)))
Yarns[1] .AddNode(CNode(XYZ(0.714, 0.5, 0.218)))
Yarns[1] .AddNode(CNode(XYZ(1.428, 0.5, 0)))
#create the same interpolation and section shape for all the yarns
for Yarn in Yarns:
    # Set the interpolation function
    Yarn.AssignInterpolation(CInterpolationCubic())
    # Assign a constant cross-section along the yarn
    Yarn.AssignSection(CYarnSectionConstant(Section))
    # Set the resolution
    Yarn.SetResolution(30)
    # Add repeats to the yarn
    Yarn.AddRepeat(XYZ(1.428, 0, 0))
    Yarn.AddRepeat(XYZ(0, 1, 0))
    # Add the yarn to the textile
    Textile.AddYarn(Yarn)

#Assign domain to the textile
Textile.AssignDomain(CDomainPlanes(XYZ(0, -0.25, -0.15), XYZ(1.428, 1.5, 0.35))) ;
# Add the textile with the name "cotton_plain_woven"
AddTextile("cotton_plain_woven", Textile)
```

Ringraziamenti

Ai miei relatori, che mi hanno guidata durante questi mesi, grazie per la comprensione, disponibilità e fiducia nei miei confronti.

Alla mia famiglia, grazie per avermi supportata in ogni mia scelta, per i vostri preziosi consigli e per aver sempre creduto in me.

Ai miei nonni, per avermi insegnato a non accontentarmi e a migliorarmi ogni giorno di più.

A mia madre, per essere stata sempre presente e per avermi trasmesso l'impegno e la passione per lo studio.

A Gianmarco, grazie per aver creduto in me più di quanto faccia io stessa, per essere stato un punto di riferimento, soprattutto in questi ultimi mesi, e per aver sempre sostenuto i miei piani, anche quando sembravano un po' troppo audaci.

A tutte le persone che ho incontrato durante questi anni, amici e conoscenti, grazie per aver condiviso con me gioie e dolori, messaggi di incoraggiamento reciproco e di sostegno.

Al gruppo I.U.P.A.C. (*I Uagliun Potent A Chimic*, letteralmente), vi devo questo ringraziamento da un paio d'anni, ma sapete come si dice... Grazie per avermi accolta nella vostra famiglia, per tutte le giornate e le serate passate insieme, non so immaginare questi anni senza di voi.

A Luca, il mio fedele revisore di bozze, grazie per aver condiviso con me ansie e preoccupazioni, soddisfazioni e vittorie in questi lunghi mesi.

A Marco, collega e dirimpettaio, ai ragazzi del *Team Famiglia* e a tutte le persone che ho avuto modo di conoscere a Torino, tutte voi avete contribuito a rendere questi anni indimenticabili, grazie.